High-dimensional Quantum Key Distribution with Frequency Encoding

by

Changchen Chen

B.S., University of Rochester (2015)
S.M., Massachusetts Institute of Technology (2017)

Submitted to the Department of Electrical Engineering and Computer Science
in partial fulfillment of the requirements for the degree of

Doctor of Philosophy in Electrical Engineering and Computer Science

at the

MASSACHUSETTS INSTITUTE OF TECHNOLOGY

September 2021

Author .....
Department of Electrical Engineering and Computer Science
August 20, 2021

Certified by .....
Franco N. C. Wong
Senior Research Scientist, Research Laboratory of Electronics
Thesis Supervisor

Accepted by .....
Leslie A. Kolodziejski
Professor of Electrical Engineering and Computer Science
Chair, Department Committee on Graduate Students

High-dimensional Quantum Key Distribution with Frequency Encoding

by

Changchen Chen

Submitted to the Department of Electrical Engineering and Computer Science
on August 20, 2021, in partial fulfillment of the
requirements for the degree of
Doctor of Philosophy in Electrical Engineering and Computer Science

Abstract

Time-energy entanglement is a quintessential resource for emerging quantum technologies. In this thesis, we harness this resource for applications such as quantum communication and quantum networking. In the first part of this thesis, we demonstrate an indistinguishable heralded single-photon source, featuring time-energy entanglement elimination in the spontaneous parametric down-conversion (SPDC) process through custom engineering of phase-matching conditions. The heralded single-photon source is useful in measurement-based quantum applications, where indistinguishable single photons are required to ensure high-visibility photon-photon interference.

The second part of this thesis studies the time-domain characterization of time-energy entangled photon pairs. We present here the first experimental demonstration of the conjugate-Franson interferometer (CFI). We show that the CFI visibility can certify time-energy entanglement and detect the biphoton spectral phase, which Franson interferometry and Hong-Ou-Mandel interferometry are incapable of.

In the final part of this thesis, we show an experimental demonstration of high-dimensional quantum key distribtuion (QKD) protocol with frequency-bin encoding using time-energy entangled photon pairs. We used programmable frequency filters to obtain 16 frequency bins for key generation within a 640 GHz flat spectrum in the telecommunication wavelength band. The security of the protocol was safeguarded by the CFI visibility being measured at the same time of the key generation process. Over a 137-meter fiber link, we measured a secure photon information efficiency (PIE) of 0.6 bit/coincidence, corresponding to a secret key rate (SKR) of 42.6 kbits/s.

Thesis Supervisor: Franco N. C. Wong
Title: Senior Research Scientist, Research Laboratory of Electronics

Acknowledgments

It would not be possible to complete this thesis and my graduate school study without the help and support from my professors, colleagues, friends, and family.

I am extremely grateful to my research advisor, Dr. Franco Wong, for his guidance and support in the past six years. He introduced me to the field of experimental quantum optics and made this thesis possible. Besides his profound insights on experimental techniques, his attention to detail sets him as a rigorous researcher for me to follow. I have benefited enormously from his philosophy about science, education, and beyond.

I want to thank Prof. Jeffrey H. Shapiro for his guidance on my theoretical study. His superb ability to get to the bottom of a problem quickly, perform calculations on the fly, and show profound theoretical insight made him an excellent research role model. I would also like to thank Prof. Dirk Englund for kindly agreeing to be on my thesis committee. It was an honor to work with Prof. Dirk Englund on many collaborative projects. I also feel privileged to work with Prof. Marko Lončar.

I want to say a special thank you to Zheshen Zhang and Feihu Xu, who helped with my transition during the first couple of years of graduate school. I would also like to thank my lab mates Jane Heyes, Murphy Yuezhen Niu, Justin Dove, Quntao Zhuang, and Connor Henley for making graduate school bearable.

It is a pleasure to collaborate with many great researchers on numerous projects. I have learned tremendous knowledge and skills from working with them. I would like to express my gratitude to Dr. Kyung-Han Hong, Bo Cao, Di Zhu, Marco Colangelo, Ching-Wei Lin, Jacques Carolan, Nicholas Harris, Mihika Prabhu, Darius Bunandar, Saumil Bandyopadhyay from MIT; Catherine Lee, Ryan Murphy, Ben Dixon from Lincoln Laboratory; Adriana Lita, Thomas Gerrits, Sae Woo Nam from NIST; and Xiang Cheng, Murat Can Sarihan, Kai-Chi Chang, and Prof. Chee Wei Wong from UCLA.

Finally, I want to thank my parents for their support and love.

This work was supported in part by AFOSR and NSF.

Contents

List of Figures

List of Tables

Chapter 1

Introduction

Advancements in quantum technology provide new opportunities in the fields of computing [1, 2, 3], communication [4], and sensing [5]. In classical secure communication, two distant parties, Alice and Bob, share a set of encryption and decryption keys and establish information exchange in a public channel. The secure communication between Alice and Bob relies on the encryption or decryption keys that are not known to the adversarial eavesdropper Eve. For instance, the secure message exchange between Alice and Bob is usually handled using RSA public-key cryptography. RSA public-key cryptography is based on a computational complexity assumption that deciphering the encrypted message is exponentially hard if one does not have the private key. Breaking RSA public-key encryption security requires factoring the product of two large prime numbers, which does not have an efficient classical algorithm yet. Nevertheless, this type of encryption scheme is theoretically breakable and not unconditionally secure. In 1994, an efficient quantum algorithm for factoring a large number was discovered by Peter Shor [6] that renders the RSA encryption insecure. Therefore, an unconditionally secure communication protocol is needed for encrypting sensitive information to counter the soon-to-be-realized Shor's algorithm and any future advancements in decryption technology.

Quantum key distribution (QKD) provides unconditionally secure communication between two parties vouchsafed by the law of physics. In QKD, randomized keys encoded on quantum states are exchanged between Alice and Bob. Because an unknown

quantum state cannot be perfectly copied, any alteration attempts by Eve therefore introduce measurable communication error in the system [7, 8]. If Eve tries to eavesdrop on the communication channel, Alice and Bob can detect the disturbance caused by Eve, abort the communication, and discard the exchanged key. Because there is no actual information being exchanged during key distribution sessions, exchanged key gained by Eve does not reveal any real information. Alice and Bob can postpone their communication until they establish a set of secure keys that are not known to Eve. Messages can then be encoded using one-time-pad encryption with the established secure keys and sent over a classical public channel. We should note here that the encryption keys should have the same length as that of the message and are not re-used to ensure absolute secrecy [9]. There are different QKD protocols that have been proposed and demonstrated, some of which are briefly discussed below.

1.1 Prepare-and-measure protocol

In the prepare-and-measure protocol, Alice prepares the encoded pulses or photons and sends them to Bob, who receives and decodes the message. One of the best known prepare-and-measure QKD protocols is the Bennet-Brassard 1984 (BB84) protocol [10, 11]. In BB84, each bit value of the key is randomly encoded on the polarization state of a single photon, and the sequence of single photons is transmitted via a quantum channel. The common polarization states used for encoding are the rectilinear basis of vertical (V) and horizontal (H) and the diagonal basis of 45° and 135°. Nevertheless, any two mutually unbiased bases can be used for encoding. Alice randomly chooses one of the mutually-unbiased bases and prepares the photon in one of the two orthogonally-polarized states, denoting it bit 0 or 1, and sends it to Bob. After Bob has received the photon, he randomly selects a basis to measure the photon's polarization, and records the bit-value result. After a series of detections has been made, Bob announces his basis choice for each of his received photons on an authenticated public channel, and Alice indicates the cases in which they used the same basis. Alice and Bob only keep the results in which the same basis was used for

the measurement. The data they keep become the sifted key. A portion of the sifted key is used to determine the quantum bit error rate (QBER). A high QBER indicates Eve's presence and shows that the communication link is not secure. If the QBER is satisfactory, Alice and Bob can perform error correction and privacy amplification to obtain the secret keys.

A simple strategy for Eve to attack the quantum channel is the intercept-and-resend attack [10]. In this attack, Eve randomly chooses a basis and performs the polarization measurement. She then sends Bob a new photon encoded according to her chosen basis and measurement result. The probability of Eve selecting the correct basis is 50%. If the correct basis is chosen, Eve introduces no additional error. Otherwise, the photon Bob received has a random polarization compared to Alice's encoded polarization. In this case, Eve presents a minimum of 25% QBER when she performs intercept-and-resend attack. This simple example shows that Eve cannot eavesdrop on Alice and Bob's key distribution without introducing noticeable errors in the quantum communication channel.

The BB84 protocol calls for using single photons in the key exchange, but, in practice, it is usually implemented with an attenuated laser source. The attenuated laser source is not a true single-photon source. The emission of two or more photons gives Eve the opportunity to split off one of the photons and perform a measurement without degrading the QBER. This hacking strategy is known as the photon-number-splitting (PNS) attack [12, 13]. The decoy-state method was proposed to fend off the PNS attack [14, 15]. The decoy-state method uses weak coherent pulses of several different intensity levels instead of one intensity level for encoding. Alice and Bob can then actively monitor the quantum channel by distinguishing between the signal and decoy states. Eve's channel interference inevitably changes the detection rates for signal and decoy states differently, thus revealing her presence. The decoy-state QKD dramatically improves the performance and has become a common practice in implementing today's QKD systems.

The BB84 protocol is a discrete-variable (DV) protocol because it encodes information in a discrete variable space. Other DV protocols, such as coherent one-way [16]

and differential-phase-shift [17], encode information on photon arrival time and relative phase between adjacent weak coherent pulses. Keys can also be encoded in a continuous variable (CV) space, such as the quadratures of the coherent state [18].

1.2 Entanglement-based protocol

An alternative to the prepare-and-measure protocol is the entanglement-based protocol that utilizes entangled photon pairs as the photon source. Alice and Bob can obtain correlated measurement results from the shared entangled photon pairs. Furthermore, Alice does not need to prepare the photon in a specific quantum state before sending it over the quantum channel, which is different from what is done in the prepare-and-measure protocol. The secret key is extracted from the correlated measurement results of the entangled photon pairs' states, whether the measurements are carried out before or after the entangled pairs are distributed. An example of the entanglement-based protocol is the Ekert91 protocol [19]. In Ekert91, polarization-entangled photon pairs are generated and distributed to Alice and Bob. The entangled photon pairs can be provided by Alice, Bob, a trusted or untrusted third party, or even Eve. Alice and Bob then measure the photons' polarization. After a series of measurements, Alice and Bob use their results to extract secret keys and check for communication security.

The security of the Ekert91 protocol relies on the quality of the entanglement. Alice and Bob use part of their measurement results to compute the S value in the Clauser-Horne-Shimony-Holt (CHSH) inequality [20]. The CHSH inequality is a generalization of Bell's theorem [21]. When the photon pairs are maximally entangled, the CHSH S value has a maximum value of $2\sqrt{2}$. If Eve eavesdrops on the communication link, she will unavoidably degrade the entanglement quality that results in a lower S value. As a result, Eve's presence can be determined by actively monitoring the CHSH inequality S value. Many experiments have demonstrated a substantial violation of the CHSH inequality with results close to the maximum S value [22, 23, 24, 25, 26]. Therefore, Alice and Bob can detect any slight decrease in CHSH value, providing

a sensitive and accurate method to safeguard the communication link. An essential advantage of an entanglement-based protocol is that the randomness of the photon's bit value (such as polarization) can be characterized by the entanglement source's CHSH S parameter value.

Nevertheless, the entanglement-based QKD system's key rate is typically on the order of kbits/s, which is not enough to satisfy today's data demand. For example, a live video feed requires Mbits/s of bandwidth to function. The low key rate limits the possible applications and usefulness of entanglement-based QKD. The bottleneck of the limited key rate is mainly due to the quantum light source's low flux. When operating in a higher flux regime, multiple entangled pairs or fluorescence can be emitted simultaneously, significantly decreasing the entanglement's quality and the achievable communication security key rate. Consequently, the entanglement-based QKD system has to operate in the low-flux regime such that the probability of more than one photon pair emitted within a bit duration is small.

1.3 High-dimensional quantum key distribution

One option to achieve a higher secure key rate is to expand the dimensions of the encoding space. Instead of polarization encoding used in BB84 and Ekert91, one can use orbital angular momentum (OAM) of light to encode information. Theoretically, OAM and its mutually unbiased basis, azimuthal angle (ANG) basis, have infinite dimensions. Nevertheless, the achievable dimension is limited by the aperture of the optical system. Free space OAM encoding QKD experiments have been demonstrated using an attenuated laser source or an entangled photon source [27, 28], showing a seven-dimensional alphabet encoding. Nevertheless, the generation rate of arbitrary OAM modes is limited, which constrains the achievable key rate in the OAM-QKD system. OAM is typically generated using spatial light modulators that have a 60 Hz refresh rate. High OAM generation rate at 4 kHz has been demonstrated using a digital micro-mirror device (DMD) [29]. Another drawback of OAM mode is that it is susceptible to turbulence and cannot be transmitted in standard single-mode optical

fiber. Therefore, using OAM for high rate QKD has some practical challenges that need to be overcome.

Time-energy entanglement is continuous-variable (CV) in nature and can provide sufficient dimensions for time or frequency encoding [30]. Furthermore, time-energy entangled photons can be reliably transferred through standard single-mode fiber, utilizing existing telecommunication networks. Dispersive-optics (DO) QKD has been proposed and experimentally demonstrated as a scheme to boost the secret key rate [31, 32]. In DO-QKD, the entangled photon pairs are distributed between Alice and Bob, and they detect the photons in the time basis or frequency basis. In the time basis it is to detect the photons' arrival times, and in the frequency basis the photons' frequency contents are measured. The frequency measurement is achieved by introducing normal dispersion and anomalous dispersion to the photons, converting their frequency information to arrival times. Signal and idler photons remain correlated if Alice and Bob choose the same basis for measurement. A dimension of 64 was achieved in the DO-QKD setup, resulting in Alice and Bob's Shannon information of 2.82 bits per coincidence detection [31]. The security of DO-QKD is based on nonlocal dispersion cancellation between the entangled photons. Eve's Holevo information can be bounded using the time-frequency covariance matrix (TFCM). Elements of the TFCM can be estimated from time basis and frequency basis measurements, limited by detector jitter and the amount of applied dispersion [32].

A different approach to utilizing time-energy entanglement is to encode in the photons' arrival times and perform the security check through Franson interferometry [33, 34]. Using low jitter single-photon detectors and high precision time taggers, Zhong *et al.* were able to achieve a dimension of 1024, yielding a secret key capacity of 6.9 bits per photon coincidence after 20 km fiber transmission. Eve's Holevo information is bounded using the TFCM, similar to what is done in the DO-QKD protocol. The TFCM is estimated using a Franson interferometer, assuming that the detector jitter limits the system's timing variation. The Franson interferometer is a direct test of time-energy entanglement, equivalent to the CHSH inequality measurement in polarization-entangled photons. Furthermore, the Franson interferometer probes

the frequency correlation, providing information on the conjugate of the encoding basis [35]. However, a 30% constant bit error rate is observed in time-bin encoding due to detector timing jitter [33]. Although the high QBER is largely corrected using a layered LDPC code, it constrains the key rate's further optimization.

1.4 Status of quantum key distribution deployment

Although QKD systems have been demonstrated successfully in laboratory settings, solutions for a practical commercial system are still under active research and development. A major shortcoming barring the QKD system from practical usage today is the limited secret key rates. QKD systems transfer secret keys used for one-time-pad encryption, which requires the key to be as long as the message. This requirement puts significant constraints on the QKD communication rate. Presently, the classical optical communication rates are on the order of Tbit/s. On the other hand, today's high-rate QKD systems can only deliver Mbit/s speeds, which is insufficient for large-scale network deployment [36].

It is also difficult to extend the communication range of QKD systems. Typically, QKD systems operate in photon starved condition, which is sensitive to channel loss. For example, in BB84 no bit information is transmitted if the photon carrier is lost en route. Improvement on fiber channel loss is difficult as it is limited by the light scattering inside the fiber core. As a result, besides developing better sources and detectors to tolerate higher transmission loss, the development of a quantum repeater is essential to scale up the communication distance of QKD systems.

Another important issue is the cost and robustness of QKD systems. For example, most QKD protocols require detectors to have high efficiency and low noise at the single-photon level. Such detectors are expensive to deploy in large quantities because of the tight technical requirements. Photonic integration of the QKD system can deliver compact QKD transceivers at low cost and hence can be a solution to this problem. The major platforms for integration are silicon (Si), indium phosphide (InP), lithium niobate ($LiNbO_3$), and glass waveguide [36]. Although the research on

integrated quantum photonics is still in its early stage, it holds a promising future for practical QKD systems.

Despite many technical challenges in realizing large-scale commercial QKD systems, experimental QKD networks have been established worldwide. For example, the DARPA quantum network, set up in 2004 in Massachusetts, USA, had 10 nodes linking MIT and Harvard [37]. Similar networks have been set up in Europe, Japan, and China [38, 39, 40]. Recently, a satellite-based QKD network has also been established that provides kHz communication rates over a distance of up to 1,200 km [41]. Twin-field QKD has also been demonstrated over 511 km of optical fiber [42].

1.5 Thesis overview

In this dissertation, we tackle some of the aforementioned problems by engineering the time-frequency correlation of entangled photon pairs. First, we investigate and develop a new source of single photons in a single spatiotemporal mode for long-distance entanglement distribution using the DLCZ protocol [43]. In the DLCZ protocol, two photons that interact at a beam splitter need to be completely indistinguishable to achieve a high success rate. This can only be done if the two interacting photons have the same spatiotemporal mode. Here, we propose and demonstrate a heralded single-photon source that can produce indistinguishable single photons that are in a single spatiotemporal mode for entanglement generation and distribution and other quantum network tasks.

Next, we study the fundamental property of time-energy entanglement through newly developed nonlocal conjugate-Franson interferometry. Understanding and characterizing time-energy entanglement is a fundamental building block for entanglement-based, high-dimensional quantum information processing using biphotons. The conventional method for characterizing such time-energy entanglement is nonlocal Franson interferometry. Franson interference can certify that a biphoton state is entangled, but it cannot fully characterize that state. This drawback is due to Franson interferometry's fringe visibility being determined by the biphoton's joint spectral intensity

(JSI), which falls short of full state characterization as it lacks the spectral phase information needed to determine the state's joint spectral amplitude (JSA). Measurement of the biphoton's joint temporal intensity (JTI) would complete state characterization made with Franson interferometry, because spectral phase can be retrieved from knowledge of the JSI and JTI. Previous experiments that measure a biphoton's JTI, however, have been limited to time-resolved local interference with nearly-degenerate photon pairs or have required femtosecond pulse gating and phase-sensitive detection with a stable and well-characterized classical field. In contrast, the conjugate-Franson interferometer (CFI), first proposed in Phys. Rev. Lett. **112**, 120506 (2014) [35], provides a much more powerful and convenient route to JTI determination for monochromatic pumped spontaneous parametric down-conversion (SPDC). In particular, the conjugate-Franson interferometer is a nonlocal measurement that can work with non-degenerate photon pairs generated by pulse-pumped or continuous-wave sources, and it does not require ultrafast pulse gating. Overall, the conjugate-Franson interferometer provides a new and convenient method for quantifying the temporal-correlation behavior of time-energy entangled photons. In conjunction with a JSI measurement obtained using a Franson interferometer, our conjugate-Franson interferometer's JTI measurement completely characterizes a biphoton's state. As a result, this work has the potential to significantly expand the current quantum-measurement toolbox.

Finally, we explore a frequency domain protocol for a high-dimensional QKD (HDQKD) system. We expect to obtain an improved QBER rate better than the 30% seen in time-bin encoding by adopting frequency-bin encoding. Furthermore, frequency-bin encoding also has a greater potential of achieving a larger encoding dimension as it can utilize the photon pairs' few THz bandwidth ranges. In the previously discussed time-bin encoding protocol, increasing the encoding alphabet extends the required time frame for single entangled pair emission, limiting photon flux. This flux-dimension trade-off does not apply to the frequency-bin encoding scheme because increasing the frequency bin number does not affect the measurement time frame, providing a more promising outlook for high rate operation.

The thesis is organized as follows:

- Chapter 2 summarizes the theory of generating factorable biphotons and describes the relevant experiment and its key results. Using a $KTiOPO_4$ (PPKTP) crystal with a tailored Gaussian phase-matching function, we demonstrate high Hong-Ou-Mandel interference (HOMI) visibility between independent heralded photons. We also investigate the effects of pump spectral shape on the HOMI visibility.

- Chapter 3 presents a frequency shifter that utilizes a commercially available quadrature phase-shift keying modulator. We demonstrate the performance of this modulator by shifting the frequency of classical monochromatic laser light and broadband single photons. We further show that the frequency shifter only acts on the frequency mode and does not affect other input properties.

- Chapter 4 introduces and discusses conjugate-Franson interferometry. In this chapter, we review the theory of the CFI and show the link between CFI visibility and the input's JTI. We present the first experimental demonstration of the CFI and show that the visibility decreases by up to 21% when a spectral phase is introduced in the input biphoton state.

- Chapter 5 presents the frequency domain high-dimensional quantum key distribution (QKD) protocol. In this chapter, we discuss the frequency encoding scheme and the calculation of communication key rate. We also show how to secure the protocol against Eve's collective attack using conjugate-Franson interferometry. Finally, we present the first proof-of-concept demonstration of high-dimensional QKD with frequency encoding.

- Chapter 6 summaries the major results and gives future research outlooks.

Chapter 2

Indistinguishable single-mode photons from spectrally engineered biphotons

Measurement-based quantum applications require strong photon-photon interference to improve their success rates. Specifically, deterministic and highly indistinguishable single-photon sources are the key for scalable implementation in photonics-based quantum simulation or long-distance quantum entanglement distribution. Because of the presence of photon loss, it is not easy to have a genuinely deterministic source. An alternative approach is to use photon pairs generated from pulsed spontaneous parametric down-conversion (SPDC). A successful heralding detection of the idler photon indicates the presence of the signal photon. The SPDC process is robust, operational at room temperature, and scalable using the lithium niobate thin-film platform [44]. Although this process is probabilistic in nature, multiple photon sources can be multiplexed to effectively guarantee that a photon is generated within one clock cycle [45].

The heralded single photons are in a spectrally mixed state because of the entanglement between signal and idler photons. This spectrally mixed state decreases interference between different photons and is not desirable for the aforementioned measurement-based quantum applications. The frequency entanglement between SPDC signal and idler has to be eliminated to solve this issue. Methods to eliminate frequency entanglement are beyond the scope of this thesis and are not discussed in this chapter. For more information on this topic, please see our previous publication,

Opt. Express **25**, 7300-7312 (2017) [46] and discussion in my Master's thesis [47]. In this chapter, we focus on the experimental verification of the heralded photons' indistinguishability. We first review the indistinguishable heralded single-photon source in periodically poled $KTiOPO_4$ (PPKTP) with phase-matching function engineering. Next, we discuss the theory of factorable photon pairs and present experimental verification of the indistinguishability between the independently generated heralded photons.

Materials presented in this chapter have been published in Opt. Express **27**, 11626-11634 (2019) [48].

2.1 Introduction

In a prototypical quantum network with multiple quantum nodes, single photons in a well-defined single-spatiotemporal mode are highly desirable for implementing qubit measurement-based quantum information processing and networking applications. High-purity single-mode photons are especially important for complex tasks that may involve multiple quantum interference measurements, such as quantum computation and simulation [49, 50], or realization of a scalable quantum network [43, 51]. It is quite simple to herald single photons from biphotons generated in pulsed SPDC. In general, however, SPDC biphotons are frequency entangled, as can be seen from their predicted joint spectral amplitude (JSA), or shown by analyzing their factorability using the Schmidt decomposition [52, 53]. Under such conditions, heralding a signal photon by detecting its idler companion results in the signal photon being left in a spectrally mixed state [54] that does not yield high visibility in quantum interference measurements.

Recent works in this area focus on spectrally engineered SPDC sources to create factorable biphotons for generating pure-state heralded single photons. One approach is to create an elongated JSA oriented along the idler (or signal) frequency axis with rectangular symmetry [55, 56], as demonstrated in [56], which showed 94.4% visibility in Hong-Ou-Mandel interference (HOMI) [57] between two independent heralded

photons at 830 nm that was observed without spectral filters. The other approach, as employed in this work, is to create a circularly symmetric JSA at a more convenient telecommunication wavelength in PPKTP.

In a low-flux, perturbative treatment of SPDC, the biphoton output has the frequency-domain representation [58]

$$|\psi\rangle_{si} \propto \int \frac{d\omega_s}{2\pi} \int \frac{d\omega_i}{2\pi} \varepsilon_p(\omega_s + \omega_i)\Phi(\omega_s, \omega_i) \, |\omega_s\rangle_s \, |\omega_i\rangle_i \, , \tag{2.1}$$

where the integrand is the JSA, whose squared magnitude is the readily-measured joint spectral intensity (JSI). In Eq. (2.1), $\varepsilon_p(\omega)$ is the pump field, $\Phi(\omega_s, \omega_i)$ is the crystal's phase-matching function, and $|\omega_{s(i)}\rangle_{s(i)}$ is the single-photon signal (idler) state at frequency $\omega_{s(i)}$. Under extended phase-matching conditions [55, 58, 59], Φ is oriented diagonally (positively correlated) in signal-idler frequency space, whereas ε_p is anti-diagonally oriented in that space. Therefore ε_p and Φ are orthogonal in signal-idler frequency space and serve as two independent control parameters to shape the JSA to be circularly symmetric.

Several attempts to generate a circularly symmetric JSA utilized standard phase matching that has a sinc function dependence whose side lobes degrade circular symmetry [59, 60, 61, 62]. To recover the desired circular symmetry, a nonlinear crystal's phase-matching function can be modified to possess a Gaussian shape by engineering its nonlinearity profile [63], poling pattern [64, 65, 66], or poling periods [67]. Recently, we custom-fabricated a PPKTP crystal with a Gaussian phase-matching function [67, 46] to generate biphotons with a circularly symmetric JSI, as shown in Fig. 2-1. The JSI of Fig. 2-1(a) shows residual side lobes that are at least 24 dB lower than the main lobe, yielding the Gaussian signal and idler spectra of Fig. 2-1(b) by tracing over the other photon's spectrum in Fig. 2-1(a). We infer a heralded-state spectral purity of 99% if we assume the joint distribution of signal and idler amplitudes are transform limited in frequency and time [46]. Because the JSI contains no phase information, we could not verify that the generated biphotons were indeed factorable with near-unity heralded-state purity. Moreover, due to the limited spec-

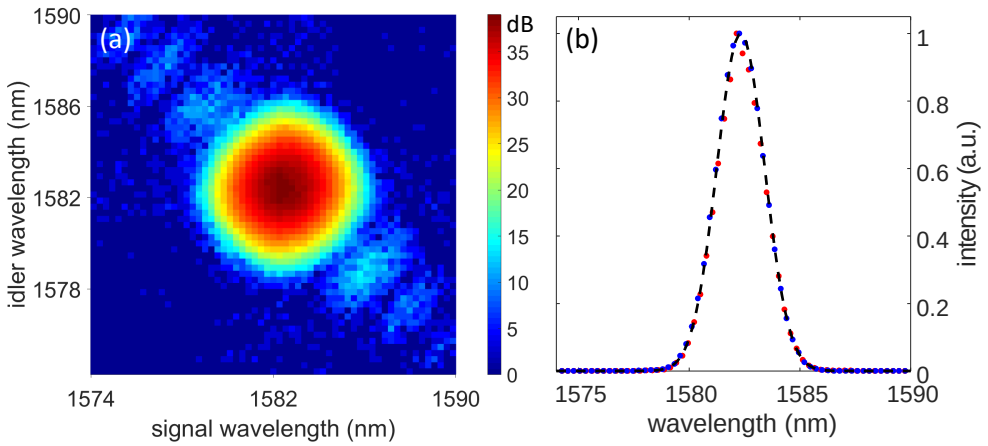

Figure 2-1: JSI and marginal distribution of biphotons generated from PPKTP with Gaussian phase matching and 1.0 nm pump bandwidth. (a) JSI, obtained from dispersion-based spectrometry with 40 km of fiber and 60-min integration time, showing weak residual side lobes. (b) Signal (red) and idler (blue) spectra and the Gaussian fit (dashed line).

tral resolution and range in the JSI measurement [68], the inferred value can only serve as an upper bound on the spectral purity. In this work, we first show theoretically that, given a circularly symmetric JSI, it is both necessary and sufficient to use a transform-limited Gaussian pump with an appropriate bandwidth to obtain a factorable biphoton state with transform-limited signal and idler. We then experimentally verify the heralded-state purity by performing HOMI between two independent heralded photons, obtaining a HOMI visibility of $93.9 \pm 1.8\%$ without filtering and $98.4 \pm 1.1\%$ with mild filtering of the SPDC output. Without correcting for accidental coincidences due to multipair events and dark counts, we obtained a heralded-state purity of 99.2%.

2.2 Theory of factorable biphoton and estimated heralded spectral state purity

To fully characterize the biphoton state requires measuring the spectral as well as the temporal correlations, as demonstrated recently [69, 70]. However, most measurements are performed in the spectral or temporal domain, but not both, rendering

these measurements incomplete. We cannot infer from a circularly symmetric JSI the factorability of the biphoton without assumptions. Given the Gaussian, circularly symmetric JSI of Fig. 2-1 together with a Gaussian phase-matching function [67, 46], we derive the necessary and sufficient conditions for a factorable biphoton state. We take the pump field's spectrum to be Gaussian

$$\varepsilon_p(\omega) = E_p(\omega_p)\exp[-(\omega-\omega_p)^2/4\sigma_p^2 - i\beta(\omega-\omega_p)^2/4], \tag{2.2}$$

where E_p is the pump field's amplitude at its center frequency ω_p, σ_p is its root-mean-square (RMS) bandwidth, and β is its second-order dispersion, in units of fs^2. We assume that the PPKTP crystal is phase matched at frequency degeneracy, satisfies the extended phase-matching condition [58], and has a Gaussian phase-matching function [67, 46]. We can then write the phase-matching function as

$$\Phi(\omega_s,\omega_i) = e^{-K\Delta k^2(\omega_s,\omega_i)} \approx e^{-K(k_s'-k_i')^2(\omega_s-\omega_i)^2}, \tag{2.3}$$

where $K>0$ is a constant proportional to the crystal length, $\Delta k(\omega_s,\omega_i) = k_p(\omega_s+\omega_i) - k_s(\omega_s) - k_i(\omega_i)$ is the phase mismatch, $k_{p(s,i)}(\omega)$ is the pump (signal, idler) wavenumber at ω, and $k'_{s(i)} = dk_{s(i)}/d\omega|_{\omega=\omega_p/2}$ is the inverse of the signal (idler) group velocity. The approximation in Eq. (2.3) is obtained by expanding the phase mismatch to second order at frequency degeneracy while imposing the extended phase-matching condition [58]. Inserting Eqs. (2.2) and (2.3) into Eq. (2.1), we find that a circularly symmetric JSI results if and only if the pump bandwidth is given by $1/4\sigma_p^2 = K(k_s'-k_i')^2$, in which case the signal and idler have RMS bandwidths $\sigma_s = \sigma_i = \sigma_p/\sqrt{2}$. To have a factorable biphoton state, i.e., a factorable JSA, we must also require a transform-limited (chirp-free) pump, viz., one whose second-order dispersion vanishes, $\beta=0$. The resulting factorable state then has transform-limited signal and idler photons:

$$|\psi\rangle_{si} \propto E_p(\omega_p)\int\frac{d\omega_s}{2\pi}e^{-(\omega_s-\omega_p/2)^2/2\sigma_p^2}|\omega_s\rangle_s\int\frac{d\omega_i}{2\pi}e^{-(\omega_i-\omega_p/2)^2/2\sigma_p^2}|\omega_i\rangle_i\,. \tag{2.4}$$

Heralded photons from the factorable state in Eq. (2.4) are in a spectrally pure state with a heralded-state purity $P = 1$. If the Gaussian pump field satisfies the bandwidth condition for a circularly-symmetric JSI, but is not transform limited because of $\beta \neq 0$, the dispersive term $\exp[-i\beta(\omega - \omega_p)^2/4]$ in Eq. (2.2) introduces a JSA phase term that is proportional to the product of the signal and idler frequencies, which decreases their heralded-state purities. The degraded purity can be quantified by performing a Schmidt decomposition on the SPDC signal (idler) state [71, 72]: $P = 1/\sqrt{1 + \beta^2\sigma_{s(i)}^4}$. Our theory implies that the heralded-state purity depends on both the pump's spectrum and its second-order dispersion, which is consistent with the theoretical and numerical analysis in [73, 68]. Furthermore, our analysis shows that measurements of the transform-limited Gaussian pump and the circularly symmetric JSI are sufficient to ensure a high-purity factorable SPDC output state.

2.3 Hong-Ou-Mandel interference between independently generated heralded photons

To verify the high purity of the SPDC output state experimentally, we measured the HOMI visibility between two heralded signal photons generated by the same SPDC source at two different times. High HOMI visibility can only occur if the heralded photons are spectrally pure.

2.3.1 Pump pulse engineering

To generate spectrally pure heralded photons, the pump needs to be Gaussian and transform-limited. In this section, we examine the effects of the pump in three different cases: (i) transform-limited pump, $\beta = 0$, with a non-Gaussian profile, (ii) Gaussian pump with nonzero second-order dispersion $\beta \neq 0$, and (iii) transform-limited Gaussian pump.

Figure 2-2 shows the experimental setup for SPDC biphoton generation and HOMI measurement of two time-separated heralded signal photons. The SPDC pump was

derived from an 80-MHz mode-locked Ti:Sapphire laser centered at 791 nm with a maximum full width at half-maximum (FWHM) bandwidth of 7.8 nm. To modify the pump bandwidth, we implemented a linear spectral filtering system using a pair of identical diffraction gratings in a $4f$ optical configuration [74, 75]. Two identical lenses with focal length $f = 20$ cm were placed $2f$ apart, and the two diffraction gratings were located a distance f from the lenses, as shown in Fig. 2-2(a). The first grating spatially dispersed the broadband pump's spectral components that were then focused by the first lens at the Fourier plane located at a distance f from the lens. We placed an apodizing mask at the Fourier plane to shape the pump spectrum. The type of mask and its exact placement determined the pump's spectrum and second-order dispersion.

The pump at the input to its spectral filtering setup had a FWHM bandwidth of 6.25 nm as determined by an optical spectrum analyzer. We note that the pump's FWHM deviates from its maximum value of 7.8 nm because the laser was driven at a lower current at the time of this particular measurement. The direct output of the mode-locked pump laser should have approximately a sech^2 pulse shape, and our aim was to modify its shape to be Gaussian with a transform-limited bandwidth of $\sim$1 nm. In order to check if the pump was transform limited we measured the pulse duration of the pump before and after the $4f$ setup without an apodizing mask. The pulse width measurement was done by autocorrelation based on second harmonic generation. We obtained a pulse broadening ratio of 1.2 which corresponds to a second-order dispersion of $\beta = 8{,}578$ fs^2. The pulse broadening observed can be caused by aberrations, spatial chirp, or imperfect alignment. This amount of dispersion is negligible for a pump bandwidth of $\sim$1 nm that we used to produce the joint spectral intensity (JSI) in Fig. 2-1.

At the Fourier plane we placed an adjustable slit to reduce the pump bandwidth to 1.0 nm and to obtain a Gaussian shape. That hard-aperture mask, however, has a rectangular transmission profile and does not result in a Gaussian spectral profile, while the pump remained transform limited. By trial and error, we moved the slit several mm away from the Fourier plane to obtain a Gaussian shape. This maneu-

ver reduced the filtered pump power and caused the pump to acquire an appreciable amount of dispersion. In order to have both a Gaussian spectrum and negligible dispersion, we chose to use a Gaussian transmission mask [76]. We collaborated with colleagues at the National Institute of Standards and Technology (NIST) who fabricated multiple transmission masks lithographically on a single 2-mm thick chromium mask. Our Gaussian transmission mask consists of 16 individual strips of 2000 $\times$ 200 opaque squares each measuring 4 μm in size. Each strip had a Gaussian spatial distribution of the opaque squares spread over slightly different strip widths that effectively imposed a pump bandwidth range 0.61–1.15 nm in 0.003 nm increments. In Sect. 2.3.2, we show the HOMI results for the three mask choices: slit at the Fourier plane that produces a transform-limited non-Gaussian pump, slit away from the Fourier plane that produces a non-transform-limited Gaussian pump, and the Gaussian transmission mask at the Fourier plane that produces a transform-limited Gaussian pump. The pump beam is then focused onto the crystal with a beam waist of 110 μm. The generated SPDC photons are collected with a collection beam waist of $\sim 90\mu$m.

After the pump spectral filter, we loosely focused the pump beam at the center of the PPKTP crystal that was temperature stabilized at 22.4 ± 0.1°C for operating at wavelength degeneracy with signal and idler outputs at 1582 nm. Reference [46] provides details of the custom PPKTP crystal featuring a Gaussian phase-matching profile under extended phase matching. After propagation through the crystal, the pump was removed by a long-pass filter with a 1300-nm cutoff wavelength. The orthogonally polarized signal and idler were coupled into a single-mode polarization-maintaining (PM) fiber, and then separated by a fiber-based polarization beam splitter (PBS) into their respective channels. At 1 mW of pump power we detected signal and idler singles of ~3,000/s and ~3,200/s, respectively, and signal-idler coincidences of ~1,200/s, which implies a system efficiency of $\sim 38\%$ and a correlated mode coupling efficiency of $\sim 80\%$ [77].

We configured the setup of Fig. 2-2(b) to measure the HOMI between two heralded signal photons separated by 8 mode-locked pulses or ~100.7 ns, chosen to be greater

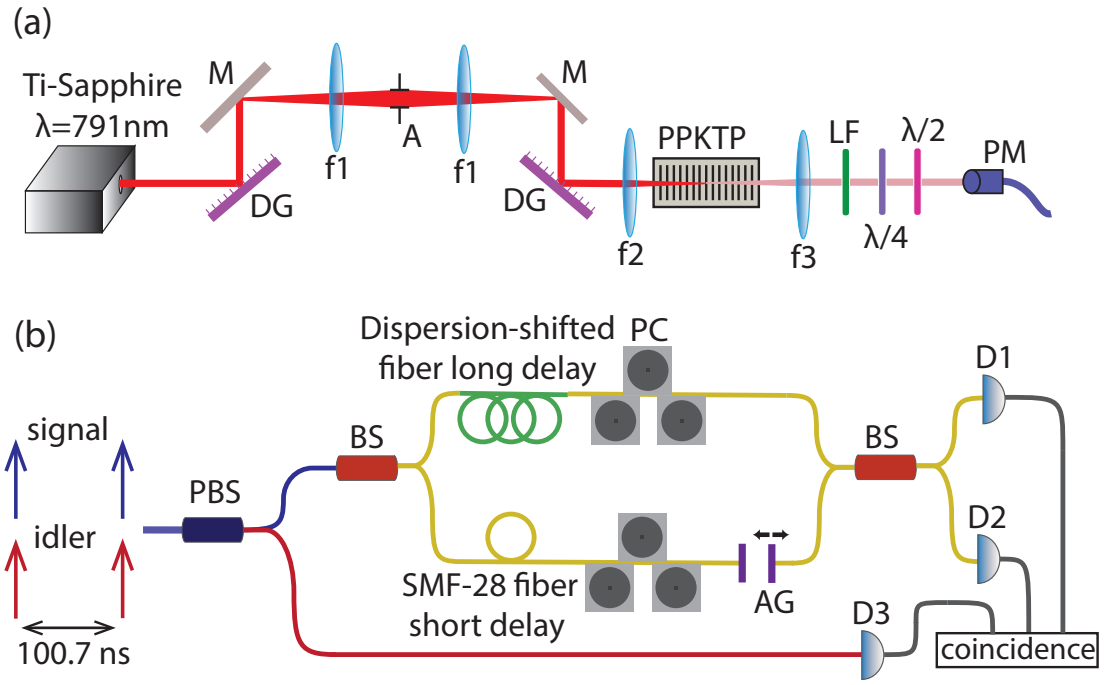

Figure 2-2: Experimental setup. (a) Pump and SPDC configuration; (b) heralded-photon HOMI measurement. Long-path fiber delay consists of 29.95 m of dispersion-shifted fiber and short-path fiber delay uses 9.95 m of SMF-28 fiber. DG, diffraction grating; A, apodizing mask; LF, long-pass filter; PM, polarization-maintaining fiber; $\lambda/2$, $\lambda/4$, half-wave and quarter-wave plates; D1–D3, superconducting nanowire single-photon detectors; PBS, polarization beam splitter; BS, 50:50 beam splitter; PC, polarization control paddles; AG, air gap.

than the ∼80-ns detector deadtime of our superconducting nanowire single-photon detectors (SNSPDs). The performance of SNSPDs is shown in Appendix C. After the fiber PBS, the idler photons were directed to SNSPD D3 for detection to herald the presence of the signal photons. The signal photons went through a 50:50 beam splitter (BS) that randomly sent them to the long-path delay or short-path delay. Given two idler detection events that are separated by ∼100.7 ns, there is a 25% chance that the first heralded signal photon went through the long path and the second heralded signal photon passed along the short path. The path difference was adjusted to match the time separation of 8 mode-locked pump pulses, so that the two heralded signal photons would interfere at the second BS before detection at SNSPDs D1 and D2. A successful HOMI data point is a four-fold coincidence event: two idler D3 detections separated by 100.7 ns and simultaneous signal detection at D1 and D2. All detection events were recorded using a time tagger. The long path was constructed of dispersion-shifted fiber so that the two paths introduced the same amount of dispersion, and the relative path delay (excluding the 100.7 ns path length difference) was adjusted using a movable air gap. Although the photon pairs are generated by different pulses from the same pump laser, the heralded photons have a random phase relationship because of phase diffusion of the SPDC process [78, 79]. Therefore, our results also apply to heralded photons generated from two independent sources.

We recorded the 4-fold coincidence events with a 2 ns coincidence gate as we varied the relative delay between the long and short paths. The zero delay position was assigned to the location where the two signal photons arrived at the BS at the same time. We use the standard HOMI visibility definition $V = (N_{\max} - N_{\min})/N_{\max}$, where $N_{\max(\min)}$ represents the maximum (minimum) coincidence counts. For a heralded state with purity P, $N_{\min} \approx N_{\max}(1 - P^2)$, implying $V = P^2$.

2.3.2 HOM interference results

Initial measurements were made with a hard-aperture mask. Adjusting the hard aperture location lets us optimize the pump's second-order dispersion or its spectrum,

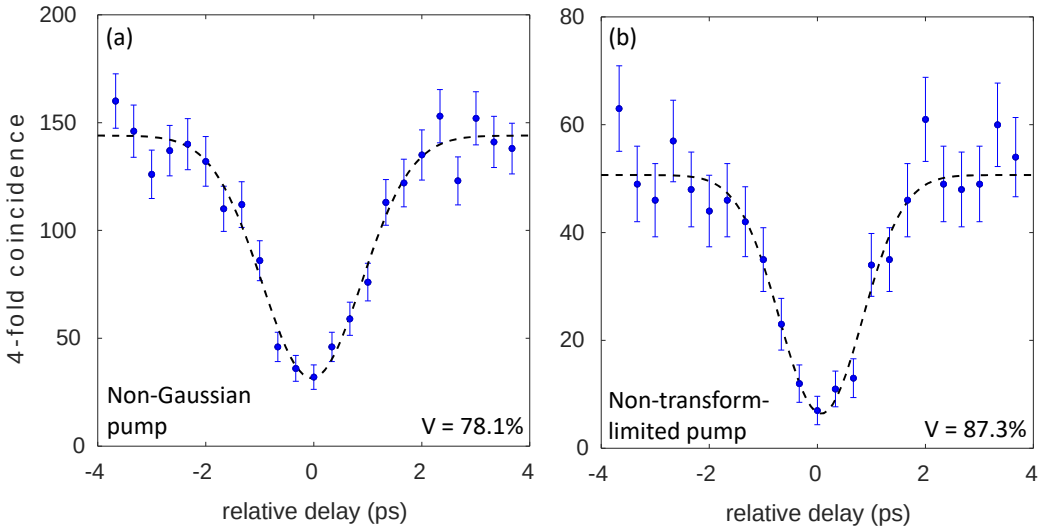

Figure 2-3: HOMI measurements using a hard-aperture mask for controlling the pump properties. (a) Non-Gaussian zero-dispersion pump; (b) Non-transform-limited Gaussian pump. No spectral filtering of the SPDC output was used. Each data point represents a 5-min measurement and no background subtraction is applied. Error bars are one standard deviation due to Poisson noise and the dashed curves are Gaussian fits.

but not both simultaneously. We obtained 78.1% HOMI visibility for a transform-limited non-Gaussian pump in Fig. 2-3(a) and 87.3% for a Gaussian pump that was not transform limited in Fig. 2-3(b), in agreement with our theory that the pump being Gaussian or transform limited, but not both, is not sufficient for obtaining high visibility HOMI.

We then used the custom NIST-fabricated Gaussian transmission mask [76] that shaped the transform-limited pump to have a Gaussian spectrum. A pump with 15 mW of power and 1.0 nm bandwidth produced a mean SPDC photon pair per pulse $\alpha = 0.002$, and we measured HOMI visibility of $V = 93.9 \pm 1.8\%$ without spectral filtering of the SPDC output, as shown in Fig. 2-4(a). For $\alpha \approx 0.003$ (at 20 mW of pump), we obtained a lower visibility $V = 91.6 \pm 1.5\%$ because the higher pump power produced more multi-pair events and therefore increased accidental coincidences. At $\alpha = 0.003$ we changed the pump bandwidth to 0.97 nm and 1.05 nm and obtained visibilities of $89.1 \pm 2.1\%$ and $90.6 \pm 1.9\%$, respectively, thus confirming that the pump bandwidth of 1.0 nm was optimal. We note that the reported visibilities are the

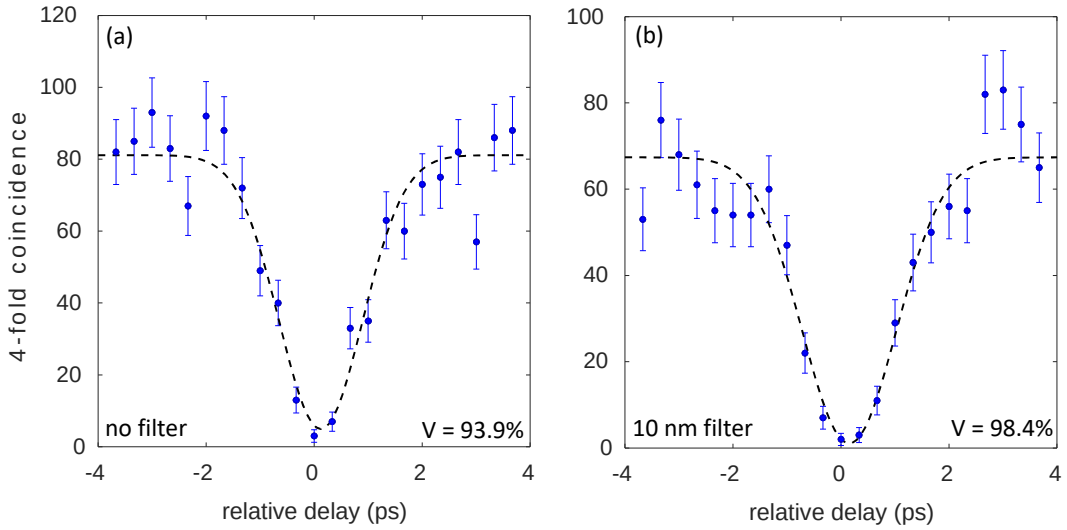

Figure 2-4: HOMI measurements using a Gaussian transmission mask at $\alpha = 0.002$: (a) without spectral filtering, and (b) with a 10 nm filter. Each data point represents a 5-min measurement without background subtraction. Error bars are one standard deviation due to Poisson noise and the dashed curves are Gaussian fits.

Gaussian fitted results along with the fitted uncertainties. Compared with a similar experiment at 1550 nm with a domain-engineered crystal reporting HOMI visibility of $90.7 \pm 0.3\%$ [66], our results show visibility improvements partly because we operated at the optimal wavelength for PPKTP's extended phase-matching condition.

In order to reduce the weak residual side lobes in Fig. 2-1's JSI, we sent the SPDC output through a 10-nm filter with near-unity transmission for the 6-nm center portion (compared with 2.62 nm bandwidth of heralded photons) so that the SPDC flux remained about the same and the Gaussian spectrum was not disturbed (see Appendix A). With this filter we measured $V = 98.4 \pm 1.1\%$ ($96.9 \pm 1.2\%$) for $\alpha = 0.002$ (0.003), as shown in Fig. 2-4(b). The measured HOMI visibility of 98.4% corresponds to 99.2% heralded-state spectral purity without background corrections, in agreement with our previous estimate of the heralded-state purity of mildly-filtered SPDC under the assumption of a transform-limited biphoton state [67].

2.4 Conclusion

We have generated heralded single photons with high intrinsic spectral purity of 99.2% by use of a custom Gaussian phase-matching profile in PPKTP and a transform-limited Gaussian pump. We verified the heralded-state purity by performing a four-fold coincidence measurement of HOMI between two time-separated heralded photons, obtaining an interference visibility of 98.4% without correcting for degradation due to dark counts and multi-pair effects. We also showed, theoretically, that given a circularly symmetric Gaussian JSI and a Gaussian phase-matching function, it is necessary and sufficient to achieve a factorable biphoton state if the pump has a transform-limited Gaussian spectrum. Our technique can be easily replicated and the generated single-spatiotemporal-mode heralded photons can be utilized in many measurement-based quantum information processing applications that involve interference between independent single photons.

Chapter 3

Frequency shifter based on quadrature phase-shift keying modulator

Manipulating single photons in the frequency domain is essential in realizing future quantum network systems. This chapter will study the method of shifting a single photon's frequency using a commercially available quadrature phase-shift keying (QPSK) modulator. We demonstrate frequency shifting on single photons and show that the frequency-shifted photons preserve their original quantum state in other degrees of freedom through Hong-Ou-Mandel interference (HOMI) measurement.

Part of the material presented in this chapter has been published and is reproduced from Sci. Rep. **11**, 1-7 (2021) [80].

3.1 Introduction

Photons are the carriers of choice for conveying quantum information over long distances to realize a scalable quantum internet owing to their weak interaction with the environment and their low-loss propagation in optical fiber [81, 82]. Quantum information can be encoded in various photonic degrees of freedom, e.g., momentum, spatial mode, polarization, and frequency, which requires that these properties

be precisely controlled. Although the momentum, spatial, and polarization modes of single-photon states can be easily manipulated with active or passive photonic components [83], the control of frequency modes is less simple.

Spectral mode control is of particular interest in quantum networking. For example, the choice of optical wavelengths is often dictated by particular tasks such as low-loss long-distance transmission through optical fibers (telecommunication band around 1.55 μm) or efficient interaction with atomic, ionic, or superconducting qubits. Fine frequency adjustments in the radio and microwave frequency ranges are just as important because fine tuning and matching the frequency spectra of photons from independent sources is required to ensure they produce high-fidelity quantum interference. For large frequency shifts on the order of terahertz or tens of terahertz, one relies heavily on nonlinear optical processes that work only at specific wavelengths and require strict phase-matching conditions [84, 85, 86, 87]. Of interest in this work are small frequency shifts in the gigahertz to tens of gigahertz range.

3.1.1 Shifting frequency with electro-optical devices

One method to deterministically shift a single photon's frequency by ω_m is to apply a linear phase ramp $\phi(t) = \omega_m t$ over the entire wave packet of the photon, which can be realized using a fast electro-optic modulator [88] or optomechanical waveguide [89]. The resulting single-photon frequency will be shifted by ω_m by the Fourier transform's frequency shift property. Typically, a single pulse experiences a time-varying linear phase when passing an electro-optical device driven by sinusoidal radio-frequency (RF) voltage signal $V(t) = V_0 \sin(2\pi f t + \phi_0)$, where V_0 is the driving voltage amplitude, f is the RF signal frequency, and ϕ_0 is the phase delay between the RF signal and the optical pulse. The optical pulse and the RF signal have to be in a stable phase relation, and the optical pulse needs to be much shorter than the RF signal period, which is defined as $T = 1/f$. In this case, the rising edge or the falling edge of the RF signal can be viewed as a linear phase upward or downward ramp. The spectral

shift amount can be approximated as [88]:

$$\omega_m \approx \pm 2\pi^2 (V_0/V_\pi) f, \tag{3.1}$$

where V_π is the voltage required to achieve a π phase shift for the electro-optical device. Using this scheme, a phase shift of $\pm$200 GHz can be achieved. A combination of parameters optimization, for example, lower V_π, higher RF frequency f, and greater RF amplitude V_0, is needed to achieve a larger frequency shift. However, higher RF frequency f and greater RF amplitude V_0 introduce difficulty in synchronizing the RF signal and the single-photon pulse. The resulting phase jitter broadens the output photon's spectral bandwidth, degrading the shifted photons' quality. Recently an ultralow-voltage electro-optical modulator has been fabricated on lithium niobate thin-film platform that has a V_π of 2.3 V at 27.5 GHz, comparing to a 7 V V_π in commercial bulk lithium niobate modulator. This record-low V_π is made possible by lithium niobate thin-film and the configuration that extends the modulation range by two times. A frequency shift of $\pm$600 GHz has been achieved using this particular modulator [90].

3.1.2 Shifting frequency with acousto-optic modulator

For smaller frequency shifts, it is also possible to use an acousto-optic modulator as a frequency shifter [91]. In an acousto-optic modulator, sound waves produce a refractive index grating in the material that diffracts the incoming single photons. A typical acousto-optic modulator operates under the Bragg condition, where the incident light comes at the Bragg angle θ_B [92]:

$$\sin\theta_B = \frac{K}{2k} = \frac{\lambda}{2\Lambda n_{\text{eff}}}, \tag{3.2}$$

where $k = 2\pi n_{\text{eff}}/\lambda$ is the optical wavenumber with n_{eff} being the optical mode index and λ being the optical wavelength. K is the acoustic wavenumber given by $2\pi/\Lambda$ with Λ being the acoustic wavelength. Typical acousto-optic modulators can only

impose a shift frequency on the order of megahertz, but a recent demonstration has shown a 3 GHz acousto-optic frequency shifter in thin-film lithium niobate, featuring a carrier suppression of more than 30 dB [92].

3.1.3 Shifting frequency with quadrature phase-shift modulator

One can obtain frequency shifts based on optical single sideband (OSSB) modulation, which has been demonstrated for cw lasers using electro-optic modulators [93, 94, 95, 96]. More recently, Lo and Takesue used a custom OSSB modulator to impose frequency shifts on single photons and they demonstrated its effectiveness by obtaining high visibility Hong-Ou-Mandel interference (HOMI) of two initially frequency-distinguishable SPDC photons [97].

In this chapter, we report implementing the same OSSB approach of Lo and Takesue [97] and achieving similar HOMI-visibility results by repurposing a commercially available quadrature phase-shift keying (QPSK) modulator as an OSSB frequency shifter. The availability of well-packaged commercial components allows for simpler and faster setup and typically offers better specifications than devices custom made for quantum photonics research. We characterized a commercial QPSK modulator for frequency shifting of single photons and compared spectra before and after the shift to show we realized a carrier-to-sideband ratio (CSR) of 30 dB. The frequency shifting technique also works well on a broadband source, showing high CSRs of > 20 dB over its 2.4-THz spectrum. We observe significant improvement in HOMI visibility when we applied an appropriate frequency shift to one of two interfering SPDC photons whose initial frequency spectra overlapped only partially. Our frequency shifter based on a commercial QPSK modulator is thus a convenient and useful device for many quantum communication applications such as providing unconditional security for high-dimensional quantum key distribution system [35, 33, 98, 99] and making fine frequency adjustment to single photons for quantum information storage in solid-state quantum memories [100]. With additional intensity and phase control,

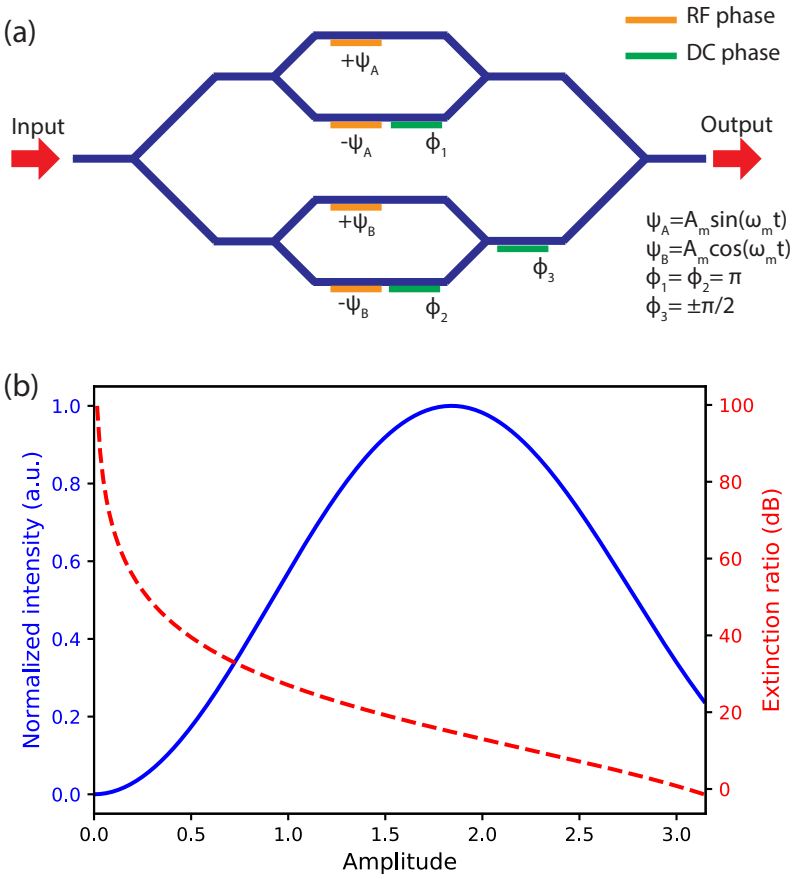

Figure 3-1: (a) Schematic of QPSK modulator with two radio-frequency (RF) phase modulators and three static phase shifters. All beam splitters and combiners are 50/50 coupled. (b) Shifted signal intensity (solid blue curve) and minimum extinction ratio (dashed red curve) as a function of driving amplitude A_m. The intensity of the shifted signal is normalized to the theoretical maximum value.

the frequency shifter can also be used as a quantum pulse shaper for precise temporal and spectral mode tuning in a dense frequency-multiplexed quantum communication network [101].

3.2 Mathematical model of QPSK modulator

The QPSK modulator shown in Fig. 3-1(a) consists of two independent Mach-Zehnder interferometers embedded in a Mach-Zehnder interferometer superstructure. Optical inputs to the modulator must be linearly polarized with alignment along the z-axis of the modulator's lithium niobate waveguide. The radio-frequency (RF) mod-

ulators in the top and bottom interferometers are driven by orthogonal RF signals $\Psi_A = A_m \sin\omega_m t$ and $\Psi_B = A_m \cos\omega_m t$, respectively, in a push-pull ($\pm\Psi_A$ and $\pm\Psi_B$) configuration, where A_m is the RF signal amplitude and ω_m is the RF signal frequency. Using the Jacobi-Anger expansion, we can express these phase modulations as

$$e^{iA_m \sin\omega_m t} = \sum_{k=-\infty}^{\infty} J_k(A_m) e^{ik\omega_m t}, \quad e^{iA_m \cos\omega_m t} = \sum_{k=-\infty}^{\infty} i^k J_k(A_m) e^{ik\omega_m t}, \tag{3.3}$$

where $J_k(A_m)$ is k-th Bessel function of the first kind. For an input field with amplitude E_0 and center frequency ω_0, $E_{in}(t) = E_0 e^{i\omega_0 t}$, the output field from the QPSK modulator can be written in harmonics of the RF signal frequency ω_m as

$$E_{out}(t) = \frac{E_0}{4} e^{i\omega_0 t} \sum_{k=-\infty}^{\infty} J_k(A_m) e^{ik\omega_m t} \Big[1 + (-1)^k e^{i\phi_1} + \left(1 + (-1)^k e^{i\phi_2}\right) i^k e^{i\phi_3} \Big], \tag{3.4}$$

where ϕ_1, ϕ_2, and ϕ_3 are constant phase shifts imposed at the QPSK modulator, as indicated in Fig. 3-1(a). To operate the QPSK modulator as a frequency shifter, we set $\phi_1 = \phi_2 = \pi$ and $\phi_3 = -\pi/2$ ($\pi/2$) for frequency blue (red) shift. For blue-shift operation, Eq. (3.4) simplifies to

$$\begin{aligned} E_{out}(t) &= \frac{E_0}{4} e^{i\omega_0 t} \sum_{k=-\infty}^{\infty} J_k(A_m) e^{ik\omega_m t} \left(1 + (-1)^{k+1}\right) \left(1 - i^{k+1}\right) \\ &= E_{in}(t) \Big[\ldots + J_{-3}(A_m) e^{-i3\omega_m t} + J_1(A_m) e^{i\omega_m t} + J_5(A_m) e^{i5\omega_m t} + \ldots \Big] \end{aligned} \tag{3.5}$$

the latter showing the three lowest non-zero harmonics. Eq. (3.5) shows that the output carrier is frequency shifted from ω_0 to $\omega_0 + \omega_m$ with amplitude $J_1(A_m)$, and that the two nearest sidebands have frequencies $\omega_0 - 3\omega_m$ and $\omega_0 + 5\omega_m$ with amplitudes $J_{-3}(A_m)$ and $J_5(A_m)$, respectively. We define the CSR for a specific sideband to be $\mathrm{CSR}_k = |J_1(A_m)/J_k(A_m)|^2$ for $k \neq 1$. In Fig. 3-1(b) we plot the intensity of the frequency-shifted signal $|J_1(A_m)|^2$ (solid blue curve) and the minimum extinction ratio (dashed red curve), given by $\min_{k\neq 1} \mathrm{CSR}_k$, versus the RF signal amplitude A_m. Figure 3-1(b) shows clearly the competing effects of maximizing the frequency-shifted

carrier signal and suppressing the sidebands as a function of RF signal strength A_m. At $A_m = 1.8$, the frequency-shifted signal reaches its theoretical maximum and is 4.7 dB below the input intensity, if we exclude the system's insertion and coupling losses. However, under this driving condition, the minimum extinction ratio is only 15 dB, which may not be sufficient for certain quantum applications as these sidebands act as noise sources that degrade quantum measurements. In order to further suppress the sidebands at undesirable frequencies, one needs to operate the modulator at lower RF amplitudes resulting in lower frequency-shifted signal strengths. For example, at $A_m = 0.85$, the shifted signal decreases to 44% of the theoretical maximum but the minimum extinction ratio increases to 30 dB.

3.3 Measurements of shifted spectra of cw laser light, frequency comb, and single photons

The QPSK modulator we used was a Fujitsu model FTM7961EX, with a 3 dB RF bandwidth of 22 GHz and a V_π of less than 3.5 V. Its specified operational optical-wavelength range is from 1530 to 1610 nm, and we measured an optical insertion loss of 5.2 dB. The modulator can only transmit a linearly-polarized input aligned to the designed polarization for modulation in the lithium niobate waveguide. The 15.65 GHz RF signal was derived from an RF frequency synthesizer, amplified and split by a 0°-phase 50/50 power splitter to serve as inputs to the QPSK modulator's top and bottom interferometers. The two cables connecting the two splitter outputs to the modulator had a 10.96 cm length difference, corresponding to a $\pi/2$ phase shift, that was chosen to ensure orthogonality of the two driving RF signals, Ψ_A and Ψ_B, as indicated in Fig. 3-1(a). We also set the static phase shifts to $\phi_1 = \phi_2 = \pi$ and $\phi_3 = -\pi/2$ for a blue frequency shift.

To characterize the performance of the QPSK modulator as a frequency shifter we first used a cw laser with sub-MHz linewidth at $\omega_0/2\pi = 192.1$ THz (1560 nm wavelength) as its optical input. The RF modulation signal was set to perform an

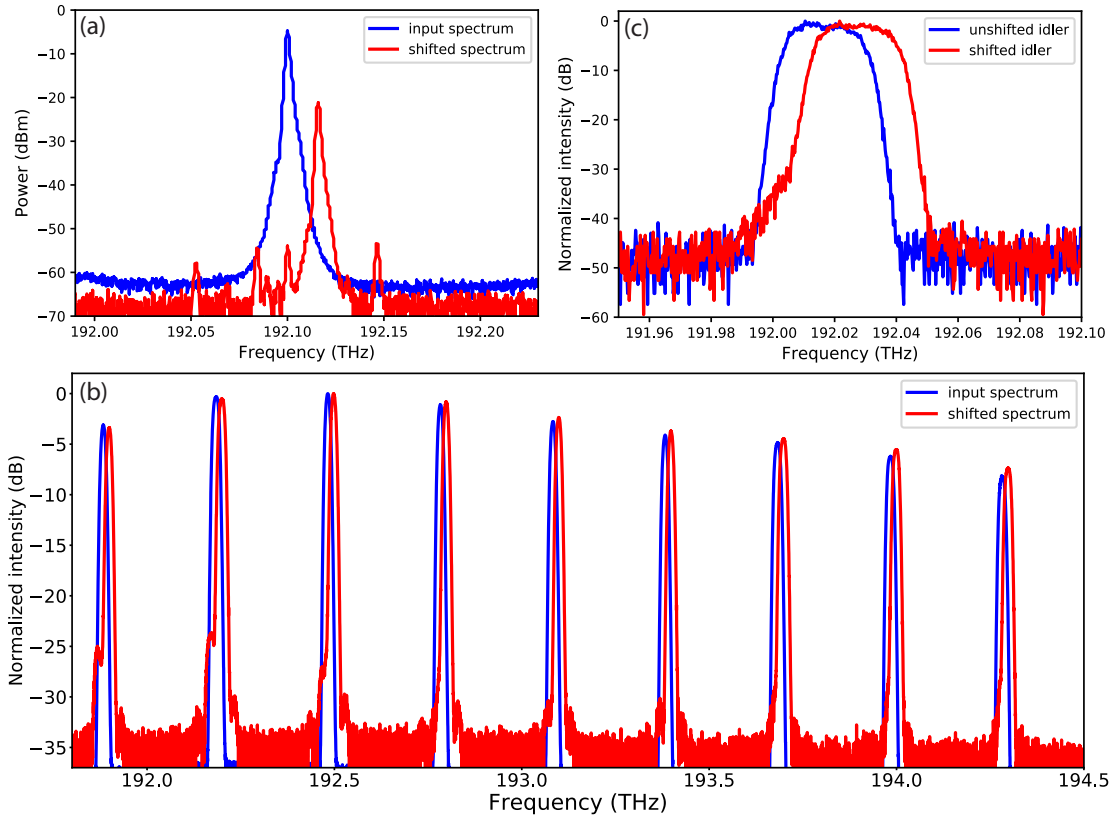

Figure 3-2: Input and output spectra for different input optical sources to the QPSK-modulator frequency shifter. (a) Spectra of the cw laser before and after the frequency shift. (b) Spectra of the frequency comb before and after the frequency shift, normalized to the maximum intensity. (c) Spectra of the idler photon before and after the frequency shift, normalized to the maximum detected signal-idler coincidence counts.

$\omega_m/2\pi$ = 15.65 GHz blue shift. Figure 3-2(a) shows the input and output spectra of the cw laser source for an RF amplitude $A_m = 0.57$, clearly showing the shift in frequency that we measured to be 16 GHz, limited by the 2-GHz resolution of our optical spectrum analyzer. The frequency shifted output power was measured to be 16.4 dB lower than the input power, a value that is accounted for by the expected drop in power, $|J_1(0.57)|^2 = -11.2$ dB, and the QPSK modulator's 5.2 dB insertion loss. The choice of $A_m = 0.57$ allows us to evaluate the CSRs. Figure 3-2(a) shows that there are 4 residual sidebands at $-3\omega_m$, $-\omega_m$, 0, and $3\omega_m$. The $-3\omega_m$ sideband is expected to have the largest amplitude according to Eq. (3.5) with $\text{CSR}_{-3} = 37$ dB for $A_m = 0.57$ that matches the measured value. However, Eq. (3.5) also predicts that the sidebands at $-\omega_m$, 0, and $3\omega_m$ should have zero amplitude, whereas their non-zero peaks in Fig. 3-2(a) yield CSRs of ∼32 dB, which is the minimum extinction ratio of this measurement. The appearance of these three residual sidebands was likely caused by a slight difference in the splitting ratios of the 50/50 couplers within the QPSK modulator so that these sidebands did not completely cancel through destructive interference at the modulator's output. Another nonideality of the QPSK modulator is that the static phase shifts ϕ_1, ϕ_2, and ϕ_3 may drift due to thermal fluctuations in the phase shifters and cause the frequency shifting operation to degrade. In a separate measurement to check the stability of the QPSK modulator, we found the minimum extinction ratio decreased from 32 dB to 18 dB over 110 min due to phase drifts, and that the extinction ratio could be restored to 32 dB by adjusting the voltages of the phase shifters at the end of the 110-min duration.

Next we examined the frequency shifting operation for a broadband optical input to the QPSK modulator. From a broadband amplified spontaneous emission source we used a programmable intensity filter in the frequency domain to carve out a frequency comb spanning a ∼2.4 THz bandwidth. The programmable intensity filter was a Finisar model 1000S waveshaper. This waveshaper provides control of the transmitted intensity from 0 dB to 50 dB attenuation at 1 GHz resolution over the entire telecommunication C band. The minimum optical bandwidth of the waveshaper was measured to be 12 GHz, limited by the point-spread function of the waveshaper's

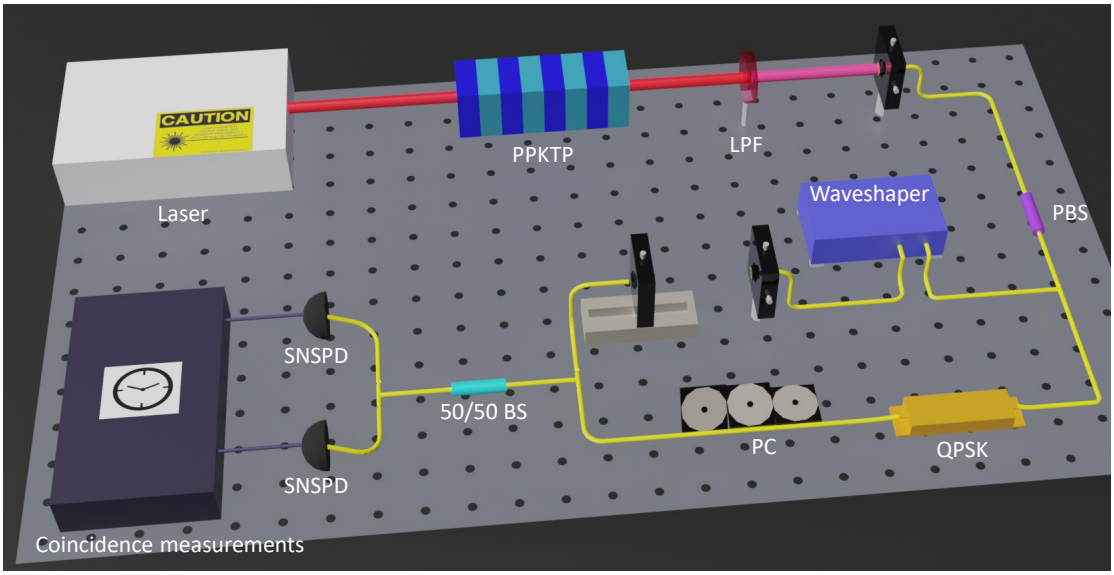

Figure 3-3: Schematic of the HOMI experiment. PPKTP: periodically-poled potassium titanyl phosphate crystal; LPF: long pass filter; PBS: polarizing beam splitter; QPSK: quadrature phase-shift keying modulator; PC: polarization control; 50/50 BS: 50/50 beam splitter; SNSPD: superconducting nanowire single-photon detector.

optics, and we measured its insertion loss to be 5 dB. The frequency comb consisted of 20-GHz-wide comb teeth spaced at 300 GHz intervals. The RF driving conditions of the QPSK modulator were the same as those used for the cw laser input, and we optimized the setting to yield the highest minimum extinction ratio at optical frequency 193.4 THz (1550 nm wavelength). The spectra of the frequency comb before and after the QPSK-modulator frequency shifter are displayed in Fig. 3-2(b), showing clearly that the entire spectrum was shifted by ∼16 GHz. We found that the minimum extinction ratio, optimized at 193.4 THz to yield 32 dB, decreased at frequencies lower than 193.4 THz, with the residual sideband peaks clearly visible in the lowest three comb lines at 191.9, 192.2, and 192.5 THz. The minimum extinction ratio for the 191.9 THz comb line was 22 dB. For the rest of the comb lines spanning more than 1.5 THz, the minimum extinction ratio of at least 30 dB was maintained. The measurements indicate that the QPSK modulator works well as a broadband optical frequency shifter but the extinction ratios can be uneven over a large bandwidth.

Additionally, we further examined the performance of the QPSK-modulator frequency shifter with heralded single photons as its optical input. From a type-II phase-

matched periodically-poled potassium titanyl phosphate (PPKTP) waveguide [102] SPDC source we generated signal and idler photon pairs whose center wavelength was ∼1560 nm. The signal and idler were partially overlapping in frequency and had a spectral full-width at half maximum bandwidth of 320 GHz. The signal and idler wave packets were time coincident within 2 ps. After the pump was filtered out by a long-pass filter (Semrock BLP02-1319R-25), the orthogonally-polarized signal and idler were coupled into a polarization-maintaining (PM) fiber. The orthogonally-polarized photons were separated by a polarizing beam splitter and sent to separate superconducting nanowire single-photon detectors (SNSPDs) with their arrival times recorded by a time tagger. Signal-photon detections were used to herald the presence of their idler-photon companions. We used the programmable intensity filter to implement a 50 GHz flat-top spectral filter on the signal photons that, by virtue of frequency entanglement, projected the corresponding idler photons to also have a 50 GHz spectrum centered at 192.014 THz. We sent the idler photons through a fiber Bragg-grating dispersion module for spectral analysis via time-to-frequency conversion [46]. The fiber Bragg grating based dispersion module was manufactured by Proximion and imposes a dispersion amount of 10 ns/nm for inputs from 1558.58 nm to 1562.23 nm. Due to the imposed dispersion, the idler's different spectral components propagated at different speeds resulting in different arrival times relative to the signal photon. Hence the idler spectrum can be obtained from the arrival time relative to that of the signal. In this particular measurement, we achieved a spectral resolution of 1.8 GHz, set by the Bragg-grating module's spatial dispersion and the SNSPD's timing jitter. We used the arrival times of idler photons at 1562.23 nm as a reference to convert the photons' arrival times to frequencies. Figure 3-2(c) shows the measured spectra of heralded idler photons before and after the frequency shift. The measured data are normalized to the maximum detected coincidence counts to remove the influence of the different transmission losses before and after measurements. The 15.65 GHz frequency shift of the single photon spectrum is clearly observed. The original spectrum is suppressed by 30 dB and is consistent with our measurement using the cw laser source as input in Fig. 3-2(a). Our results demonstrate the abil-

ity to deterministically modify the spectral components of nonclassical light using a commercial QPSK modulator configured as a frequency shifter.

3.4 Hong-Ou-Mandel interference of photon pairs

Hong-Ou-Mandel interference [57], which measures the indistinguishability of two single photons, is an essential measurement tool in quantum photonics making the ability to fine tune the frequency of single photons to best match their spectra highly desirable. Figure 3-3 is the schematic of our HOMI measurement that utilized corrective frequency shifting to recover HOMI visibility by making the two interfering photons spectrally indistinguishable. The photon pairs were generated by the same cw SPDC source used for Fig. 3-2(c)'s single-photon frequency-shifting measurements. After the orthogonally-polarized signal and idler were separated, the signal photon was shaped by the programmable intensity filter to have a 50-GHz flat-top spectrum with a tunable center frequency. The corresponding idler, which also possessed a 50-GHz spectrum, went through the QPSK-modulator frequency shifter before recombining with the signal photon for HOMI coincidence measurements detected with two SNSPDs and then time tagged. Our niobium nitride (NbN) SNSPDs have 60% system efficiency, 150 ps timing jitter, <400/s dark counts per detector, and 100 ns recovery time. The operational temperature for the SNSPDs was ∼0.8 K. The typical coincidence count in HOMI measurements was ∼200/s.

We first established the baseline visibility without frequency shifting, which denotes the maximum visibility achievable with our SPDC source. We tuned the center frequency of the signal spectral filter so that the filtered signal and the projected idler were frequency degenerate with overlapping spectra and therefore frequency indistinguishable. We measured the signal-idler coincidences as we varied the relative arrival-time delay between the signal and idler using an adjustable air gap in the signal path, as shown in Fig. 3-3. The HOMI measurement result without frequency shifting is shown in Fig. 3-4(a) (blue markers), fitted with a sinc function (red curve), from which we obtained a 92.6±0.3% background-subtracted interference visibility.

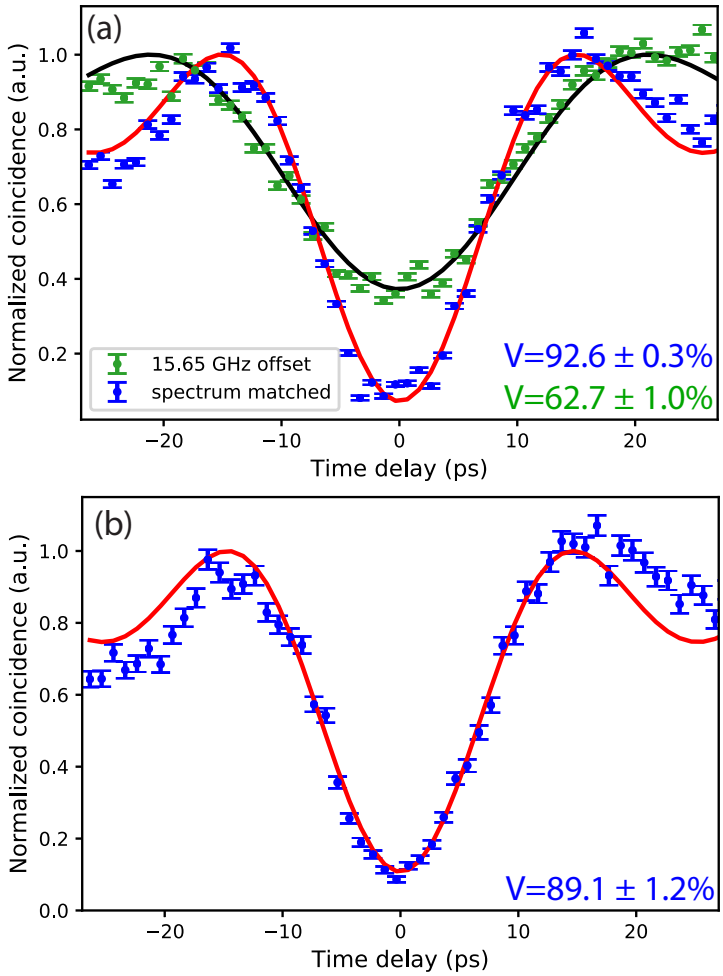

Figure 3-4: Hong-Ou-Mandel interference measurement results. (a) Normalized coincidence counts when the signal and idler had the same center frequency and matched spectra (blue) and when the signal and the blue-shifted idler spectra were offset by 15.65 GHz (green). The fitted functions for the matched and frequency-offset spectra are shown in red and black, respectively. (b) Normalized coincidence counts when the signal frequency was increased by 8 GHz so that it and the blue-shifted idler had nearly identical center frequencies. In both (a) and (b) the error bars mark the ± 1 standard deviations of the detected coincidences' Poisson noise and the maximum coincidence rates of the fitted functions are normalized to one. The background coincidence counts were measured and subtracted for each of the three measurements.

Details of the fitting function and the background subtraction are discussed in Appendix B. The HOMI visibility is defined as $(N_{\max} - N_{\min})/N_{\max}$, where $N_{\max(\min)}$ is the maximum (minimum) detected coincidence count, and the uncertainty is calculated assuming Poisson noise. We calculated the background coincidence counts from accidental coincidences measured when the signal path but not the idler path to the 50/50 beam splitter was blocked, and vice versa. The background coincidence counts were primarily due to polarization leakage of the fiber polarization beam splitter.

We then blue shifted the idler by 15.65 GHz while the signal frequency remained unchanged, so that their center frequencies were now separated by the applied frequency shift. Because the signal and idler spectra were no longer entirely overlapping, the background-subtracted HOMI visibility decreased to 62.7±1.0%, as shown in Fig. 3-4(a) (green markers with black fitted curve, $\Delta\omega/2\pi = 15.65$ GHz). To recover the HOMI visibility, the spectra of the filtered signal and the blue-shifted idler need to have the same center frequencies. We tuned the intensity filter to increase the signal's center frequency by 8 GHz, which is about half of the applied frequency shift of 15.65 GHz. By energy conservation the sum frequency of the SPDC signal and idler equals the cw pump frequency. As a result, the 8 GHz increase in signal frequency reduced the idler frequency by 8 GHz so that their center frequencies became nearly identical. Note that we could not blue shift the signal by the exact 7.825 GHz amount (half of the RF frequency) owing to the programmable intensity filter's minimum frequency-tuning step being too large. However, the 0.35 GHz difference in their center frequencies is relatively small compared with their 50 GHz bandwidth, thus any resultant degradation to HOMI is expected to be small. We remeasured the HOMI visibility, as shown in Fig. 3-4(b) (blue markers with red fitted curve), yielding a measured background-subtracted visibility of 89.1 ± 1.2%, close to the baseline visibility. We can interpret this measurement as starting with initial signal and idler center frequencies being separated by 16 GHz and a corrective frequency shift being applied to recover the frequency indistinguishability that is required for obtaining high HOMI visibility. We should remark that high HOMI visibility requires all degrees of freedom to match well between the two photons, suggesting that

the QPSK-modulator frequency shifter did not materially affect other photonic degrees of freedom in this measurement. We note that the frequency shifter requires a linearly-polarized input with an output of the same polarization.

3.4.1 Role of spectral phase in Hong-Ou-Mandel interference

In this section, we study the effect of the spectral phase on HOMI. Using the setup shown in Fig. 3-3, we can impose an arbitrary spectral phase on one of the photons using the waveshaper. Specifically, we imposed a constant π phase, linear phase, quadratic phase, and randomized phase on the signal photons and measured the HOMI curve for each case. The measurement results are shown in Fig. 3-5.

We first establish a baseline visibility with zero added phase, as shown in Fig. 3-5 (a). In the zero phase case, we measured a fitted visibility of 89.97%, as shown in Fig. 3-5 (b). If only a constant flat phase is present (Fig. 3-5 (c)), we measured visibility of 90.01% (Fig. 3-5 (d)), similar to that with the zero-phase baseline. A linear phase ramp in the spectral-domain (Fig. 3-5 (e)) corresponds to a linear shift in the time domain. As a result, a shifted HOMI pattern was observed, as shown in Fig. 3-5 (f). Next, we studied the effect of quadratic phase, shown in Fig. 3-5 (g) and (h). We observed that the quadratic phase term does not affect the width of the HOMI dip, but it slightly degraded the measured visibility. This observation result is consistent with [103], showing that HOMI is immune to dispersion. We implemented a random phase profile on the signal photons (Fig. 3-5 (i)), and the observed interference pattern shown in Fig. 3-5 (j) departs greatly from the expected sinc shape. The randomized phase distorts the single photon's time-domain shape and degrades the HOMI visibility.

Overall, we show that HOMI is insensitive to the constant and quadratic spectral phase. A linear phase in the spectral domain corresponds to the translation shift of the HOMI pattern in the time domain. Random phase alters the photon's pulse shape and degrades the HOMI visibility. We note that this degradation in HOMI visibility does not indicate that the HOMI is sensitive to spectral phase. This degradation is a result of mismatch between the signal and idler's temporal shape.

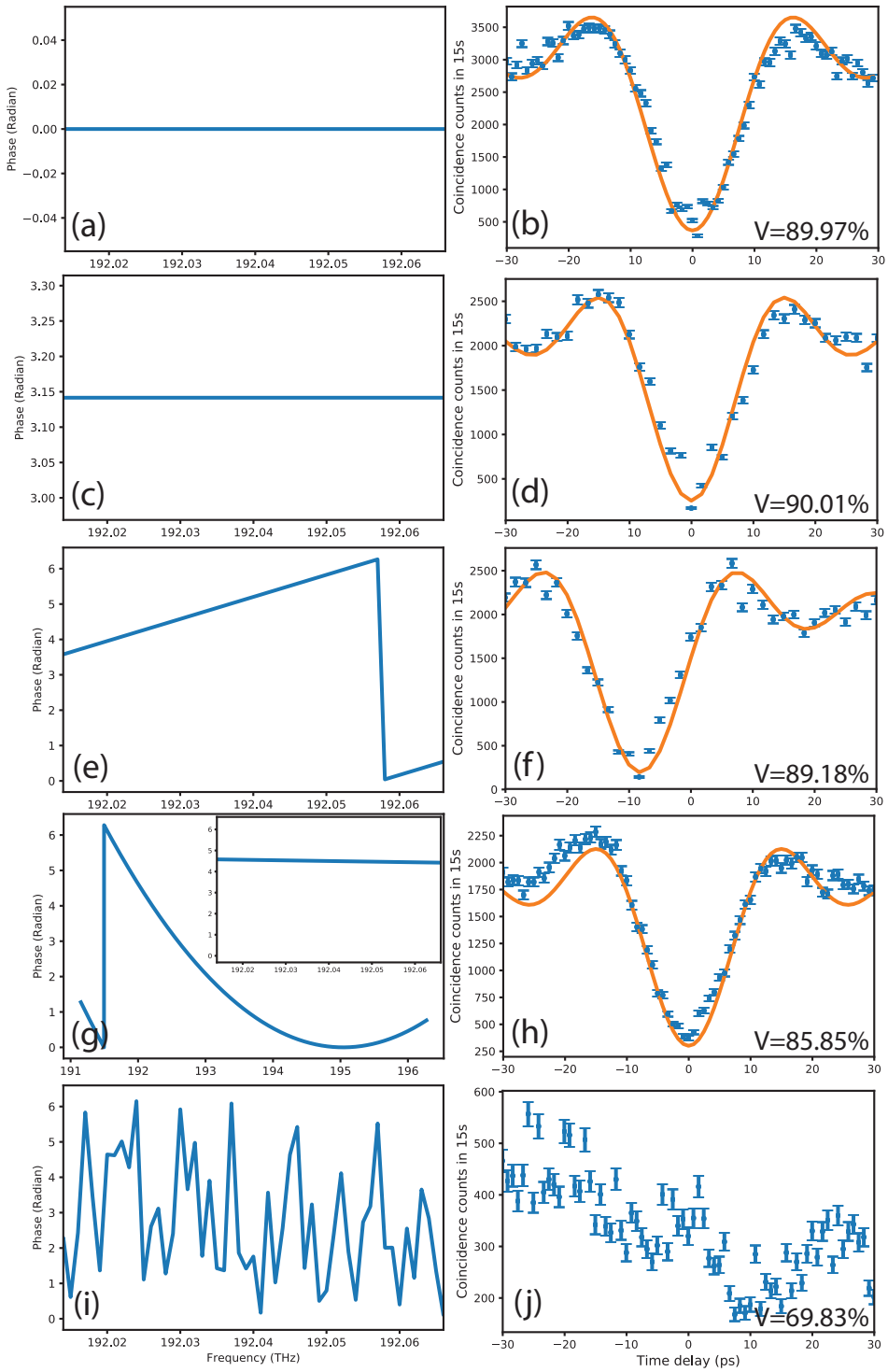

Figure 3-5: HOMI results with different input phase profiles. The shown visibility is fitted with a sinc function except in (j). The reported visibility in (j) is calculated from the measured maximum and minimum coincidence counts.

3.5 Discussion

In this chapter, we showed that we can operate a commercially available QPSK modulator as a frequency shifter. We demonstrated a 15.65 GHz deterministic frequency shift on narrowband and broadband classical light as well as on single photons. We showed the trade-off relation between the amplitude of the shifted signal and the minimum extinction ratio. At a A_m =0.57 drive amplitude, we measured the noise sidebands to be at least 30 dB below the frequency-shifted signal. Furthermore, our measurement suggests that the frequency shift can be applied over a broad spectral range of >1.5 THz while maintaining a 30 dB extinction ratio. The amount of optical frequency shift is set by the applied RF signal frequency and is limited by the bandwidth of the QPSK modulator. Both high bandwidth RF sources and QPSK modulators are commercially available at up to 64 GHz, and they can be used to increase the frequency shift beyond what we have demonstrated. An even higher bandwidth electro-optical phase modulator at 100 GHz has also been reported [104], suggesting future improvements as these devices become commercial. Additionally, we showed that this frequency shifting process only transforms the input photons in the frequency domain while preserving their original state in other degrees of freedom. We believe that QPSK-modulator frequency shifters will be useful in quantum communication and quantum network applications where frequency manipulation is desirable. The waveguide structure of QPSK modulators is compatible with photonic integration processes for more compact device integration with quantum sources and detectors.

Chapter 4

Conjugate-Franson interferometry

Franson interferometry is a well-known quantum measurement technique for probing photon-pair frequency correlations that is often used to certify time-energy entanglement. In this chapter, we demonstrate, for the first time, the complementary technique in the time basis, called conjugate-Franson interferometry, that measures photon-pair arrival-time correlations, thus providing a valuable addition to the quantum toolbox. We obtain a conjugate-Franson interference visibility of $96 \pm 1\%$ without background subtraction for entangled photon pairs generated by spontaneous parametric down-conversion. Our measured result surpasses the quantum-classical threshold by 25 standard deviations and validates the conjugate-Franson interferometer (CFI) as an alternative method for certifying time-energy entanglement. Moreover, the CFI visibility is a function of the biphoton's joint temporal intensity and is therefore sensitive to that state's spectral phase variation, something which is not the case for Franson interferometry or Hong-Ou-Mandel interferometry. We highlight the CFI's utility by measuring its visibilities for two different biphoton states, one without and the other with spectral phase variation, and observing a 21% reduction in the CFI visibility for the latter. The CFI is potentially useful for applications in areas of photonic entanglement, quantum communications, and quantum networking.

Parts of the material presented in this chapter are reproduced from arXiv:2104.15084 (2021) [105].

4.1 Introduction

Time-energy entanglement is the quintessential quantum resource for enabling next-generation quantum technologies such as one-way quantum computation [106], quantum-enhanced sensing [107, 108, 109], and quantum-secured communications [33, 31]. Franson interferometry is a well-known technique for measuring the nonlocal timing coincidence of photon pairs [34]. Because Franson interference visibility resembles the Clauser-Horne-Shimony-Holt (CHSH) inequality, it is often used to characterize the quality of a biphoton's time-energy entanglement [20]. Nevertheless, Franson interferometry only quantifies the photon pair's correlation in the frequency domain and does not provide correlation information in the time domain [35]. Without time-domain characterization, Franson interferometry by itself cannot reveal a full picture of the biphoton's nonclassical correlations. Characterization of entangled photon pairs in the time domain is challenging because there is no readily available experimental method to directly measure two-photon timing correlation. One can extract two-photon time correlation from their joint temporal intensity (JTI) measurements but they typically require sub-picosecond temporal gating and single-photon nonlinear conversion that tend to limit measurement efficiencies [59, 110, 69, 111].

The conjugate-Franson interferometer (CFI) was proposed as a quantum measurement technique for probing two-photon correlation in the time domain in contrast to the Franson interferometer's frequency-domain probing [35]. The two interferometric techniques form a complementary quantum-measurement duo for quantifying biphotons' time-energy entanglement. The Franson interferometer applies a time delay inside one arm of each of its Mach-Zehnder interferometers (MZIs) and measures coincidences to reveal frequency-domain correlations. In comparison, the conjugate-Franson interferometer applies a frequency shift inside one arm of each of its MZIs and measures frequency coincidences utilizing second-order dispersion to reveal time-domain correlations. The time-domain characterization enabled by the CFI can sense spectral phase information and thus improve performance for a wide range of tasks that utilize high-dimensional entangled states, such as quantum communication [35],

quantum sensing [112], and quantum computation [113].

The addition of the CFI to the expanding quantum toolbox offers new or improved measurement capability in quantum photonic studies. Although biphoton spectral phase information can be obtained using frequency-resolved [114] or time-resolved [115] two-photon local interference, these techniques require nearly-degenerate photon pairs. The CFI, however, is a nonlocal two-photon measurement that is suitable for nondegenerate photon pairs. Other means to probe temporal correlations include the use of an electro-optic spectral shearing interferometer [116, 70] with femtosecond pulse gating, and phase-sensitive detection with a stable and well-characterized classical field [117]. The CFI, on the other hand, does not require a reference field and can work with photon pairs generated by pulsed or continuous-wave (cw) pumping.

Recent studies on quantum frequency combs have underscored the inability of Hong-Ou-Mandel interference (HOMI) [57] or Franson interference to distinguish two frequency combs that differ only in their spectral phase content. Lingaraju *et al.* made HOMI measurements on biphoton frequency combs with different spectral phase variations and found identical HOMI signatures [118]. To understand what properties of biphoton frequency combs can be extracted by different interferometric measurements, Chang *et al.* argues that both HOMI and Franson interference are functions of the biphoton's joint spectral intensity (JSI), whereas the CFI measures the state's JTI [119]. Because spectral phase variation does not affect the JSI, it confirms the observation in [118] and suggests that the CFI is the appropriate measurement tool to distinguish combs with spectral phase variations. A classical-optics analog is how linear dispersion of a transform-limited optical pulse imposes a phase chirp that results in pulse broadening which is detectable by time-domain but not frequency-domain measurements.

In this chapter, we report implementing the CFI and obtaining a 96±1% CFI fringe visibility without background subtraction for time-energy entangled photon pairs generated by cw pumped SPDC. Our measured visibility surpasses the quantum-classical threshold by ∼25 standard deviations, thus validating the CFI as a valuable tool for quantifying a biphoton's time-energy entanglement. Moreover, we demonstrate the

CFI's unique capability by utilizing it to distinguish between two biphoton states that differ only in their spectral phase content, one having a uniform phase and the other with a nonuniform phase. Our CFI measurements show a visibility degradation of 21.2% for the biphoton state with a nonuniform spectral phase when compared to the visibility obtained with a uniform phase (which is transform limited), in agreement with our theoretical calculation. The visibility degradation indicates a decrease in timing correlation as the result of the presence of spectral phase, whose information cannot be obtained using standard tools for analyzing the joint properties of photon pairs, such as HOMI, Franson interference, and JSI measurements [118, 46, 120]. We expect that the addition of the CFI to the quantum toolbox provides a simpler way to characterize time-domain correlation and a new method to monitor spectral phase information of time-energy entangled photon pairs. Hence we believe the CFI will enhance future developments of entanglement systems for computing, communication, and sensing applications.

4.2 Conjugate-Franson interferometry

The conjugate-Franson interferometer, shown in Fig. 4-1, comprises two Mach-Zehnder interferometers (MZIs) that are separated in space with each MZI having equal-length arms. For time-energy entanglement characterization, signal (idler) photons of entangled signal-idler photon pairs are sent to one (the other) MZI, and their coincidence outputs are monitored to measure the conjugate-Franson interference. An optical frequency shifter is placed in one of the arms within each interferometer, implementing a $\Delta\Omega$ frequency shift for the signal photons and a $-\Delta\Omega$ frequency shift for the idler photons, with $\Delta\Omega$ large enough to rule out single-photon interference. Light passing through frequency-shifted and the frequency-unshifted paths interfere at a 50/50 beam splitter and acquire a phase difference of ϕ_S (ϕ_I) within the signal (idler) interferometer. The outputs from both MZIs are sent to dispersive elements that impose second-order dispersions with equal magnitudes but opposite signs. The dispersed signal and idler photons are then detected by superconducting nanowire single-photon

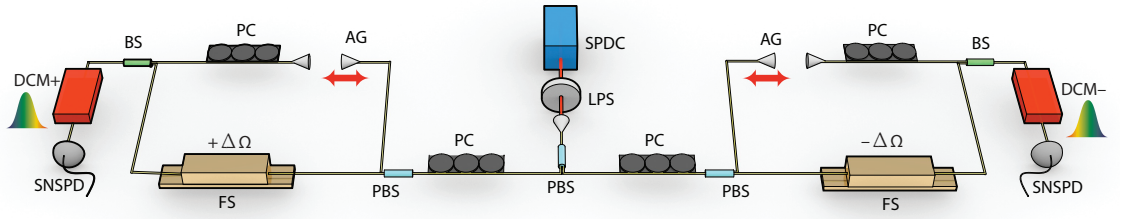

Figure 4-1: Experimental setup of our conjugate-Franson interferometer. Time-energy entangled signal-idler photon pairs generated by cw pumped SPDC were coupled into an optical fiber and routed to their respective MZIs. The signal's frequency shifter was configured to blue shift its input while the idler's shifter was configured to red shift its input. The polarization and the path lengths between the two arms of each MZI were made to be the same. The fiber-based CFI was placed inside a custom-built two-stage thermal box for phase stabilization. The MZI outputs were detected with SNSPDs and their arrival times recorded for coincidence measurements. LPS: long-pass filter; PBS: polarizing beam splitter; PC: polarization controller; FS: frequency shifter for $\Delta\Omega$ ($-\Delta\Omega$) frequency shift; AG: tunable air gap; BS: 50/50 beam splitter; DCM+(−): dispersion module with normal (anomalous) dispersion.

detectors (SNSPDs) and their timing coincidences are recorded. The second-order dispersions imposed by the dispersive elements correlates the frequency content of the inputs to their measured arrival times, thus effectively converting the performed time-domain measurement result to a frequency-domain measurement. The opposite signs of the two dispersive elements, together with nonlocal dispersion cancellation [31, 121], recover the signal-idler frequency coincidences as signal-idler timing coincidences and thus distinguish between different signal-idler sum frequencies.

4.2.1 Mathematical description of conjugate-Franson interferometry

We are interested in single spatial mode signal and idler fields produced by a type-II or type-0 phase matched spontaneous parametric downconverter. The scalar, photon-units, positive-frequency field operators for the relevant polarizations of the signal and idler will be taken to be $\hat{E}_S^{(+)}(t)$ and $\hat{E}_I^{(+)}(t)$ with the usual δ-function commutators,

$$[\hat{E}_K^{(+)}(t), \hat{E}_K^{(+)\dagger}(u)] = \delta(t-u), \text{ for } K = S, I. \tag{4.1}$$

For what will follow it will be valuable to have these operators' frequency-domain decompositions,

$$\hat{E}_S^{(+)}(t) = \int \frac{\mathrm{d}\omega_S}{2\pi}\, \hat{\mathcal{E}}_S(\omega_S) e^{-i(\omega_{S_0}+\omega_S)t} \quad \text{and} \quad \hat{E}_I^{(+)}(t) = \int \frac{\mathrm{d}\omega_I}{2\pi}\, \hat{\mathcal{E}}_I(\omega_I) e^{-i(\omega_{I_0}-\omega_I)t}, \quad (4.2)$$

where ω_{S_0} (ω_{I_0}) is the center frequency of the signal (idler). The convention we have chosen here accords opposite signs to the signal and idler detunings such that their sum, for a biphoton produced by SPDC, is confined to a phase-matching bandwidth about zero frequency. Throughout this section integrals without limits will be taken to be from $-\infty$ to ∞.

Our interest will be in biphoton states of these signal and idler, i.e., states of the form

$$|\psi\rangle_{SI} = \frac{1}{2\pi} \int \mathrm{d}\omega_S \int \mathrm{d}\omega_I\, \Psi_{SI}(\omega_S, \omega_I) |\omega_{S_0} + \omega_S\rangle_S |\omega_{I_0} - \omega_I\rangle_I \,. \quad (4.3)$$

Here, $|\omega_{S_0} + \omega_S\rangle_S$ and $|\omega_{I_0} - \omega_I\rangle_I$ are signal and idler states consisting of single photons at detunings ω_S and $-\omega_I$, respectively, from those fields' center frequencies. The preceding states are properly normalized, viz., ${}_{SI}\langle\psi|\psi\rangle_{SI} = 1$. Hence, taking

$${}_S\langle\omega_{S_0} + \omega_S|\omega_{S_0} + \omega_S'\rangle_S = 2\pi\, \delta(\omega_S - \omega_S') \quad \text{and} \quad {}_I\langle\omega_{I_0} - \omega_I|\omega_{I_0} - \omega_I'\rangle_I = 2\pi\, \delta(\omega_I - \omega_I'), \quad (4.4)$$

we find that $\int \mathrm{d}\omega_S \int \mathrm{d}\omega_I\, |\Psi_{SI}(\omega_S, \omega_I)|^2 = 1$. In other words, this biphoton's JSA is

$$\mathrm{JSA}(\omega_S, \omega_I) = \Psi_{SI}(\omega_S, \omega_I), \quad (4.5)$$

and its JSI is

$$\mathrm{JSI}(\omega_S, \omega_I) = |\Psi_{SI}(\omega_S, \omega_I)|^2. \quad (4.6)$$

For a time-domain representation of this biphoton, we introduce signal and idler states $|t_S\rangle_S$ and $|t_I\rangle_I$ consisting of single photons at times t_S and t_I, respectively.

These states are the Fourier duals of $|\omega_{S_0}+\omega_S\rangle_S$ and $|\omega_{I_0}-\omega_I\rangle_I$, i.e., we have

$$|t_S\rangle_S = \int \frac{\mathrm{d}\omega_S}{2\pi}\, e^{i(\omega_{S_0}+\omega_S)t_S}|\omega_{S_0}+\omega_S\rangle_S \quad \text{and} \quad |t_I\rangle_I = \int \frac{\mathrm{d}\omega_I}{2\pi}\, e^{i(\omega_{I_0}-\omega_I)t_I}|\omega_{I_0}-\omega_I\rangle_I, \tag{4.7}$$

and

$$|\omega_S\rangle_S = \int \mathrm{d}t_S\, e^{-i(\omega_{S_0}+\omega_S)t_S}|t_S\rangle_S \quad \text{and} \quad |\omega_I\rangle_I = \int \mathrm{d}t_I\, e^{-i(\omega_{I_0}-\omega_I)t_I}|t_I\rangle_I, \tag{4.8}$$

from which we get

$${}_K\langle t_K|t'_K\rangle_K = \delta(t_K - t'_K), \text{ for } K = S, I. \tag{4.9}$$

Then, direct evaluation using Eqs. (4.3), (4.4), and (4.7) gives

$${}_S\langle t_S|_I\langle t_I|\psi\rangle_{SI} = \frac{e^{-i(\omega_{S_0}t_S+\omega_{I_0}t_I)}}{2\pi}\int \mathrm{d}\omega_S \int \mathrm{d}\omega_I\, \Psi_{SI}(\omega_S,\omega_I)e^{-i(\omega_S t_S-\omega_I t_I)}, \tag{4.10}$$

which implies that

$$|\psi\rangle_{SI} = \int \mathrm{d}t_S \int \mathrm{d}t_I\, \psi_{SI}(t_S,t_I)|t_S\rangle_S|t_I\rangle_I, \tag{4.11}$$

with

$$\psi_{SI}(t_S,t_I) = \frac{e^{-i(\omega_{S_0}t_S+\omega_{I_0}t_I)}}{2\pi}\int \mathrm{d}\omega_S \int \mathrm{d}\omega_I\, \Psi_{SI}(\omega_S,\omega_I)e^{-i(\omega_S t_S-\omega_I t_I)} \tag{4.12}$$

satisfying $\int \mathrm{d}t_S \int \mathrm{d}t_I |\psi_{SI}(t_S,t_I)|^2 = 1$. It is now easily seen that the biphoton's JTA and JTI are

$$\mathrm{JTA}(t_S,t_I) = \psi_{SI}(t_S,t_I), \tag{4.13}$$

and

$$\mathrm{JTI}(t_S,t_I) = |\psi_{SI}(t_S,t_I)|^2. \tag{4.14}$$

Later we shall employ the Gaussian biphoton wave functions,

$$\Psi_{SI}(\omega_S, \omega_I) = \frac{e^{-(\omega_S-\omega_I)^2\sigma_{\rm coh}^2}\, e^{-(\omega_S+\omega_I)^2\sigma_{\rm cor}^2/4}}{\sqrt{\pi/2\sigma_{\rm coh}\sigma_{\rm cor}}}, \tag{4.15}$$

and

$$\psi_{SI}(t_S, t_I) = \frac{e^{-i(\omega_{S_0}t_S+\omega_{I_0}t_I)}\, e^{-(t_S+t_I)^2/16\sigma_{\rm coh}^2}\, e^{-(t_S-t_I)^2/4\sigma_{\rm cor}^2}}{\sqrt{2\pi\sigma_{\rm coh}\sigma_{\rm cor}}}, \tag{4.16}$$

where the root-mean-square (rms) coherence time, $\sigma_{\rm coh}$, is determined by the downconverter's pump linewidth and the rms correlation time, $\sigma_{\rm cor}$, is determined by the downconverter's phase-matching bandwidth. This biphoton can be realized by engineered phase matching of a periodically-poled nonlinear crystal, see, e.g., [48].

There is a detailed derivation of the CFI's coincidence-count behavior in [35]'s Supplemental Material. Thus we can content ourselves with a briefer presentation that gets at an essential feature of the CFI that was not made explicit in Ref. [35], i.e., the CFI's coincidence behavior is controlled by the biphoton state's joint temporal intensity (JTI). As such, the CFI complements the conventional Franson interferometer (FI), whose coincidence behavior is controlled by the biphoton state's joint spectral intensity (JSI). The biphoton's JSI is the squared magnitude of its joint spectral amplitude (JSA), which is the biphoton's properly normalized frequency-domain wave function. Similarly, the biphoton's JTI is the squared magnitude of its joint temporal amplitude (JTA), which is the biphoton's properly normalized time-domain wave function. It follows that knowing both the JSI and the JTI will allow the biphoton's full state to be determined by applying standard phase-retrieval techniques to recover the JSA's missing spectral phase, see, e.g., [122].

To instantiate the CFI configuration shown in Fig. 4-1, let the downconverter's signal beam undergo the $\Delta\Omega > 0$ frequency shift and normal dispersion, while the downconverter's idler beam undergoes the $-\Delta\Omega < 0$ frequency shift and anomalous dispersion. Taking all the optics to be lossless, we then have that the positive-frequency field operators illuminating the single-photon detectors in Fig. 1 are

$$\hat{E}_{S'}^{(+)}(t) = \frac{1}{2}\int \frac{{\rm d}\omega_S}{2\pi}\, [\hat{\mathcal{E}}_S(\omega_S) + \hat{\mathcal{E}}_S(\omega_S + \Delta\Omega)e^{i\phi_S}]e^{i\beta_2\omega_S^2/2}e^{-i(\omega_{S_0}+\omega_S)t} \tag{4.17}$$

and

$$\hat{E}_{I'}^{(+)}(t) = \frac{1}{2}\int \frac{\mathrm{d}\omega_I}{2\pi}\,[\hat{\mathcal{E}}_I(\omega_I) + \hat{\mathcal{E}}_I(\omega_I + \Delta\Omega)e^{i\phi_I}]e^{-i\beta_2\omega_I^2/2}e^{-i(\omega_{I_0}-\omega_I)t}. \tag{4.18}$$

As shown in Ref. [35], for sufficiently high frequency shifts and a sufficiently high dispersion coefficient, β_2, there will not be any second-order interference and, in the absence of dark counts, the probability of registering a coincidence from a biphoton emitted by the downconverter is

$$P_{\mathrm{CFI}}(\phi_S,\phi_I) = \frac{\eta^2}{8}\left(1 + \int \mathrm{d}\omega_S \int \mathrm{d}\omega_I\, \mathrm{Re}[\Psi_{SI}^*(\omega_S,\omega_I)\Psi_{SI}(\omega_S+\Delta\Omega,\omega_I+\Delta\Omega)e^{i(\phi_S+\phi_I)}]\right), \tag{4.19}$$

where η is the detectors' quantum efficiency.

To rewrite Eq. (4.19) in terms of $\psi_{SI}(t_S,t_I)$, we first invert Eq. (4.12) to obtain

$$\Psi_{SI}(\omega_S,\omega_I) = \frac{1}{2\pi}\int \mathrm{d}t_S \int \mathrm{d}t_I\, \psi_{SI}(t_S,t_I)e^{i[(\omega_{S_0}+\omega_S)t_S+(\omega_{I_0}-\omega_I)t_I]}. \tag{4.20}$$

Using this result in Eq. (4.19) gives us the result we are seeking,

$$P_{\mathrm{CFI}}(\phi_S,\phi_I) = \frac{\eta^2}{8}\left(1 + \int \mathrm{d}t_S \int \mathrm{d}t_I\, |\psi_{SI}(t_S,t_I)|^2 \cos[\Delta\Omega(t_S-t_I) + (\phi_S+\phi_I)]\right) \tag{4.21}$$

$$= \frac{\eta^2}{8}\left(1 + \int \mathrm{d}t_S \int \mathrm{d}t_I\, \mathrm{JTI}(t_S,t_I)\cos[\Delta\Omega(t_S-t_I)+\phi_T]\right), \tag{4.22}$$

where $\phi_T \equiv \phi_S + \phi_I$ is the interferometer's phase sum. As an illustration of the coincidence probability's behavior, let us evaluate Eq. (4.22) using $\psi(t_S,t_I)$ from Eq. (4.16). The double integral is easily performed if we change to sum and difference coordinates, i.e., $t_+ \equiv (t_S+t_I)/2$ and $t_- \equiv t_S - t_I$. The result we obtain is

$$P_{\mathrm{CFI}}(\phi_T) = \frac{\eta^2[1 + e^{-\Delta\Omega^2\sigma_{\mathrm{cor}}^2/2}\cos(\phi_T)]}{8}, \tag{4.23}$$

which implies an interference fringe visibility

$$V_{\mathrm{CFI}} \equiv \frac{\max_{\phi_T}[P_{\mathrm{CFI}}(\phi_T)] - \min_{\phi_T}[P_{\mathrm{CFI}}(\phi_T)]}{\max_{\phi_T}[P_{\mathrm{CFI}}(\phi_T)] + \min_{\phi_T}[P_{\mathrm{CFI}}(\phi_T)]} = e^{-\Delta\Omega^2\sigma_{\mathrm{cor}}^2/2} \approx 1, \text{ for } \Delta\Omega \ll 1/\sigma_{\mathrm{cor}}. \tag{4.24}$$

The preceding analysis must be modified to treat the case of ideal continuous-wave (cw) pumped downconversion. The biphoton such an arrangement generates is a state

$$|\psi\rangle_{SI} \propto \int \mathrm{d}\omega\, \Psi_{SI}(\omega)|\omega_{S_0} + \omega\rangle_S|\omega_{I_0} - \omega\rangle_I \tag{4.25}$$

that cannot be normalized, i.e., ${}_{SI}\langle\psi|\psi\rangle_{SI} = \infty$. Nevertheless, we can normalize $\Psi_{SI}(\omega)$ to serve as this biphoton's JSA for $\omega_S = -\omega_I = \omega$ and $|\Psi_{SI}(\omega)|^2$ as its JSI for $\omega_S = -\omega_I = \omega$. Furthermore, by neglecting the unimportant—insofar as $P_{\mathrm{CFI}}(\phi_T)$ is concerned—phase factor $e^{-i(\omega_{S_0}t_S + \omega_{I_0}t_I)}$, we can define

$$\psi_{SI}(t_-) = \frac{1}{\sqrt{2\pi}} \int \mathrm{d}\omega\, \Psi_{SI}(\omega) e^{-i\omega t_-}, \tag{4.26}$$

so that the unnormalizable $|\psi\rangle_{SI}$ can be rewritten as

$$|\psi\rangle_{SI} \propto \int \mathrm{d}t_-\, \psi_{SI}(t_-)|t_+ + t_-/2\rangle_S|t_+ - t_-/2\rangle_I, \tag{4.27}$$

where, as before, $t_+ = (t_S + t_I)/2$ and $t_- = (t_S - t_I)$. The JTI for this cw case is then $\mathrm{JTI}(t_-) = |\psi_{SI}(t_-)|^2$ and the CFI's coincidence probability is

$$P_{\mathrm{CFI}}(\phi_T) = \frac{\eta^2}{8}\left(1 + \int \mathrm{d}t_-\, \mathrm{JTI}(t_-)\cos(\Delta\Omega t_- + \phi_T)\right). \tag{4.28}$$

The resulting visibility is

$$V_{\mathrm{CFI}} = \int \mathrm{d}t_-\, \mathrm{JTI}(t_-)\cos(\Delta\Omega t_-). \tag{4.29}$$

Here, we see that conjugate-Franson interference visibility is a function of the JTI, which is susceptible to the spectral phase. For long-distance nonlocal interference, the visibility is affected by the second-order dispersion in fiber during propagation.

This is different from Franson interference, which is unaffected by the fiber dispersion en route. As a result, conducting conjugate-Franson interference measurement at long distance requires dispersion compensation to achieve high-visibility nonlocal interference.

4.2.2 Experimental setup

To demonstrate conjugate-Franson interferometry, we built a CFI as shown in the experimental schematic of Fig. 4-1 with inputs of time-energy entangled photon pairs generated from SPDC in a type-II phase-matched periodically-poled potassium titanyl phosphate (PPKTP) waveguide pumped by a 780 nm cw laser. The orthogonally-polarized signal and idler photons were nondegenerate with ∼200 GHz offset between their center frequencies and each had a full-width at half-maximum (FWHM) bandwidth of 320 GHz. The photon pairs were separated using a fiber polarizing beam splitter and sent to their respective MZIs. We repurposed two dual-drive quadrature phase-shift keying (QPSK) modulators (Fujitsu FTM7961EX) operating in a configuration for single sideband generation as the frequency shifters, as discussed in Chapter 3, and set the frequency shift at $\pm\Delta\Omega/2\pi = \pm 15.65$ GHz [80]. We first characterized the frequency-shifted outputs from both frequency shifters using a narrowband cw laser at 1560 nm, as shown in Fig. 4-2(a). Within the desired frequency range from $-\Delta\Omega$ to $\Delta\Omega$, a minimum of 25 dB carrier-to-sideband ratio was achieved for both blue and red frequency shifters. During operation, the signal's MZI had an 18.6 dB insertion loss and the idler's MZI had a 22.7 dB insertion loss. These high insertion losses were mainly due to the low conversion efficiencies of the frequency shifters [80]. The different insertion losses of the two MZIs was caused by performance difference of the two frequency shifters and tunable air gaps. The outputs from the signal and idler MZIs were sent to fiber Bragg-grating dispersion modules that imposed equal magnitude but opposite sign dispersions of ±10 ns/nm. These dispersion modules had 3 dB insertion loss and passband from 1557.85 nm (192.44 THz) to 1563.05 nm (191.80 THz). The photons emerging from the dispersion modules were detected using WSi SNSPDs with ∼80% system efficiency and 120 ps timing jitter. The detected

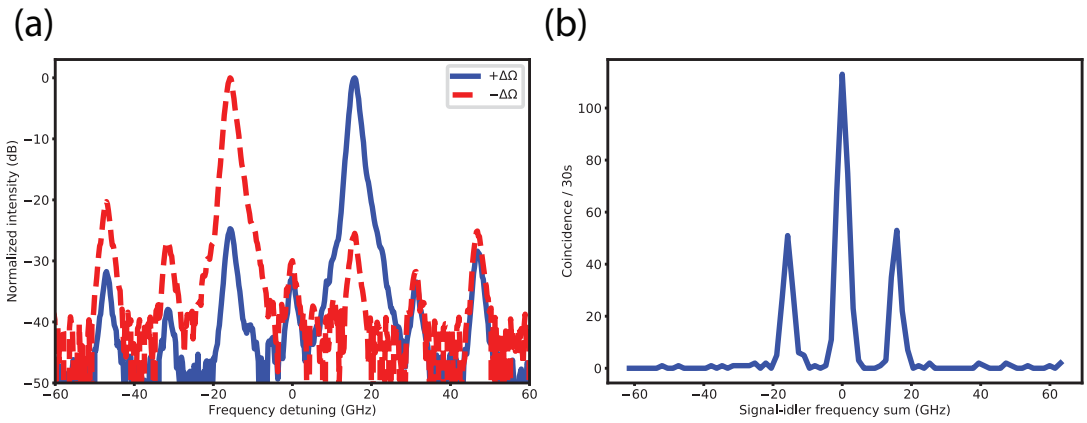

Figure 4-2: (a) Log-scale display of the frequency shifters' output spectra, measured using classical light, that show signal-to-noise ratios of at least 20 dB limited by higher-order sidebands. Maximum intensities of both spectra normalized to 0 dB. (b) Measured CFI coincidences vs. the inferred signal-idler frequency sum: central peak location determines zero detuning of the signal-idler sum frequency. 30-s integration time for each data point; measurement taken with MZI phase sum $\phi_T \approx \pi/2$.

signal and idler spectral ranges were limited by the dispersion modules' 640 GHz passband. The detection events were time-tagged using a time-tagger (Hydraharp 400) with 128 ps timing resolution.

Because the SPDC signal-idler photon pairs are time-energy entangled, the imposed opposite dispersions cancel and their arrival times remain correlated [31]. Nevertheless, the existence of dispersion reveals the incoming photons' frequency information. The resolution of our frequency-domain measurement is 1.8 GHz, which is determined by the detectors' timing jitter and the amount of applied dispersion. A sample signal-idler coincidence measurement from the CFI is shown in Fig. 4-2(b). The locations of the coincidence peaks correspond to the signal-idler sum frequencies which in turn indicate the possible paths the signal and idler photon have traveled. There are four possible path configurations as signal and idler photons can travel along either the frequency-shifted or the frequency-unshifted arms. The two side peaks correspond to the case in which only one of the signal and idler photons has been frequency shifted such that the signal-idler frequency sum is detuned by $\pm\Delta\Omega/2\pi = \pm 15.65$ GHz. For the center peak the sum frequency remains unchanged, requiring that both photons travel along their frequency-unshifted arms or they both

go through their respective frequency shifters. The two different paths are indistinguishable and they interfere as a function of the MZI phase sum ϕ_T, producing the CFI's nonlocal coincidence interference similar to that of the Franson interferometer. We note that if the dispersion modules were not present, the three peaks could not be separated and the maximum interference visibility achievable would be limited to 50%.

4.2.3 Interferometer alignment procedure

Alignment of the conjugate-Franson interferometer is critical for achieving high interference visibility. This section will discuss the procedure for matching the path length and setting the correct polarization.

High interference visibility requires the frequency-shifted path and frequency-unshifted path within each MZI to have the same polarization. In our experimental setup shown in Fig. 4-1, the polarization beam splitter (PBS) set the initial polarization state for the frequency-shifted and frequency-unshifted paths. After the PBS, both paths' polarization are aligned to the slow axis of the PBS's polarization-maintaining (PM) fiber. The input and the output fibers of the frequency shifter are also PM, maintaining the initial polarization state. In the frequency-unshifted path, the fiber is not polarization-maintaining. We use a polarization paddle to adjust the polarization in the frequency-unshifted path to match the polarization of the frequency-shifted path.

To do so, we first connected the output of the MZI to a polarization paddle followed by a linear fiber polarizer. We sent laser light through the input PBS of the MZI and varied the laser polarization so that the laser light was equally distributed between the frequency-shifted and frequency-unshifted paths. We then blocked the transmission of the frequency-unshifted path. The power after the linear polarizer was monitored and maximized by changing the input polarization to the linear polarizer. In this step, we aligned the polarization of the frequency-shifted path to the linear polarizer. Next, we unblocked the frequency-unshifted path but blocked the frequency-shifted path. We adjusted the polarization on the frequency-unshifted path using the in-line

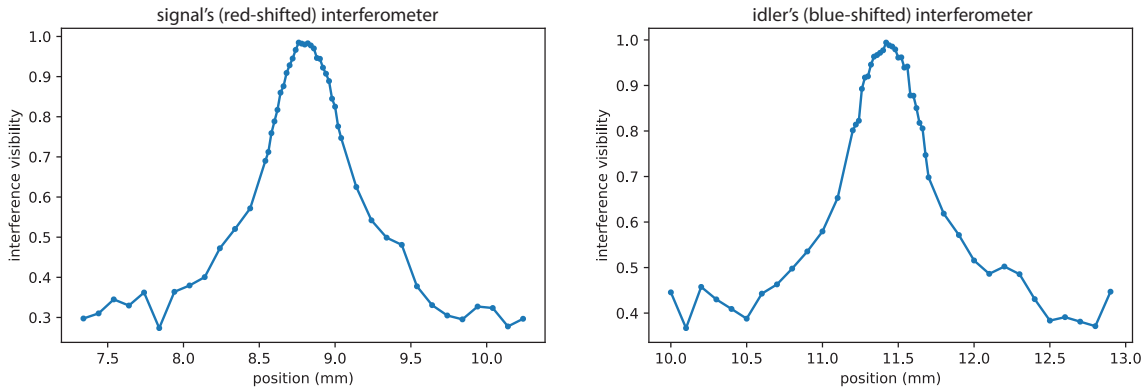

Figure 4-3: Single photon interference visibility as a function of air gap position. The optimal location for the signal's (red-shifted) interferometer is 8.82 mm. The optimal location for the idler's (blue-shifted) interferometer is 11.42 mm.

polarization paddles so that output power from the linear polarizer was maximized. The polarization of both paths should be matched at this point. Alternatively, one can use a polarimeter to observe the polarization and match the polarization of the two paths.

We used an interferometric method to determine the path-length mismatch between the frequency-shifted and frequency-unshifted paths. We filtered the broadband SPDC photon pairs' spectra generated from a type-0 phase-matched periodically-poled lithium niobate (PPLN) crystal using a 10 nm flat-top filter centered at 1560 nm. The filtered photons' polarizations were set such that the input PBS to the MZI functioned as a 50/50 beam splitter. We set the QPSK modulator to pass its input without applying a frequency shift. Finally, we observed the single-photon interference by monitoring the photon count rate from the MZI output. The interference's visibility indicates the two paths' length mismatch. We used the tunable air gap to look for the optimal position where the visibility is maximized, showing that the frequency-shifted path and the frequency-unshifted path have the same lengths. The measurement results are shown in Fig. 4-3. We adjusted the air gap position to achieve $\geq$ 99% interference visibility for the signal (red-shifted) MZI and the idler (blue-shifted) MZI shown in Fig. 4-1. We note that the optimal location is sensitive to the ambient room temperature and needs to be optimized regularly. One can also

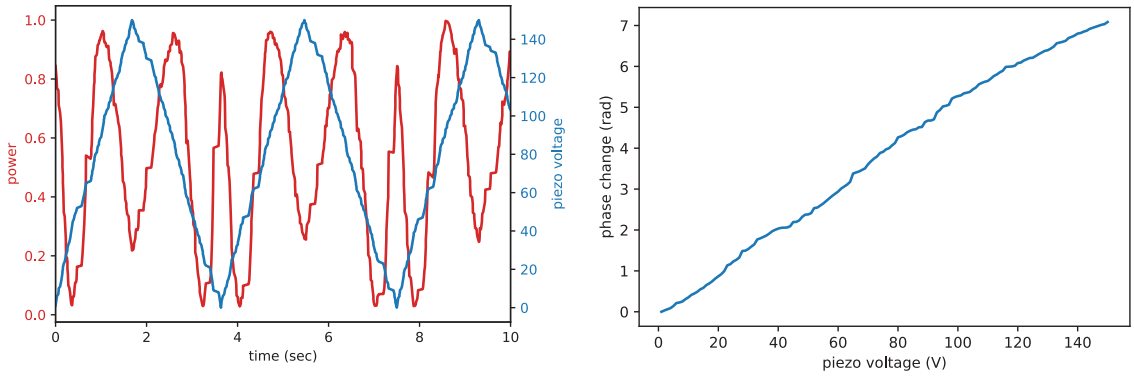

Figure 4-4: Left: applied voltage to PZT and the measured MZI power as a function of time. Right: Calculated induced phase change as a function of the applied voltage to PZT.

use a broadband ASE light to conduct the path-length matching calibration instead of using broadband single photons.

4.2.4 Piezoelectric transducer characterization

We used a piezoelectric transducer (PZT) stack to impose a controllable phase change actively. We fixed the fiber onto the PZT stack. The fiber is stretched as the PZT stack expands. The PZT was placed in the signal's MZI (blue-shifted MZI) to change its phase, while the idler's MZI (red-shifted MZI) was kept unchanged. The PZT has input voltage ranges from 0 to 150 V. To characterize the performance of the PZT, we monitored the MZI output power with a 1560 nm laser input. The MZI power output changes as a function of the relative phase difference introduced by the PZT. We varied the PZT voltage and recorded the corresponding applied voltage (V) and the measured MZI power output. The results are shown in the left plot of Fig. 4-4. We see that the PZT has a response time in the ms time scale, and the induced phase change is repeatable and greater than 2π. We calculated the induced phase change based on MZI's optical response and plotted the results in the right plot of Fig. 4-4. The relationship between the voltage applied to the PZT and the induced phase change is mostly linear. The V_π of this PZT fiber stretcher is found to be ~ 64 V.

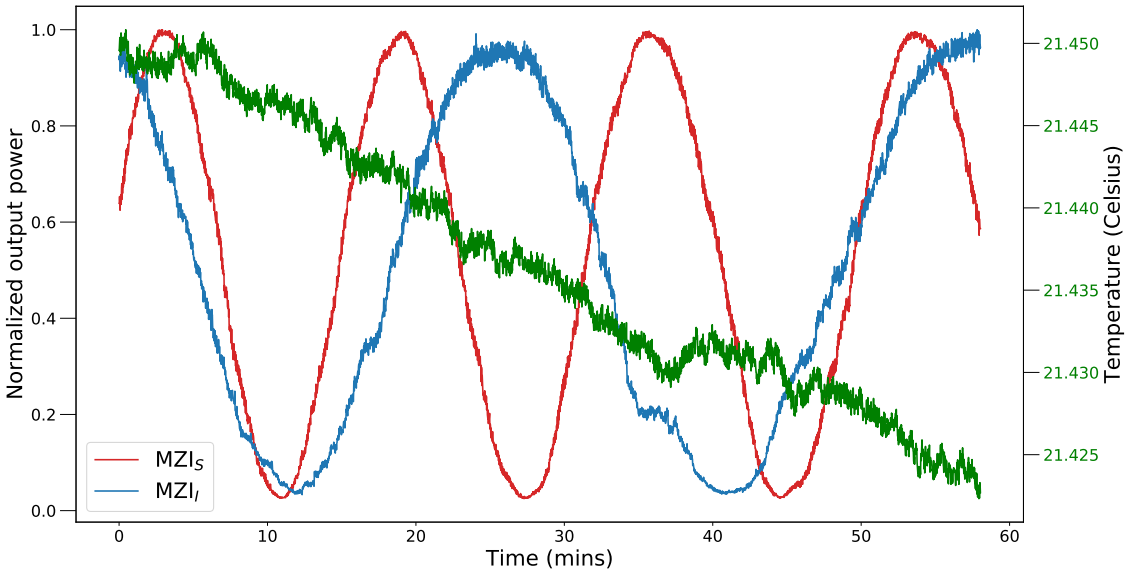

Figure 4-5: Normalized output power from MZIs measured at 1s intervals. The red (blue) curve is the measured power for signal's (idler's) MZI. The green curve is the measured ambient temperature inside CFI's thermal enclosure.

4.2.5 Conjugate-Franson interferometer phase stability characterization

We placed the CFI setup in a custom-built two-stage thermal enclosure. Both the outer and inner layers were made from cardboard and thermal-isolation foam. This passive thermal enclosure reduced and slowed down the ambient thermal fluctuations and also restricted the inside air current flow so that the phase of the fiber interferometer was relatively stable for the duration of measurements. During measurement, the temperature outside the enclosure was kept reasonably stable.

To study the phase drift we simultaneously monitored the power variations in the signal and idler's balanced Mach-Zehnder interferometers (MZIs) with a 1560 nm cw laser. Frequency shift was not employed in this phase-drift measurement. The results we obtained are shown in Fig. 4-5. From the MZIs' output powers, we found that the two MZIs' phases drift at different rates. The relative phase of the signal MZI changes at a rate of 0.37 rad/min. The relative phase of the idler MZI changes at a rate of 0.27 rad/min. The temperature inside the box changes at a rate of 0.0004°C/min.

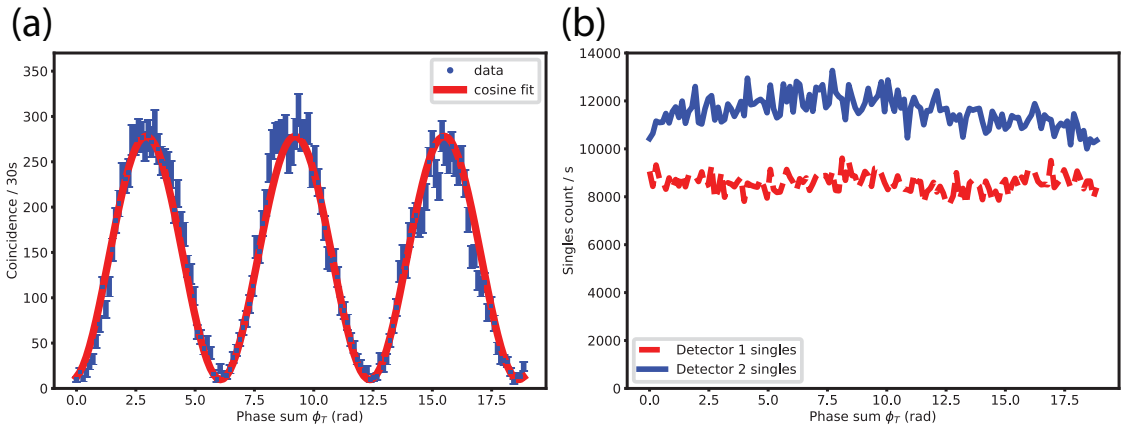

Figure 4-6: (a) Coincidences (blue) as a function of MZI phase sum ϕ_T, with calculated uncertainties assuming Poisson statistics. Least-squares fit (solid red line) to the form $A[1 + V\cos(\phi_T)]$ yields a fitted CFI visibility (V) of 93%. No background counts are subtracted from measured data. (b) Singles count rates for both detectors as functions of the MZI phase sum ϕ_T, showing no meaningful variations.

4.2.6 Conjugate-Franson interference results

We observed that the center coincidence peak of Fig. 4-2(b) varied as a function of the phase sum ϕ_T. The CFI was thermally insulated but we still observed that the center coincidence peak changed its magnitude due to residual thermal drift at an estimated rate of 0.29±0.06 rad/min for ϕ_T. This number is calculated from the measured 21.6±0.4 minutes it took the interferometer to accumulate a 2π phase change. We recorded the signal-idler coincidences and plotted the coincidence counts of the center peak as a function of the accumulated phase sum ϕ_T, as shown in Fig. 4-6(a). The result shows a clear oscillatory signature as a function of the phase drift. To eliminate the possibility that the change of the coincidence counts was caused by changes of the photon flux, we also recorded the singles rates of both detectors at the same time during the coincidence measurement, as shown in Fig. 4-6(b). The measured singles rates remain constant throughout the thermal drift duration and show that the oscillatory fringe is not a result of single-photon interference.

To obtain an accurate value for the CFI's interference visibility, we attached a PZT stack to the signal MZI's frequency-unshifted arm as a fiber stretcher to impose a controllable phase shift on ϕ_S. The PZT has an input voltage range between

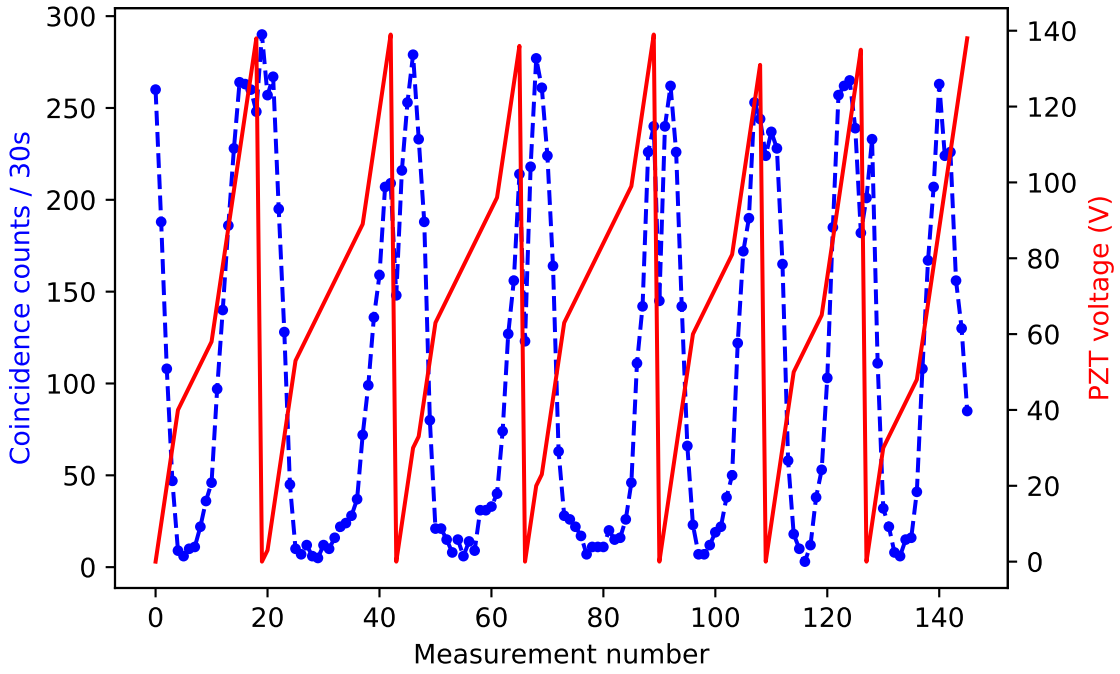

Figure 4-7: CFI coincidences with controllable phase shift. The abscissa is the number of sequential measurements. The coincidences are shown by the blue dashed line with the left ordinate. The PZT voltage associated with each measurement is shown in red with the right ordinate. The calculated visibilities for these seven measurements are: 0.961, 0.956, 0.966, 0.958, 0.951, 0.948, 0.978.

0 to 150 V and is capable of applying phase shifts $> 2\pi$. We used this PZT to actively search for the maximum and minimum coincidence counts of the conjugate-Franson interference by repeatedly scanned ϕ_S from 0 to 2π while keeping ϕ_I constant. The fringe visibility was calculated based on the observed minimum and maximum coincidence counts within each phase scan. For each search, we increased the PZT voltage from 0 to 140 V at variable step sizes. When the coincidence counts are within 10% of the maximum or minimum value, we set the voltage step size to be 3 V. Otherwise, we set the voltage step size to be 12 V. We show seven search results in Fig. 4-7 as an example. The PZT voltage is always changed in the ascending direction to avoid hysteresis. Once the input voltage setting exceeds 140 V, the voltage is reset to 0 V. The reset points show up as the sudden increase or decrease of the CFI coincidence, which are visible in Fig. 4-7.

We obtain a CFI visibility of $96 \pm 1\%$ based on 23 phase-scan measurements and an uncertainty of 1 standard deviation. We estimate that degradation of our CFI visibility measurements was due to phase fluctuations of the CFI (1.2%), modulators' extra sidebands (0.7%), modulator dispersion (0.5%), dark counts and noise background (0.5%), and SPDC multi-pair events (0.4%). The achieved visibility validates the quantum nonlocal correlation between our SPDC photon pairs, surpassing the quantum-classical threshold of $1/\sqrt{2}$ =70.7% by ∼25 standard deviations. This high CFI visibility confirms that our photon-pair source indeed produces time-energy entanglement and validates conjugate-Franson interferometry's being a promising quantum measurement technique for certifying time-energy entanglement. We note that although our current measurement setup is affected by the post-selection loophole, it can be modified to match the two side peaks temporally and eliminate the post-selection loophole [123].

4.3 Spectral phase detection using conjugate-Franson interference

To show that the CFI brings new capability to the increasingly expanding photonic quantum toolbox, we demonstrate that the CFI visibility is sensitive to the spectral phase of a biphoton state, something which cannot be sensed by Franson or Hong-Ou-Mandel interferometers. First consider a cw pumped SPDC source generating a time-energy entangled biphoton state with a flat spectrum spanning 320 GHz and no spectral phase variation, i.e., its frequency-domain description is

$$|\psi^{(1)}\rangle_{SI} \propto \int_{-\omega_{\max}}^{\omega_{\max}} \mathrm{d}\omega \, \Psi_{SI}^{(1)}(\omega) |\omega_{S_0} + \omega\rangle_S |\omega_{I_0} - \omega\rangle_I \,, \tag{4.30}$$

where $\Psi_{SI}^{(1)}(\omega) = 1/\sqrt{2\omega_{\max}}$ is its joint spectral amplitude (JSA), ω_{S_0} (ω_{I_0}) is the signal (idler) center frequency, and ω is the state's frequency detuning with a range

of $\pm\omega_{\max}$ where $\omega_{\max}/2\pi = 160\,\mathrm{GHz}$. Now consider the state $|\psi^{(2)}\rangle_{SI}$ whose JSA is

$$\Psi^{(2)}_{SI}(\omega) = \begin{cases} 1/\sqrt{2\omega_{\max}}, & \text{for } |\omega| \le \omega_1 \\ e^{i\phi}/\sqrt{2\omega_{\max}}, & \text{for } \omega_1 < |\omega| \le \omega_{\max}, \end{cases} \tag{4.31}$$

where $\omega_1/2\pi = 80\,\mathrm{GHz}$.

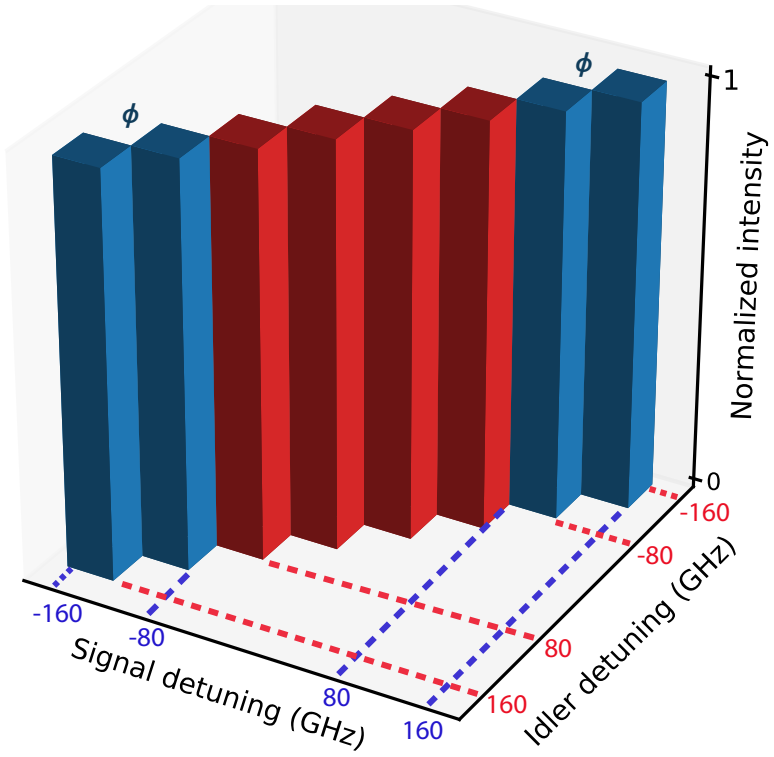

Figure 4-8: JSI calculated for a biphoton with 320-GHz-wide flat-top spectrum. Spectral phase ϕ (none, set to 0) applied to blue (red) shaded region outside (within) the $\pm 80\,\mathrm{GHz}$ span of signal and idler frequency detuning, showing no ϕ dependence.

Although $|\psi^{(2)}\rangle_{SI}$ differs from $|\psi^{(1)}\rangle_{SI}$ when $0 < \phi < 2\pi$, these states cannot be distinguished by Franson or Hong-Ou-Mandel interference because $|\psi^{(2)}\rangle_{SI}$ and $|\psi^{(1)}\rangle_{SI}$ have identical JSIs, as shown in Fig. 4-8, and those interferometers' interference patterns are determined by the JSI. On the other hand, the JTIs of $|\psi^{(2)}\rangle_{SI}$ and $|\psi^{(1)}\rangle_{SI}$ are different, because of JTI's spectral phase dependence. This difference is shown in Figs. 4-9, which display the JTIs of $|\psi^{(2)}\rangle_{SI}$ for $\phi = 0$ and π, respectively, with the former also being the JTI of $|\psi^{(1)}\rangle_{SI}$. Eq. (4.29) indicates that the CFI vis-

ibility is a function of the JTI and thus sensitive to spectral phase. Our theoretical calculation for the CFI visibility yields 95.1% for $|\psi^{(1)}\rangle_{SI}$ and 75.5% for $|\psi^{(2)}\rangle_{SI}$ with $\phi = \pi$. This represents a ∼20% drop in CFI visibility that should be measurable experimentally.

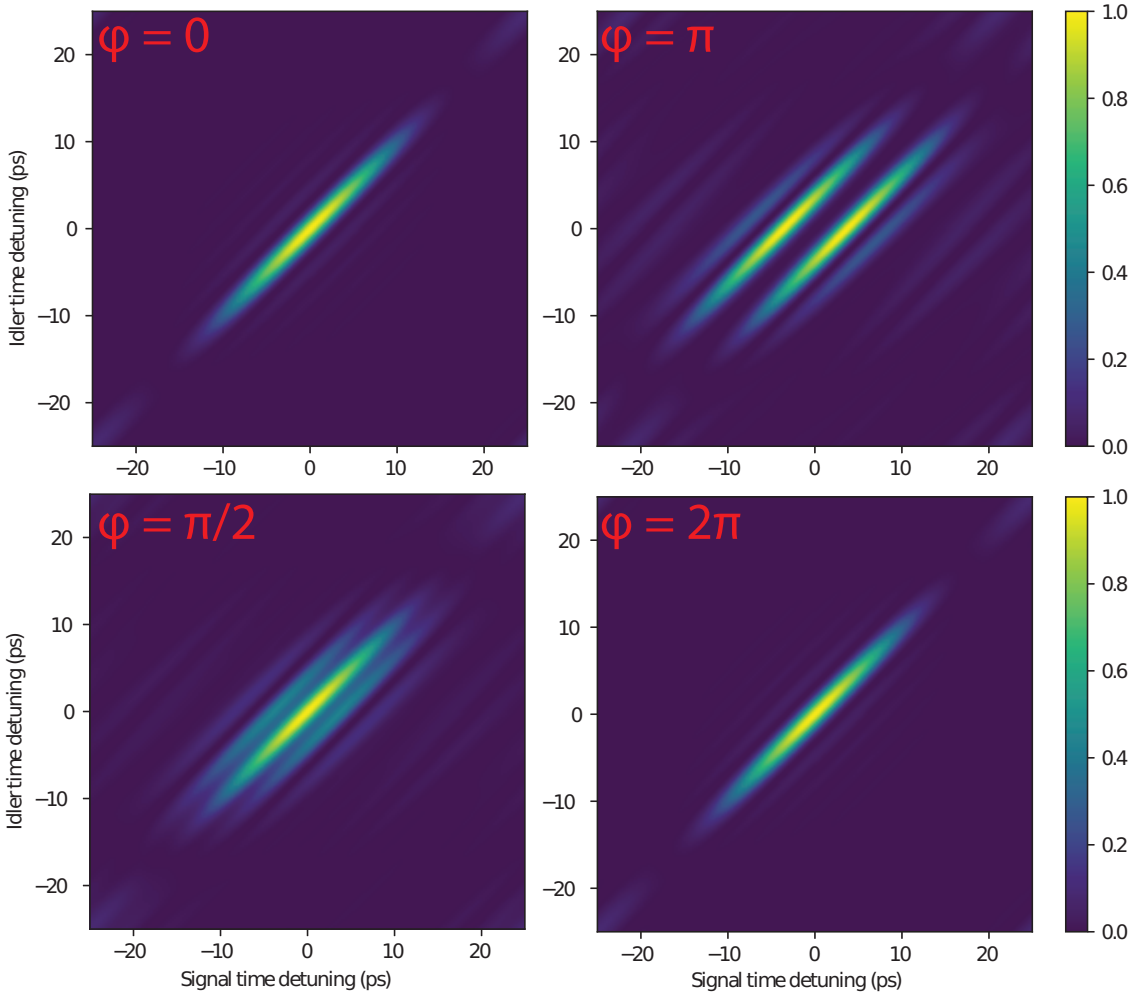

Figure 4-9: JTI of same biphoton state with various imposed phase value ϕ. Maximum of JTI normalized to 1.

We used a type-0 phase-matched PPLN crystal pumped by a 780 nm continuous-wave (cw) laser to generate time-energy entangled photon pairs with a flat spectrum across the telecommunication C band. A 50/50 beam splitter was used to separate the co-polarized signal and idler photons that incurred a 3 dB loss for postselected signal-idler coincidence measurements. The signal and idler had flat spectra across the telecommunication C band. We applied a programmable amplitude and phase

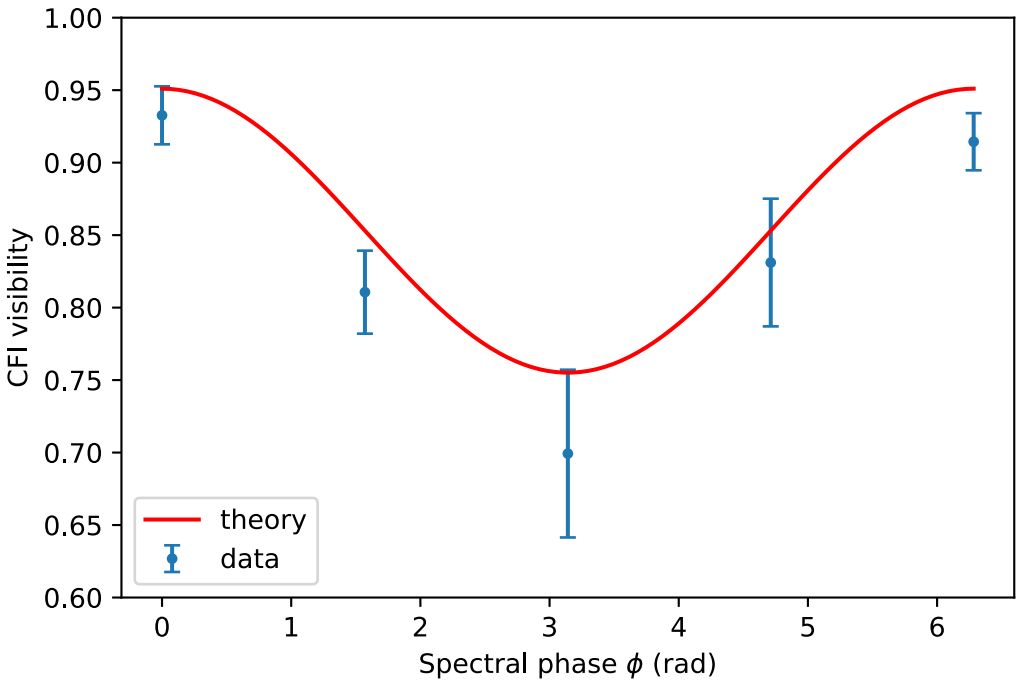

Figure 4-10: Conjugate-Franson fringe visibility as a function of applied spectral phase ϕ of Eq. (4.3). Measured data points (blue) follow closely the calculated values (solid red line) obtained from Eq. (4.29) with a rectangular spectrum of 320 GHz span shown in Fig. 4-8.

spectral filter (Finisar waveshaper 1000S) to shape the signal and idler spectra to be rectangular with a 320 GHz bandwidth and to impose an adjustable phase $e^{i\phi}$ on both signal and idler light for frequency detuning $|\omega|/2\pi$ between 80 to 160 GHz, thus producing the biphoton state $|\psi^{(2)}\rangle_{SI}$. We measured the CFI visibility at $\phi = 0$, $\pi/2$, π, $3\pi/2$, and 2π and Fig. 4-10 displays our results along with the theoretically calculated values. Because $\phi = 0$ or 2π makes $|\psi^{(2)}\rangle_{SI} = |\psi^{(1)}\rangle_{SI}$, the $93.2 \pm 2.0\%$ visibility we obtained for $\phi = 0$ and the $91.4 \pm 2.0\%$ we got for $\phi = 2\pi$, with the uncertainty value being the standard deviation of 3 measurements, are consistent with that equivalence. Figure 4-10 shows that the CFI visibility degrades when spectral phase variation was introduced, reaching a minimum visibility of $72.0 \pm 3.1\%$ for $\phi = \pi$, in good agreement with our calculation. In this simple example, the substantial visibility reduction of 21.2% from $\phi = 0$ to $\phi = \pi$ clearly confirms the ability of the CFI to distinguish between states with different spectral phase content. Our experimental results show that conjugate-Franson interferometry can be used not only for quantifying time-energy entanglement of biphotons but also for detecting their spectral phase differences, which is helpful in characterizing entangled systems with high-dimensional encoding [118, 119].

4.4 Conclusion

In summary, we reported experimental realization of the conjugate-Franson interferometer, which measures the conjugate variables of the Franson interfereometer. We summarize the differences and similarities between the Franson and conjugate-Fanson in Table 4.1.

We have demonstrated experimentally a CFI visibility of $96 \pm 1\%$ without any background subtraction for time-energy entangled photon pairs generated by cw pumped SPDC. The achieved visibility surpasses the quantum-classical threshold of $\sim$71% by 25 standard deviations and clearly validates the quantum entanglement feature between the SPDC signal and idler photons. To illustrate its application potential, we utilized the CFI as an enabling quantum measurement technique to distinguish

Franson interferometer	Conjugate-Franson inteferometer
unbalanced MZI with ΔT path length difference between two paths	balanced MZI with $\Delta\Omega$ frequency difference between two paths
measures signal and idler time coincidences	measures signal and idler frequency coincidences
interference visibility quantifies biphoton's frequency correlation	interference visibility quantifies biphoton's time correlation
interference visibility relates to the biphoton's joint spectral intensity	interference visibility relates to the biphoton's joint temporal intensity
interference visibility is sensitive to temporal phase, not spectral phase	interference visibility is sensitive to spectral phase, not temporal phase

Table 4.1: Similarities and differences between Franson and conjugate-Franson interferometers.

between two biphoton states with identical joint spectral intensities but different joint temporal intensities due to spectral phase variation. By introducing an adjustable spectral phase shift to a cw pumped SPDC biphoton state, we observed a significant CFI visibility drop of 21% between the two biphoton states, matching our theoretical calculations. Our results show that conjugate-Franson interferometry quantifies correlation in the time domain and is complementary to the well-known Franson interferometry. Overall, we expect that the addition of the CFI to the quantum toolbox provides a simpler way than prior techniques for characterizing time-domain correlation and a new method to monitor spectral phase information of time-energy entangled photon pairs. Hence we believe the CFI will enhance future developments of entanglement systems for computing, communication, and sensing applications.

Chapter 5

Frequency domain high-dimensional quantum key distribution

5.1 Introduction

Quantum communication and quantum cryptography enable the secure transfer of information between distant parties. The communication security is safeguarded by the laws of physics. Conventional QKD protocols often encode information using binary format. For example, BB84 uses horizontal (or, alternatively, left-handed circular) polarization to represent bit 0 and vertical (right-handed circular) polarization to represent bit 1. In this encoding scheme, the key capacity, which is also referred to as the photon information efficiency (PIE), is limited to 1 bit per photon. Furthermore, QKD systems typically operate in photon-starved conditions, and therefore the maximum key rate is capped by the PIE and the photon flux. One solution to increase the PIE is to encode information in a high-dimensional Hilbert space. Moreover, encoding in the high-dimensional Hilbert space is more resilient to noise [124].

A few different degrees of freedom have been studied for improving PIE, including time [33], orbital angular momentum [125, 27], position momentum [126], and time-energy [31, 32]. In this chapter, we focus the discussion on a scheme employing frequency domain encoding. We report an experimental demonstration of high-dimensional QKD with frequency encoding using time-energy entangled photon

pairs over a 137-meter fiber link. Its security against a collective Gaussian attack is quantified through conjugate-Franson interferometry. The conjugate-Franson interferometer (CFI) was discussed in Chapter 4. The CFI measurement bounds the time correlation of the entangled photon pairs, which quantifies Eve's Holevo information. In the following sections, we start with the discussion of experimental methods to implement frequency encoding, followed by the formulation to calculate Eve's Holevo information. Finally, we report that we have obtained a secure key rate (SKR) of 42 kbit/s through 137 meters of single-mode fiber with a PIE of 0.6 bit per photon coincidence.

5.2 Methods of encoding in the frequency domain

Wavelength-division multiplexing (WDM) technology multiplexes a number of optical signals with different wavelengths into a single optical fiber and increases the classical communication channel capacity. Here we use WDM technology for a different purpose. We divide the frequency spectrum into different frequency bins using WDM technology and perform projective measurements on the signal and idler's frequencies. The measurement results, correlated in frequency because of the biphoton's time-energy entanglement, can be used to generate correlated keys for communication. The dimension of the encoding alphabet depends on the available spectrum and the number of frequency bins. In general, a larger number of bins leads to higher encoding alphabet dimensions. In this section, we explore and compare three different methods to generate frequency bins for frequency encoding.

5.2.1 Dense wavelength division multiplexing

Dense wavelength division multiplexing (DWDM) systems are pervasive in today's internet network. DWDM wavelengths are positioned in a fixed optical frequency grid with 100 GHz ($\sim$ 0.8 nm) spacing and a reference wavelength at 191.10 THz (1552.52 nm), as defined by the International Telecommunication Union (ITU). A typical DWDM system utilizes thin-film filters to pass or reflect certain wavelengths

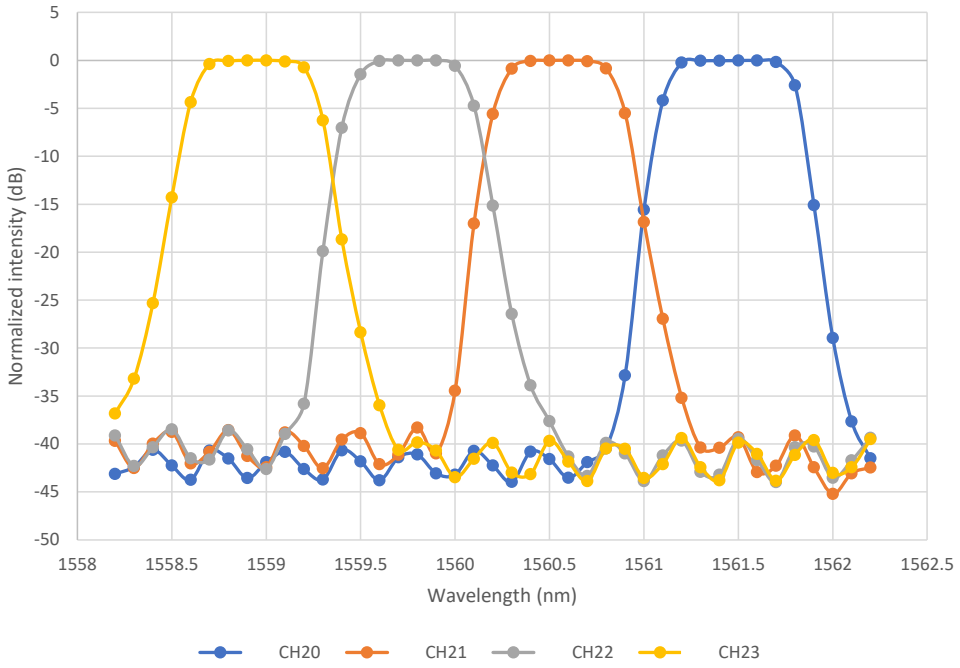

Figure 5-1: Transmission profile of a commercial 4-channel DWDM module at ITU channels 20 to 23.

of interest [127]. A bandpass thin-film filter consists of one or more coupled thin-film Fabry-Perot filters. The filter can be designed to reflect non-resonant wavelength components and transmit the resonant wavelength components. The transmission profile of the thin-film filter can be designed to be an approximately square shape. However, this tends to introduce chromatic dispersion that distorts the input optical signal. In practice, the squareness of the transmission profile is often modified to reduce the chromatic dispersion introduced by the filter design. In Fig. 5-1, we show the measured transmission profile of a commercial four-channel DWDM module that is designed for ITU channels 20-23. We measured a channel insertion loss of $<$1.5 dB and adjacent channel extinction ratio of $>$10 dB. However, the commercial DWDM module is only available with 100 GHz channel spacing in the telecommunication C band. This is not ideal for our QKD system as part of the entangled photons' spectra is in the telecommunication L band. Furthermore, 100 GHz channel spacing is relatively large for our applications as it limits the number of frequency bins available. A DWDM system with 50 GHz channel spacing is available but is more expensive than

the 100 GHz module. The 50 GHz DWDM system features arrayed waveguide grating technology instead of thin-film filters that increases the system design complexity. We note that the DWDM system with smaller channel spacing is also available down to 12.5 GHz using fiber Bragg gratings. However, the small channel spacing systems ($<$50 GHz) are often associated with a high manufacturing cost, which prevents them from large-scale adoption in the telecommunication industry.

5.2.2 Silicon photonics for wavelength multiplexing

A silicon ring resonator transmits certain wavelengths when it is in resonance, making it a viable candidate for frequency binning and frequency selection [128]. In particular, we consider an add-drop ring resonator where there is an add port, a drop port, and a looped optical waveguide. When the optical waves inside the loop accumulate a round trip phase shift that is a multiple of 2π, the cavity is in resonance, and the optical waves interfere constructively. One major issue with the add-drop ring resonator is the coupling loss when light is coupled into and out of the looped waveguide. A large-sized high Q resonator has low coupling loss, but its free spectral range (FSR) is small that it cannot be used over a large spectral bandwidth as it transmits multiple wavelengths over the desired bandwidth. To overcome this issue, Mach-Zehnder interferometers can be placed before a series of high Q ring resonators to coarsely divide the spectrum. Recent research shows an integrated system featuring 640 resonators [129] with a 16 GHz (0.13 nm) channel offset. However, the $\sim$ 33 dB insertion loss of such a system is too high for most applications. A portion of the insertion loss is due to the poor fiber-to-chip coupling. The fiber-to-chip coupling loss can be reduced with a custom inverted taper, which has been shown to feature a 0.8 dB insertion loss per facet [130]. In the future, we believe that the integrated photonics platform is a promising solution for making scalable frequency filters and other devices for quantum communication.

5.2.3 Programmable filter with frequency detection

Both the DWDM system and ring resonator system require multiple detectors. This requirement brings significant experimental overhead in constructing the frequency domain QKD testbed. Alternatively, we use two programmable filters (Finisar Waveshaper 1000S) and two single-photon detectors to emulate a physical multi-channel DWDM system. The programmable filter consists of a $4f$ optical system that transforms the input light into and out of the frequency domain and a spatial light modulator (SLM) system that imposes frequency-resolved phase changes in the frequency domain. The minimum bandwidth for the programmable frequency filters is 12 GHz. However, discretization error due to limitation of the filters can be observed when the filter bandwidth is below 50 GHz. The discretization error leads to uneven insertion loss for different frequency channels. As an alternative, especially for small filter bandwidths, it is better to use a grating-based optical filter, such as EXFO-XTA-50, which has a minimum filter bandwidth down to 1 GHz.

Although the commercial DWDM system or the silicon photonics system offer superior performance to the programmable filter system, they do not have the flexibility to adjust the filter's center frequency. Adjustments of the filter's center frequency are essential to minimize channel crosstalk. This inflexibility is not ideal for testing our frequency-encoded QKD system because our pump laser's frequency is not tunable. For this proof-of-principle experiment, we will investigate the frequency-encoded QKD performance with a programmable frequency filter system.

5.3 Security analysis based on conjugate-Franson interferometry

We use the Gaussian continuous variable QKD framework to assess protocol security. The security analysis is based on the optimality of Eve's Gaussian collective attack for Alice and Bob's time-frequency covariance matrix (TFCM) [35, 33, 131]. The

TFCM for the biphoton state in Eq. (4.16) is

$$\Gamma_0 = \begin{bmatrix} \gamma_{SS}^0 & \gamma_{SI}^0 \\ \gamma_{IS}^0 & \gamma_{II}^0 \end{bmatrix}, \tag{5.1}$$

where

$$\gamma_{SS}^0 = \gamma_{II}^0 = \begin{bmatrix} \sigma_{\text{cor}}^2/4 + \sigma_{\text{coh}}^2 & 0 \\ 0 & 1/4\sigma_{\text{cor}}^2 + 1/16\sigma_{\text{coh}}^2 \end{bmatrix} \tag{5.2}$$

$$\gamma_{SI}^0 = \gamma_{IS}^0 = \begin{bmatrix} -\sigma_{\text{cor}}^2/4 + \sigma_{\text{coh}}^2 & 0 \\ 0 & 1/4\sigma_{\text{cor}}^2 - 1/16\sigma_{\text{coh}}^2 \end{bmatrix}. \tag{5.3}$$

The root-mean-square coherence time, σ_{coh}, is set by the pump pulse's duration; and the root-mean square correlation time, σ_{cor}, is set by the reciprocal of the full width at half-maximum (FWHM) phase-matching bandwidth, B_{PM}, in Hz. Eve's disturbance changes the TFCM to become

$$\gamma_{SS} = \gamma_{SS}^0 \tag{5.4}$$

$$\gamma_{SI} = \gamma_{IS} = \begin{bmatrix} 1-\eta_t & 0 \\ 0 & 1-\eta_\omega \end{bmatrix} \gamma_{SI}^0 \tag{5.5}$$

$$\gamma_{II} = \begin{bmatrix} 1+\epsilon_t & 0 \\ 0 & 1+\epsilon_\omega \end{bmatrix} \gamma_{II}^0, \tag{5.6}$$

where η_t, η_ω are the loss, and $\epsilon_t, \epsilon_\omega$ are the excess noise in Bob's idler photon in the time and frequency correlations, respectively. η_t and ϵ_t are bounded by the conjugate-Franson interference visibility V_{CFI}.

It has previously been shown that $V_{\text{CFI}} = \langle \cos[(\hat{t}_S - \hat{t}_I)\Delta\Omega] \rangle$ [35], where $\hat{t}_{S(I)}$ is the arrival-time measurement operator for signal (idler) photons, and $\Delta\Omega$ is the applied frequency shift in the CFI. We define $t_{\text{MSE}} \equiv (t_{S0} - t_{I0})^2$ to be the mean-square signal-idler timing difference at the source. Taylor expanding the $\langle \cos[(\hat{t}_S - \hat{t}_I)\Delta\Omega] \rangle$ term gives:

$$V_{\text{CFI}}^{\text{th}} = \langle \cos[(\hat{t}_{S0} - \hat{t}_{I0})\Delta\Omega] \rangle \geq 1 - \frac{\langle (t_{S0} - t_{I0})^2 \rangle \, \Delta\Omega^2}{2} \tag{5.7}$$

and

$$V_{\mathrm{CFI}} \leq 1 - \frac{\langle (t_S - t_I)^2 \rangle \, \Delta\Omega^2}{2} + \frac{\langle (t_S - t_I)^2 \rangle^2 \, \Delta\Omega^4}{8}, \tag{5.8}$$

where $V_{\mathrm{CFI}}^{\mathrm{th}}$ is the theoretical maximum conjugate-Franson visibility, and $\hat{t}_{S(I)0}$ is the undisturbed arrival-time measurement operator determined by the source. Combining Eq. (5.7) and (5.8), we can write:

$$0 \leq -\frac{\langle (t_S - t_I)^2 \rangle \, \Delta\Omega^2}{2} + \frac{\langle (t_S - t_I)^2 \rangle^2 \, \Delta\Omega^4}{8} + (V_{\mathrm{CFI}}^{\mathrm{th}} - V_{\mathrm{CFI}} + \frac{\langle (t_{S0} - t_{I0})^2 \rangle \, \Delta\Omega^2}{2}), \tag{5.9}$$

$$\langle (t_S - t_I)^2 \rangle^2 - \frac{4 \langle (t_S - t_I)^2 \rangle}{\Delta\Omega^2} + \frac{8}{\Delta\Omega^4}(V_{\mathrm{CFI}}^{\mathrm{th}} - V_{\mathrm{CFI}} + \frac{\langle (t_{S0} - t_{I0})^2 \rangle \, \Delta\Omega^2}{2}) \geq 0, \tag{5.10}$$

From the quadratic form of Eq. (5.10) equation, we obtain two roots:

$$\langle (t_S - t_I)^2 \rangle = \frac{2}{\Delta\Omega^2}\Big(1 + \sqrt{1 - 2(V_{\mathrm{CFI}}^{\mathrm{th}} - V_{\mathrm{CFI}} + \frac{\langle (t_{S0} - t_{I0})^2 \rangle \, \Delta\Omega^2}{2})}\Big), \tag{5.11}$$

and

$$\langle (t_S - t_I)^2 \rangle = \frac{2}{\Delta\Omega^2}\Big(1 - \sqrt{1 - 2(V_{\mathrm{CFI}}^{\mathrm{th}} - V_{\mathrm{CFI}} + \frac{\langle (t_{S0} - t_{I0})^2 \rangle \, \Delta\Omega^2}{2})}\Big). \tag{5.12}$$

The solution in Eq. (5.11) is rejected because its value is orders of magnitude larger than the experimental value. Therefore, we use the solution of Eq. (5.12) to bound Eve's Holevo information. We note that this bound is valid only when $V_{\mathrm{CFI}} \geq 50\%$. When $V_{\mathrm{CFI}} < 50\%$, the quadratic inequality does not have a solution. In the security analysis, we use ξ_t to quantify the change of the timing difference t_{MSE}. The signal-idler timing difference becomes larger as the entanglement quality degrades, which can be written as: $\langle (t_S - t_I)^2 \rangle = (1 + \xi_t) \langle (t_{S0} - t_{I0})^2 \rangle$. Combined with Eq. (5.12), we can write ξ_t as:

$$\xi_t = \frac{2}{\Delta\Omega^2 t_{\mathrm{MSE}}}\Big[1 - \sqrt{1 - 2(V_{\mathrm{CFI}_0} - V_{\mathrm{CFI}} + \frac{t_{\mathrm{MSE}} \Delta\Omega^2}{2})}\Big] - 1, \tag{5.13}$$

where $t_{\mathrm{MSE}} \equiv \langle (t_{S0} - t_{I0})^2 \rangle$. On the other hand, η_ω and ϵ_ω are bounded by the Franson interference visibility. However, in frequency encoding QKD, any disturbance caused

by Eve in the frequency domain increases the error rate of the key generation process and it is easily detectable. Here, we assume that Eve's disturbance does not affect the frequency correlation and has a negligible impact on Eve's Holevo information. In the security analysis, we define the mean-square frequency sum at the source to be $\Omega_{\mathrm{MSE}} \equiv \langle(\Omega_{S0} + \Omega_{I0})^2\rangle$. Similarly, the change in frequency sum is $\langle(\Omega_S + \Omega_I)^2\rangle = (1 + \xi_\Omega)\Omega_{\mathrm{MSE}}$. The experimental frequency sum resolution is determined by the detector jitter and the dispersion module.

We assume Alice, Bob, and Eve all share a pure Gaussian state because a Gaussian attack maximizes Eve's Holevo information for a given TFCM. Eve's Holevo information for covariance matrix Γ can be written as [35]:

$$\chi_\Gamma(A;E) = S(\hat{\rho}_E) - \int dt p(t_A) S(\hat{\rho}_{E|T_A=t_A}), \tag{5.14}$$

where $S(\hat{\rho}) = -\mathrm{Tr}[\hat{\rho}\log_2(\hat{\rho})]$ is the von Neumann entropy of the state $\hat{\rho}$. Because Alice, Bob, and Eve's joint quantum state is pure, we can write $S(\hat{\rho}_E) = S(\hat{\rho}_{AB})$. Conditioned on Alice's measurement, the quantum state shared by Bob and Eve is also pure. Thus we can write $S(\hat{\rho}_{E|T_A=t_A}) = S(\hat{\rho}_{B|T_A=t_A})$. Moreover, Bob and Eve's conditional quantum state is independent of Alice's measurement result. We can simplify Eq. (5.14) to be:

$$\chi_\Gamma(A;E) = S(\hat{\rho}_{AB}) - S(\hat{\rho}_{B|T_A}). \tag{5.15}$$

Eve's Holevo information can be estimated by the upper bound of Eq. (5.15). For example:

$$\chi^{\mathrm{UB}}_{\epsilon_t,\epsilon_\omega}(A;E) = \sup_{\Gamma\in\mathcal{M}} \chi_\Gamma(A;E), \tag{5.16}$$

where $\mathcal{M}$ is the set of physically-allowed TFCMs.

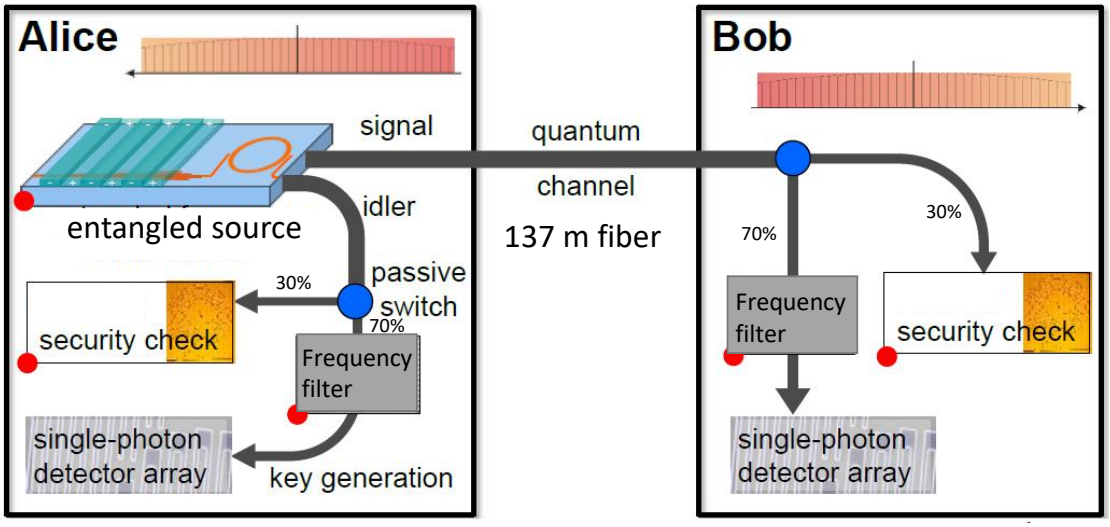

Figure 5-2: Schematic of frequency domain high-dimensional quantum key distribution experimental setup.

5.4 Demonstration of frequency bin quantum key distribution over fiber

Having established a framework to generate raw communication keys and bound Eve's Holevo information, we now demonstrate a proof-of-principle experiment on frequency domain high-dimensional quantum key distribution. Alice used a type-0 periodically-poled lithium niobate (PPLN) crystal as the entangled photon pair source. Because the signal and idler photons are co-polarized, she used a 50/50 beam splitter to passively separate them, incurring a 3 dB loss. Alice kept the idler photon and sent the signal photon to Bob via a 137-meter fiber channel. Alice and Bob both used 70/30 passive beam splitters to randomly switch the photon between key generation or security check. If both signal and idler were sent for key generation, they passed through frequency filters and were detected using superconducting nanowire single-photon detectors (SNSPDs). If both photons were sent for security check, Alice and Bob utilized the CFI setup shown in Fig. 4-1 for frequency coincidence measurement. Otherwise, photon coincidence cannot be registered and such events are discarded. A schematic of the experimental setup is shown in Fig. 5-2.

In this demonstration, we use Alice and Bob's 70/30 beam splitters to select

$\sim$50% (0.7^2) and $\sim$10% (0.3^2) of photon pairs for generating keys and security check, respectively. For key generation, the effective success probability is less than 1% because of channel selection (1/16) and insertion losses of the programmable frequency filters and other components. Similarly, for CFI security check, the success probability is also low due to insertion losses of the frequency shifters in each of the two MZIs. As a result, using a different splitting ratio can significantly affect the signal-to-noise ratio (SNR) ratio of both key generation and CFI measurement that determines the required measurement time of a QKD session. For example, changing the splitting ratio to 50/50 will increase the CFI's SNR, but the key generation SNR will be decreased. As a result, it will take more time for the key generation measurement to achieve the same SNR as in the 70/30 case. Low SNR in key generation results in a low adjacent channel extinction ratio, which leads to an increase of the communication error rate and ultimately a low raw communication key rate. Here, we chose the splitting ratio so that enough SNR (maximum coincidence count detected $>$ 3000) can be achieved for key generation at 1 second integration time. At the same time, the CFI setup can detect $\sim$ 130 coincidence counts per 30 seconds.

The spectral range of the QKD system is restricted to 640 GHz centered from 1557.85 nm (192.44 THz) to 1563.05 nm (191.80 THz) due to passband limitation of the dispersion modules used in the CFI. The signal and idler spectra are assumed to be flat. We set the programmable frequency filter's bandwidth to be 40 GHz with a tunable center frequency to emulate 16 frequency bins within the 640 GHz range. In Table 5.1, we list the physical parameters for the frequency domain high-dimensional QKD experiment. These parameters are also used for calculating the PIE and the SKR.

5.4.1 Raw key generation and information reconciliation

We used a type-0 PPLN crystal to generate time-energy entangled photon pairs. The PPLN crystal was designed to have a broadband phase-matching function with a few THz bandwidth [132]. The PPLN crystal was 4-cm long and operated at 89.4°C. The crystal was pumped by a 780.2-nm continuous-wave (cw) laser at 12

Parameters	Definitions	Values
$\mathrm{d}t$	Detector's FWHM timing jitter (s)	150×10^{-12}
B_{PM}	QKD system bandwidth (Hz)	640×10^{9}
β_2	Dispersion module 2$^{\mathrm{nd}}$ order dispersion (second/Hz)	$8.3{\times}10^{-20}$
$\mathrm{d}\Omega/2\pi$	FWHM frequency resolution (Hz)	$1.8{\times}10^{9}$
$\Delta\Omega/2\pi$	Conjugate-Franson frequency shift (Hz)	15.65×10^{9}
V_{CFI_0}	Maximum CFI visibility for 640 GHz spectrum	97.5%

Table 5.1: List of parameters for frequency encoding QKD system. The maximum CFI visibility is calculated using Eq. (4.29) and the 640 GHz spectrum.

mW power. To benchmark the output flux of the PPLN source, we used a coarse wavelength-division multiplexing (CWDM) module to separate the signal and idler photons. The CWDM's two output channels have 20 nm bandwidth and their center wavelengths are 1551 nm and 1571 nm. At 0.078 mW of pump power, we measured ∼27400 coincidences per second. The singles of both detectors were ∼ 66500 per second. Therefore, the system efficiency of this source for this particular signal-idler separation scheme was 41%. We note that this is not how we separate the signal and idler in all of the experiments discussed in this chapter. This particular measurement was done to provide information for comparing the source's system efficiency.

Because the signal and idler have the same polarization, they cannot be separated by their polarizations. Therefore, we can only measure the combined spectrum of the signal and idler photons. We used a tunable filter (EXFO-XTA50) with 0.2 nm passband to measure the output spectrum. The measurement result is shown in Fig. 5-3. We fitted the spectrum with a double Gaussian function and estimated that the signal (idler) full width at half maximum (FWHM) bandwidth to be 9.5 THz. In the wavelength range of interest, from 1557.85 nm (192.44 THz) to 1563.05 nm (191.80 THz), the signal-idler spectral power is uniform.

In an ideal situation, we would like the programmable filter to have 16 channels where each channel is connected to an SNSPD. This 16-channel system is realizable in principle by having a fan-out system inside the programmable filter. Nevertheless, for this experiment, we use two single-channel programmable filters and two SNSPDs to emulate the performance of the 16-channel system. We set the programmable filter to

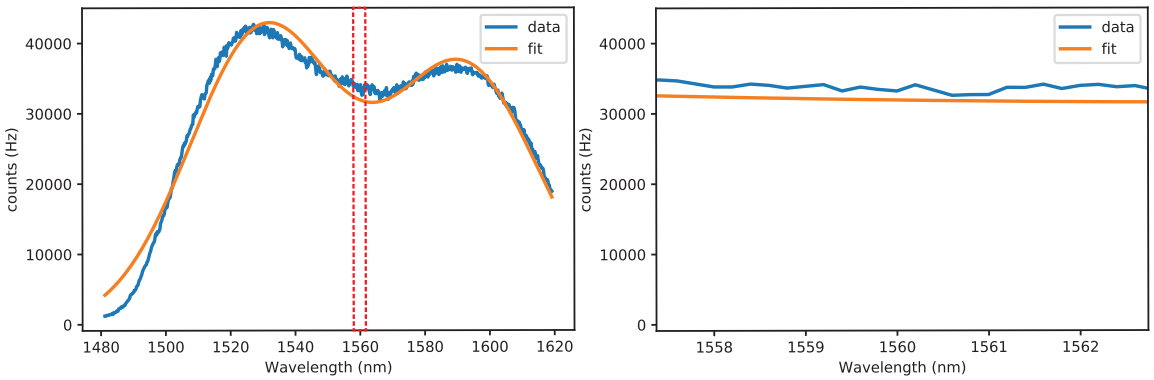

Figure 5-3: Left: Spectrum of the output from the PPLN crystal. Rectangular section is the spectrum of interest. Right: signal and idler's spectra of interest from 1557.85 nm (192.44 THz) to 1563.05 nm (191.80 THz). The resolution of this spectrum measurement is 0.2 nm.

have a 40 GHz passband with a variable center frequency. For the 16-channel system, there are 256 combinations for Alice and Bob's frequency measurements. Therefore, we need to take 256 measurements to emulate the 16-channel system performance. For each pair of Alice and Bob's filter settings, we integrated for 1 s with a 2 ns coincidence window. As a result, one set of key generation measurements would take 256 seconds to complete. The measured coincidences become our raw keys, as shown in Fig. 5-4.

We measured an average coincidence rate of $\sim$ 4400 coincidences/s for matched frequency bins for the programmable filters. Our detected singles count rate was $\sim$ $55,000$/s. As a result, the estimated photon pairs generation rate is $(55,000)^2/4400 \approx$ $687,500$/s. The pair generation probability for the 2 ns coincidence window is calculated to be 0.0014. One key performance specification is the extinction ratio between the correct frequency bins and their adjacent channels. Here, we measured the extinction ratio to be at least 13 dB. This extinction ratio is affected by how well the center frequencies of the frequency filters were lined up relative to the degenerate frequency (half the pump laser frequency). Optimally, the degenerate frequency should be exactly at the middle of the two center frequencies. In our experiment, this extinction ratio is limited by the setting resolution of the programmable filters' center frequencies.

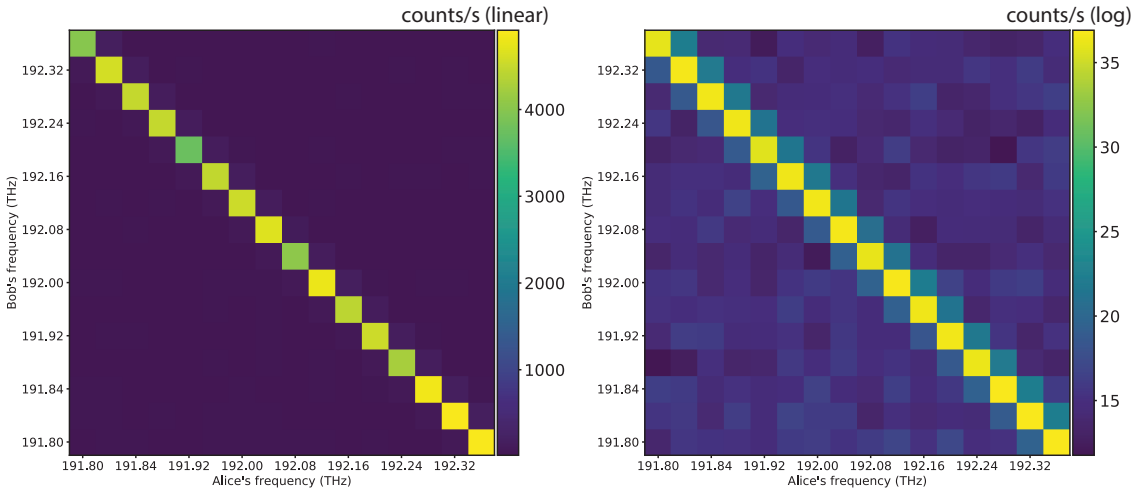

Figure 5-4: Measurement result of frequency bin coincidences for raw key generation. Left: measured keys in linear scale. Right: measured keys in log scale. Alice's and Bob's frequencies shown are the starting frequencies of the frequency bins. The center frequency of the frequency bin is 20 GHz higher than the starting frequency bin.

We consider the coincidence measurements of 256 Alice and Bob's frequency bin pairs to constitute one QKD session. As a result, the measurement results shown in Fig. 5-4 are considered to be from one QKD session and it took 256 seconds to complete. We performed five QKD sessions and calculated the average probability of getting a coincidence for each pair of the 256 frequency bin combinations. The calculated probability mass function (pmf) is shown in Fig. 5-5. We note that the total probability of all 256 frequency bins is normalized to 1. From this pmf, we can observe 16 peaks with probabilities around 5%. These peaks are the diagonal coincidences observed in Fig. 5-4. The variation of the probability is caused by the discretization effect of the programmable filters, which is discussed in Sect. 5.2.3.

Alice and Bob's Shannon information, I_{ab}, can be calculated from the pmf function. Specifically, the Shannon information is given by

$$I_{ab} = \sum_{\mathrm{bin_A},\mathrm{bin_B}} p(\mathrm{bin_A},\mathrm{bin_B}) \frac{p(\mathrm{bin_A},\mathrm{bin_B})}{p(\mathrm{bin_A})p(\mathrm{bin_B})}, \tag{5.17}$$

where $\mathrm{bin_A}$ and $\mathrm{bin_B}$ are the frequency bin numbers, ranging from 1 to 16, for Alice and Bob, respectively. $p(\mathrm{bin_A},\mathrm{bin_B})$ is the joint probability distribution given

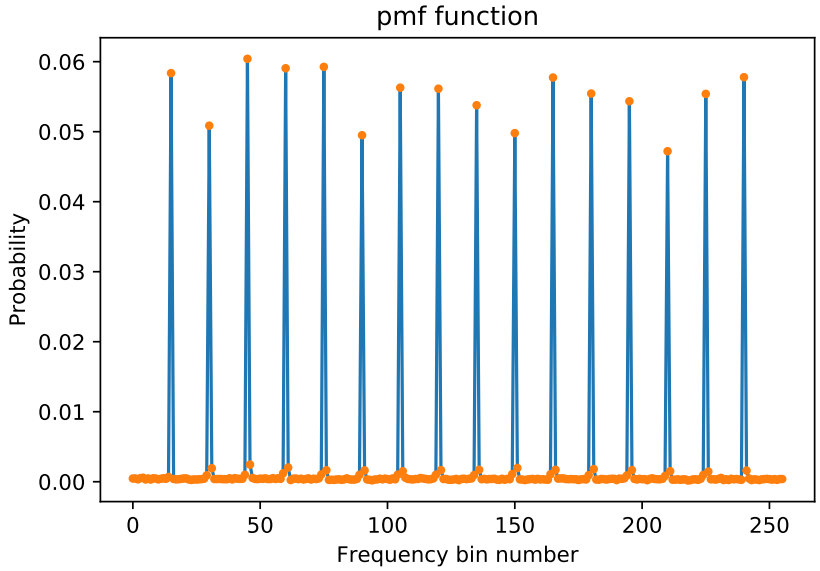

Figure 5-5: Calculated probability mass function (pmf) of coincidence probability for 256 frequency bins.

by the pmf, and $p(\text{bin}_{\text{A(B)}})$ is the marginal coincidence probability distribution for Alice's (Bob's) frequency bin. Based on our measurement, the I_{ab} is found to be 3.06 bits/coincidence. This calculated I_{ab} is $\sim 24\%$ lower than the theoretical maximum of 4 bits/coincidence. The I_{ab} degradation is mainly caused by channel crosstalk and system dark counts.

To obtain a set of raw keys, we simulate coincidence events based on the calculated pmf function. We generate $71,000$ events from the distribution. The 71,000 is the average number of counts we expect to detect per second for the 16-bin frequency filters. In the generated raw key data, we observe an error rate of $\sim 12\%$, consistent with the pmf function. Error correction on the raw keys is performed using layered low-density parity-check (LDPC) code that was developed for large-alphabet quantum key distribution [133]. The layered LDPC code successively applies binary error correction on all bit layers of the symbols, and can achieve high reconciliation efficiency β even when the error rates are high. After error correction with blocks of 20,000 symbols each, Alice and Bob's shared information is found to be 2.7 bits/coincidence, representing a reconciliation efficiency β of 87%.

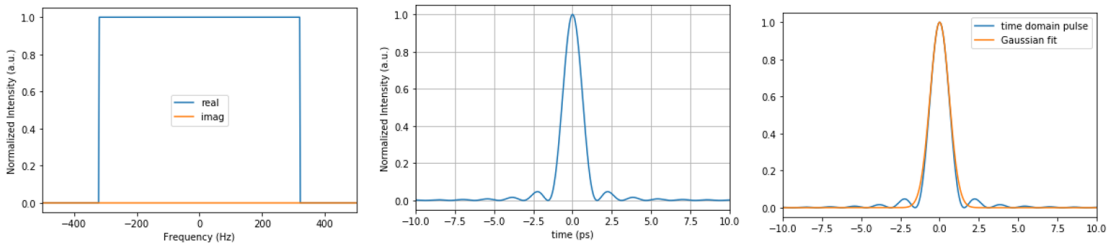

Figure 5-6: Left: frequency domain signal with 640 GHz spectrum bandwidth. Middle: time domain signal of 640 GHz spectrum. Right: Gaussian fit of the time-domain signal.

5.4.2 Measurement of Eve's Holevo information

To numerically calculate Eve's Holevo information, we need to estimate t_{MSE}, which is the square of the root-mean-square correlation time, σ_{cor}. To find σ_{cor} over the predefined 640 GHz rectangular spectrum, we first Fourier transform the rectangular spectrum to get its time domain representation. We fit the time domain signal using Eq. (4.16) and get a FWHM pulse width of 1.43 ps, which corresponds to a σ_{cor} value of $1.43/2.355 = 0.608$ ps. The pictorial representation of this calculation is shown in Fig. 5-6. The mean-square $\Omega_S + \Omega_I$ at the source is $\Omega_{\mathrm{MSE}} = 1/(4\sigma_{\mathrm{coh}}^2)$, where $\sigma_{\mathrm{coh}}^2 = 2\pi \times B\mathrm{pm} \times \beta_2/\sqrt{8\log(2)}$. The correlation degradation in time domain and frequency domain, ξ_t and ξ_ω, can then be calculated using the method described in Sect. 5.3. Eve's Holevo information depends on the conjugate-Franson visibility, as shown in Eq. (5.16). Her information can be tightly bound with a high visibility. Eve's Holevo information decreases exponentially when the conjugate-Franson visibility is greater than 95%. Eve's Holevo information decreases linearly as visibility decreases from 90% to 50%. Therefore, a high conjugate-Franson visibility is desirable for achieving high SKR in frequency domain high-dimensional QKD.

For the five QKD measurement sessions, CFI visibilities were measured at the same time to probe the protocol's security. For each measurement, the CFI's phase was changed adaptively using the piezo transducer (PZT) stack, which is described in Sect. 4.2.6. The average CFI visibility is found to be $95.8 \pm 1.2\%$, where the uncertainty is the standard deviation of five measurements. From the measured visibility, we calculate Eve's Holevo information to be 2.1 bits/coincidence. Therefore,

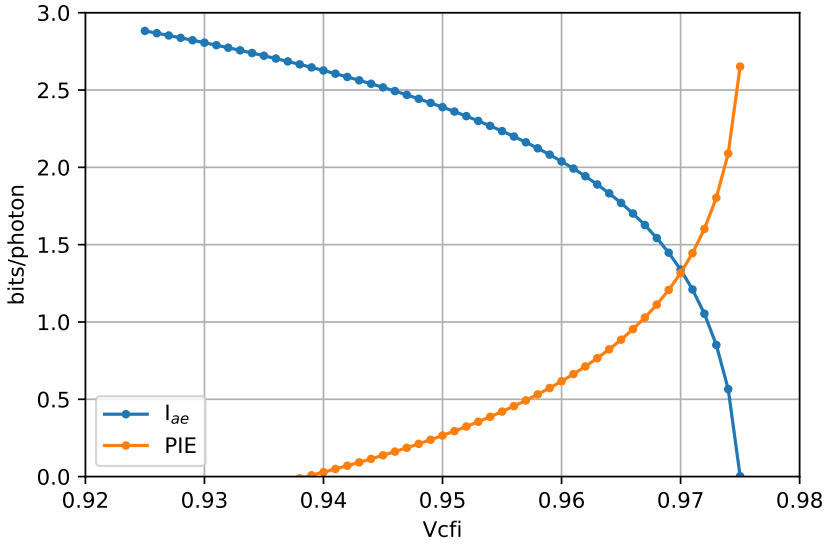

Figure 5-7: Eve's Holevo information, I_{ae}, and PIE as a function of CFI visibility. The maximum PIE is set to be 2.7 bits/photon coincidence, which is given by $I_{ab} = 3.06$ bits/photon multiplied by $\beta = 0.87$. All parameters used for calculation are listed in Table 5.1.

the secret key transmitted per photon coincidence is found to be $2.7 - 2.1 = 0.6$ bits/coincidence, which corresponds to an SKR of $0.6 \times 71000 = 42600$ bits/s. To visually show the effect of Eve's Holevo information on the PIE, we plot both the calculated Eve's Holevo information and the corresponding PIE as a function of the CFI visibility in Fig. 5-7. From the calculated result, we see that the CFI visibility needs to be greater than 93.8% to obtain a non-zero PIE.

The above calculations are done in the asymptotic limit, which assumes Alice and Bob's keys and the data subset used for parameter estimation were infinitely long. To estimate the finite key effect on Eve's Holevo information, Alice and Bob need to calculate their normalized time correlation from measured conjugate-Franson visibilities via Eq. (5.13), which has a χ^2 distribution [33]:

$$(m-1)\frac{\langle(\hat{t}_S - \hat{t}_I)^2\rangle}{\langle(\hat{t}_{S0} - \hat{t}_{I0})^2\rangle} \sim \chi^2(1-\epsilon_{PE}, m-1), \tag{5.18}$$

where ϵ_{PE} is the probability when security parameter estimation failed, and m is the number of conjugate-Franson visibility measurements within each session. An upper

bound on $\langle (t_S - t_I)^2 \rangle$ with confidence interval $1 - \epsilon_{PE}$ is given by:

$$\langle \hat{t}_S - \hat{t}_I)^2 \rangle_{\max} = \langle \hat{t}_{S0} - \hat{t}_{I0})^2 \rangle + \frac{2}{\sqrt{m}} \mathrm{erf}^{-1}(1 - \epsilon_{PE}) \langle \hat{t}_S - \hat{t}_I)^2 \rangle . \tag{5.19}$$

In each QKD session, we only made one conjugate-Franson visibility measurement. Therefore, it is difficult to estimate the finite key effect with a tight bound. Typical estimations choose $\epsilon_{PE} = 10^{-5}$ [33, 134]. In this case, the number of measurements per QKD session needs to be greater than 10 to have a non-zero secret key rate given our CFI visibility measurement result. The insertion loss of the CFI needs to be improved by at least 10 dB in order to achieve 10 measurements per QKD session. In the future, we believe this can be achieved through photonic integration of CFI components.

5.4.3 Franson time delay and conjugate-Franson frequency shift

In Eq. (5.12), we see that the timing difference is inversely proportional to the square of the applied frequency shift $\Delta\Omega^2$. Therefore, a larger $\Delta\Omega$ indicates a tighter bound on Eve's Holevo information, yielding a higher SKR. We note that the calculation of Eve's Holevo information is independent of Alice and Bob's number of frequency bins. To illustrate this point, we calculate Eve's information assuming different $\Delta\Omega$ values, while keeping all other parameters the same. The results are shown in Fig. 5-8. The calculation results show that the maximum of Eve's accessible information reduces from ~ 5.2 bits/photon to ~ 0.7 bits/photon when $\Delta\Omega$ increases from 3 GHz to 100 GHz, given that the measured visibility is 5% lower than the ideal conjugate-Franson visibility. We note that the theoretical maximum value of conjugate-Franson interference visibility decreases as $\Delta\Omega$ increases, and that Eve's information is bounded by the difference between the measured visibility and the maximum visibility.

A similar behavior is expected for the time-bin QKD protocol [33]. In time domain high-dimensional QKD, the mean-square frequency difference $\langle (\omega_S - \omega_I)^2 \rangle$ is bounded by

$$\langle (\omega_S - \omega_I)^2 \rangle \leq 2(V_{\mathrm{FI}}^{\mathrm{th}} - V_{\mathrm{FI}})/\Delta T^2, \tag{5.20}$$

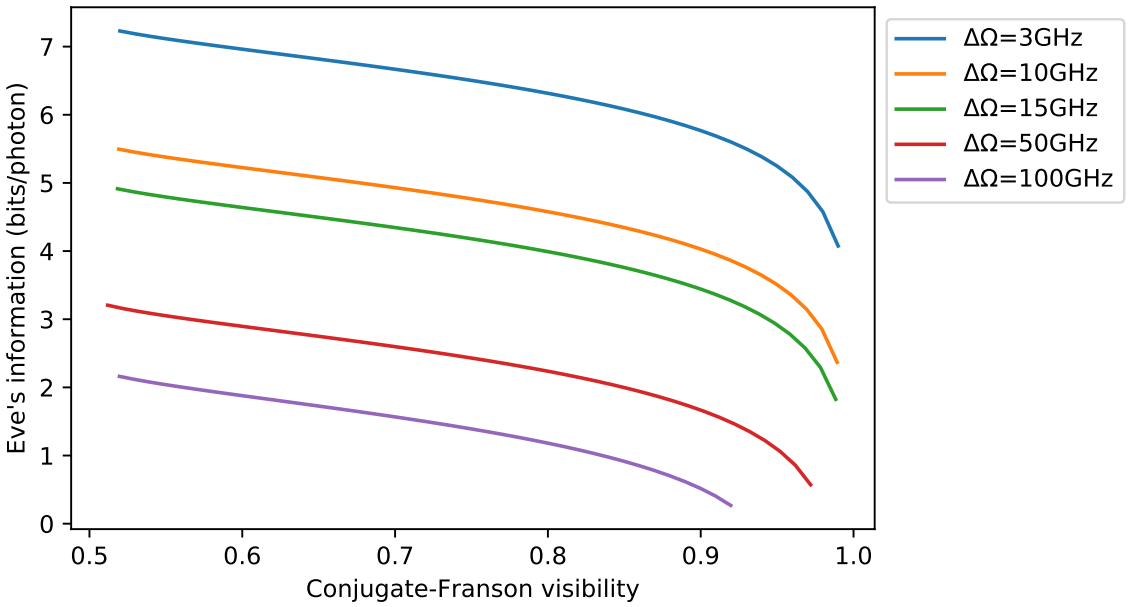

Figure 5-8: Eve's Holevo information as a function of conjugate-Franson visibility at different frequency shift $\Delta\Omega$.

where $V_{\mathrm{FI}}^{\mathrm{th}}$ is the theoretical Franson visibility, V_{FI} is the measured Franson visibility, and ΔT is the path-length difference within the Franson interferometer. A greater path-length difference ΔT decreases the mean-square frequency difference, allowing a tighter bound on Eve's Holevo information. This observation is in agreement with the findings in [135].

For the rest of this section, we compare the effect of ΔT and $\Delta\Omega$ on Eve's Holevo information. Specifically, given the same level of Franson (conjugate-Franson) interference visibility, we compute the corresponding path-length difference ΔT (frequency shift $\Delta\Omega$). In this calculation, we use the parameters shown in Table. 5.1. For a Gaussian input state, the ideal Franson interference visibility V_{FI_0} and the ideal conjugate-Franson interference visibility V_{CFI_0} can be expressed as:

$$V_{\mathrm{FI}_0} = e^{-\Omega_{\mathrm{MSE}}\Delta T^2/2}, \tag{5.21}$$

and

$$V_{\mathrm{CFI}_0} = e^{-t_{\mathrm{MSE}}\Delta\Omega^2/2}. \tag{5.22}$$

Therefore, we can rewrite them as $\Delta T = \ln(-2V_{\mathrm{FI}_0}/\Omega_{\mathrm{MSE}})$ and $\Delta\Omega = \ln(-2V_{\mathrm{CFI}_0}/t_{\mathrm{MSE}})$. Using these two equations, we compute these two values given the same maximum theoretical visibility and show them in Table 5.2. To achieve the same level of theoretical visibility, the amount of frequency shift $\Delta\Omega$ in GHz is similar to the amount of path-length difference ΔT in ns. In CFI, $\Delta\Omega$ can be easily adjusted by changing the RF input frequency. However, it is difficult to increase $\Delta\Omega$ beyond 20 GHz. On the other hand, ΔT can be easily increased by adding new fiber. Unfortunately, change of path-length difference in Franson interferometer requires realignment of the physical interferometer.

Visibility	$\Delta\Omega$ (GHz)	ΔT (ns)
0.999	11.7095	12.7314
0.998	16.5639	18.0094
0.997	20.2917	22.0624
0.996	23.4367	25.4818
0.995	26.2096	28.4967
0.994	28.7184	31.2244
0.993	31.0272	33.7347
0.992	33.1778	36.073
0.991	35.1993	38.2708
0.99	37.1126	40.3512
0.96	74.796	81.3229
0.91	113.687	123.608
0.86	143.769	156.315
0.81	169.936	184.765
0.76	193.933	210.857
0.71	216.649	235.554
0.66	238.63	259.453
0.61	260.271	282.982
0.56	281.889	306.487
0.51	303.774	330.282

Table 5.2: Conversion table between $\Delta\Omega$ in frequency domain QKD and ΔT in time domain QKD.

5.5 Conclusion

In this chapter, we presented a proof-of-principle experimental demonstration of the frequency-encoded high-dimensional quantum key distribution protocol. Within the 640 GHz spectrum centered at ∼192.12 THz (1560.45 nm), we obtained 16 frequency bins using programmable filters with 40 GHz bandwidth. By adopting frequency-bin encoding, we obtained a 12% quantum bit error rate, which is better than the 30% reported in the time-bin encoding scheme. The security of this protocol was guaranteed by the conjugate-Franson interference visibility measured during the key generation process. Over the 137 meters fiber link, we measured a secure PIE of 0.6 bits/coincidence, corresponding to an SKR of 42600 bits/s.

The performance of this system is limited by the difficulty to tightly bound Eve's Holevo information. Current measurements of CFI interference visibility of 95.8% indicates a 1.7% degradation from the theoretical maximum value. An average of 97.3% visibility is needed to bound Eve's Holevo information to be less than 1 bit/coincidence. Alternatively, one can also increase the frequency shift amount in the CFI to tighten the bound on Eve's information. CFI has to have a low insertion loss, large frequency shift range, and good phase stability to achieve this objective. Photonics integration of the optical components in the CFI offers great potential for achieving these goals. Furthermore, optical filters with micro rings can be developed to increase the frequency bin density per unit frequency hence increasing the key capacity. We believe with better dispersion modules and frequency filters, the operational frequency range can increase from 640 GHz to 1 THz with 20 GHz filter bandwidth, resulting in a key capacity of $\log_2(50) \approx 5.6$ bits/coincidence. Assuming an Eve's Holevo information of 1 bit/coincidence (CFI visibility degradation $\leq$0.2%) and a measurement error comparable to our current setup, we expect the PIE can be increased to 2.6 bits/coincidence. With photon sources that have ∼1 GHz photon pair rate, we expect the frequency encoding high-dimensional QKD can reach Gigabits/s SKR, providing sufficient bandwidth for point-to-point secure communication.

Chapter 6

Summary and outlook

In this thesis, we harnessed time-energy entanglement for applications in quantum communication. Specifically we generated indistinguishable single photons by eliminating time-energy entanglement in the spontaneous parametric down-conversion (SPDC) process through custom crystal design; we demonstrated a novel method for entangled photon pairs' time correlation characterization and biphoton spectral phase detection; and we conducted a proof-of-principle experiment on high-dimensional quantum key distribution (QKD) with frequency encoding. In this chapter, we summarize our results and discuss future research directions in these areas.

6.1 Heralded single-photon source

Heralding detection of the signal photon generated from the SPDC process provides timing information of the idler photon. The precise timing of the idler photon is critical for measurement-based quantum information. However, the heralded idler photons are in a spectrally mixed state because of the signal and idler's time-energy entanglement. We achieved a 99% heralded-state purity with a custom designed periodically poled $KTiOPO_4$ (PPKTP) crystal that possesses a Gaussian phase-matching function under extended phase-matching conditions [46, 67]. We further performed Hong-Ou-Mandel interference (HOMI) between two independently generated heralded photons and obtained $93.9 \pm 1.8\%$ without filtering and $98.4 \pm 1.1\%$ with mild filtering, which

is consistent with our expectation.

For future quantum networking tasks or measurement-based quantum simulation experiments, a large number of indistinguishable heralded quantum sources are required. Nevertheless, the current crystal design is not suitable for large-scale manufacturing. Therefore, a promising future research direction is to apply this crystal design on an integrated photonics platform. The capability of manufacturing indistinguishable sources at scale is beneficial for the development of the multiplexed single-photon source and large-scale quantum simulation experiments such as Boson sampling with >100 input modes.

6.2 Conjugate-Franson interferometry

We have demonstrated a conjugate-Franson interferometer (CFI) with quadrature phase-shift keying (QPSK) modulators and optical fibers and achieved $96 \pm 1\%$ interference visibility. We have also shown that the CFI visibility is sensitive to the biphoton spectral phase. The maximum visibility drop observed in our experiment due to the spectral phase is 21%.

The performance of our CFI was limited due to its high insertion loss and poor phase stability. A major portion of the insertion loss comes from the frequency shifters. A future research direction is to reduce the CFI insertion loss by replacing the QPSK frequency shifter with a phase modulator that imposes a linear temporal phase on the optical pulse. The frequency conversion scheme with linear temporal phase has minimal insertion loss [70]. We can also reduce the frequency shifter's insertion loss by applying a RF signal with higher amplitude. In this case, we need to consider how the noise sidebands affect the interference visibility. Another improvement is to reduce the CFI's phase instability. The CFI can be integrated on-chip and the entire chip can be thermally stabilized to maintain long-term phase stability. A controllable phase shift within the CFI can be realized through localized heating [136] or the free-carrier plasma dispersion effect [137].

CFI's role in biphoton frequency combs can also be investigated. The CFI visibility

as a function of frequency shift has been shown to exhibit a comb-like revival structure [119]. Our work has shown that the CFI is affected by spectral phase, indicating that the CFI could be a useful tool for biphoton frequency comb characterization.

6.3 Quantum key distribution with frequency encoding

We have shown a high-dimensional QKD system with frequency encoding that delivers a 0.6 bit/coincidence secure photon information efficiency (PIE), or 42.6 kbit/s secure key rate (SKR), over 137 meters of fiber. For future research, one can improve the QKD's performance in the following aspects:

- The current system has a 640 GHz operation bandwidth with 40 GHz frequency filters. This setting corresponds to 16 frequency bins and a theoretical maximum of 4 bits/coincidence PIE. Increasing the operating bandwidth and decreasing the frequency filter's passband can improve the PIE. One can explore a new method for photon-frequency detection. On an integrated platform, one can utilize optical gratings and array single-photon nanowire detectors with spatial resolution [138]. The grating converts photons' frequency information to spatial information. The array detector can resolve this spatial information and hence detect the photons' frequencies. This scheme is more compact and has the potential to achieve a higher PIE than the methods discussed in Sect. 5.2.

- Eve's Holevo information is bounded by the CFI visibility and found to be 2.1 bits/coincidence. The CFI visibility or the frequency shift of the CFI can be increased to reduce Eve's Holevo information.

- Another improvement is to extend the transmission distance of the QKD system. However, because the CFI is sensitive to spectral phase, dispersion compensation is required for long-distance transmission. The SPDC flux can also

be increased by optimizing the entangled source design. We expect the photon pair generation rate can be increased to be $> 10^7$ pairs/mW/s [102], improving the SKR rate by over 20 dB.

Appendix A

Spectral filter transmission profile

We applied a 10-nm spectral filter to the SPDC output in order to remove the residual side lobes of the signal-idler JSI that are clearly visible in the Fig. 2-1(a) and reproduced here in Fig. A-1's inset. For optimal filtering, it is ideal to have unity transmission over the central peak and sufficient absorption in the side lobes such that the SPDC flux remains about the same and the JSI becomes more circularly symmetric, thereby improving the heralded-state spectral purity. Figure A-1 shows the measured transmission profile of the flat-top spectral filter and the signal spectrum obtained from the marginal distribution of the JSI. We see that the filter transmission profile fully covers the SPDC spectrum with little attenuation of the central peak, suggesting that the spectral filter introduces negligible loss to the main lobe of the SPDC output. The mild spectral filtering allows us to improve the Hong-Ou-Mandel interference visibility from 93.9% without filtering to 98.4% with filtering as noted in the main text of Chapter 2.

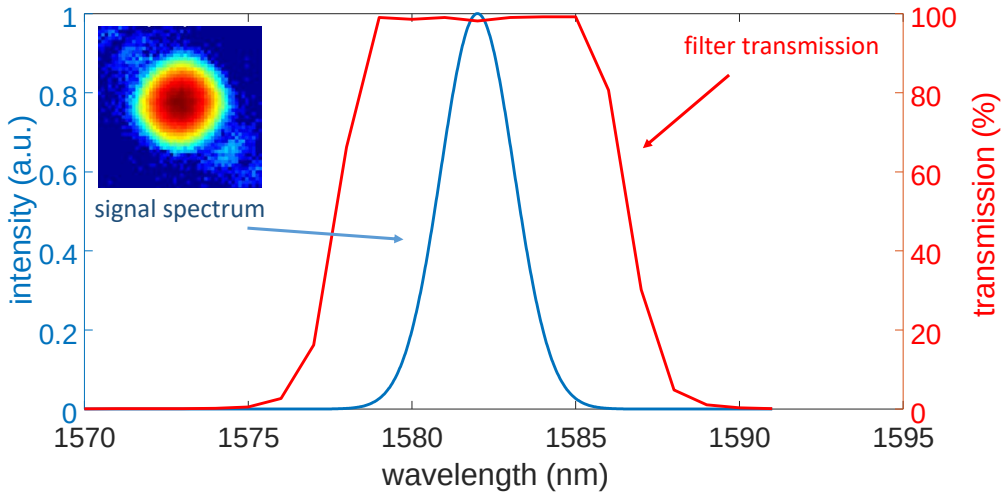

Figure A-1: Transmission profile (red) of the spectral filter shows a central flat-top 6-nm region with near-unity transmission compared with the signal spectrum (blue) with a 2.62 nm bandwidth. The inset shows the JSI with its residual side lobes in logarithmic scale when mild filtering is not used.

Appendix B

Mathematical model of frequency-shifted Hong-Ou-Mandel interference and background subtraction

B.1 Mathematical model of Hong-Ou-Mandel interference

In this section, we model the reported Hong-Ou-Mandel (HOM) experiment discussed in Chapter 3. We will employ a cw-pumped, type-II quasi-phase-matched, SPDC source that, after filtering through a waveshaper and idler-beam polarization rotation, supplies flat-fluorescence-spectra, co-polarized signal and idler beams—with the latter delayed by T—to the interferometer's 50/50 beam splitter. The signal (S) and idler (I) scalar-wave, positive-frequency field operators entering that beam splitter will be taken to be in identical spatial modes whose $\sqrt{\text{photons/s}}$ positive-frequency field operators, $\hat{E}_S(t)$ and $\hat{E}_S(t)$, are in a zero-mean, jointly-Gaussian state that is completely characterized by those operators' non-zero correlation functions and spec-

tra [139], viz.,

$$\langle \hat{E}_S^\dagger(t)\hat{E}_S(t')\rangle = K^{(n)}(t-t')e^{i\omega_S(t-t')} = \int_{-\infty}^{\infty}\frac{d\omega}{2\pi}S^{(n)}(\omega)e^{i\omega(t-t')}e^{i\omega_S(t-t')}, \tag{B.1}$$

$$\langle \hat{E}_I^\dagger(t)\hat{E}_I(t')\rangle = K^{(n)}(t-t')e^{i\omega_I(t-t')} = \int_{-\infty}^{\infty}\frac{d\omega}{2\pi}S^{(n)}(\omega)e^{i\omega(t-t')}e^{i\omega_I(t-t')}, \tag{B.2}$$

$$\langle \hat{E}_S(t)\hat{E}_I(t')\rangle = K_{SI}^{(p)}(t-t')e^{-i\omega_S t-i\omega_I t'} = \int_{-\infty}^{\infty}\frac{d\omega}{2\pi}S^{(n)}(\omega)e^{i\omega(t-t')}e^{-i\omega_S t-i\omega_I t'}, \tag{B.3}$$

where angle brackets denote ensemble average, and ω_S and ω_I are the center frequencies of the signal and idler beams. The normally-ordered correlation function and its associated fluorescence spectrum are given by [139]:

$$K^{(n)}(\tau) = \frac{|\kappa|^2\ell^2\Delta\Omega}{2\pi}\frac{\sin(\Delta\Omega\tau/2)}{\Delta\Omega\tau/2}, \tag{B.4}$$

and

$$S^{(n)}(\omega) = \begin{cases} |\kappa|^2\ell^2 & \text{for } |\omega| \le \Delta\Omega/2, \\ 0 & \text{otherwise,} \end{cases} \tag{B.5}$$

where $|\kappa|$ is the SPDC source's signal-idler coupling coefficient, ℓ is its crystal length, and $\Delta\Omega/2\pi$ is its fluorescence bandwidth (in Hz). The phase-sensitive correlation function and its associated spectrum—suppressing the signal and idler's differential group delay—are given by [139]:

$$K_{SI}^{(p)}(\tau) = \frac{i\kappa\ell\Delta\Omega}{2\pi}\frac{\sin(\Delta\Omega\tau/2)}{\Delta\Omega\tau/2}, \tag{B.6}$$

and

$$S^{(p)}(\omega) = \begin{cases} i\kappa\ell & \text{for } |\omega| \le \Delta\Omega/2, \\ 0 & \text{otherwise,} \end{cases} \tag{B.7}$$

The positive-frequency field operators at the outputs of the HOM interferometer's 50/50 beam splitter are:

$$\hat{E}_S^{\text{out}}(t) = \frac{\hat{E}_S(t) + \hat{E}_I(t-T)}{\sqrt{2}}, \tag{B.8}$$

$$\hat{E}_I^{\text{out}}(t) = \frac{\hat{E}_S(t) - \hat{E}_I(t-T)}{\sqrt{2}}, \tag{B.9}$$

and these signal and idler output operators illuminate single-photon detectors, which are assumed to have insignificant dark counts and quantum efficiencies η_S and η_I. The resulting time-stamped photon-counting records are used to compute the signal-referenced, product-of-counts-protocol coincidence rate [140],

$$C(T) = \frac{\eta_S \eta_I}{T_m} \int_{-T_m/2}^{T_m/2} dt \int_{t-T_g/2}^{t+T_g/2} dt' \langle \hat{E}_S^{\text{out}\dagger}(t) \hat{E}_I^{\text{out}\dagger}(t') \hat{E}_S^{\text{out}}(t) \hat{E}_I^{\text{out}}(t') \rangle, \tag{B.10}$$

where the quantum efficiency factors arise from the quantum theory of photodetection, T_m and T_g are, respectively, the durations of the data-collection interval and the coincidence gate, and $T_m \gg T_g$. Gaussian-state moment factoring reduces the $C(T)$ expression from Eq. (B.10) to:

$$\begin{aligned} C(T) = & \frac{\eta_S \eta_I}{T_m} \int_{-T_m/2}^{T_m/2} dt \int_{t-T_g/2}^{t+T_g/2} dt' \langle \hat{E}_S^{\text{out}\dagger}(t) \hat{E}_S^{\text{out}}(t) \rangle \langle \hat{E}_I^{\text{out}\dagger}(t') \hat{E}_I^{\text{out}}(t') \rangle \\ & + \frac{\eta_S \eta_I}{T_m} \int_{-T_m/2}^{T_m/2} dt \int_{t-T_g/2}^{t+T_g/2} dt' |\, \langle \hat{E}_S^{\text{out}\dagger}(t) \hat{E}_I^{\text{out}}(t') \rangle \,|^2 \\ & + \frac{\eta_S \eta_I}{T_m} \int_{-T_m/2}^{T_m/2} dt \int_{t-T_g/2}^{t+T_g/2} dt' |\, \langle \hat{E}_S^{\text{out}}(t) \hat{E}_I^{\text{out}\dagger}(t') \rangle \,|^2. \end{aligned} \tag{B.11}$$

Using Eqs. (B.1)-(B.9), assuming that $T_g \gg 1/\Delta\Omega + |T|$, and defining $\Delta\omega = |\omega_S - \omega_I|$, we now get:

$$
\begin{aligned}
C(t) &\approx 2\eta_S\eta_I T_g K^{(n)2}(0) \\
&\quad + \frac{\eta_S\eta_I}{4}\int_{\infty}^{\infty} d\tau \Big\{ |K_{SI}^{(p)}(\tau+T)|^2 + |K_{SI}^{(p)}(-\tau+T)|^2 \qquad \text{(B.12)} \\
&\quad - 2\mathrm{Re}[K_{SI}^{(p)*}(-\tau+T)K_{SI}^{(p)}(\tau+T)e^{-i(\omega_S-\omega_I)\tau}] \Big\} \\
&= \begin{cases} 2\eta_S\eta_I T_g \left(\frac{|\kappa|^2\ell^2\Delta\Omega}{2\pi}\right)^2 + \frac{\eta_S\eta_I}{2}\frac{|\kappa|^2\ell^2\Delta\Omega}{2\pi}\left(1-\frac{\sin[\Delta\Omega-\Delta\omega)T]}{\Delta\Omega T}\right), & \text{for } \Delta\omega \le \Delta\Omega, \\ 2\eta_S\eta_I T_g \left(\frac{|\kappa|^2\ell^2\Delta\Omega}{2\pi}\right)^2, & \text{for } \Delta\omega > \Delta\Omega. \end{cases} \qquad \text{(B.13)}
\end{aligned}
$$

The first term in both regions is the rate of accidental coincidences, while the second term is the rate of true coincidences. If we suppress the accidentals in Eq. B.13's coincidence rates we find that the normalized true coincidence rate for our idealized experiment is:

$$
\frac{C(T)}{C(\infty)} = \begin{cases} 1-\frac{\sin[(\Delta\Omega-\Delta\omega)T]}{\Delta\Omega T}, & \text{for } \Delta\omega \le \Delta\Omega, \\ 0, & \text{for } \Delta\omega > \Delta\Omega. \end{cases} \qquad \text{(B.14)}
$$

B.2 Background estimation in HOM measurements

High background accidentals were observed in our HOM measurements because of the disproportional loss between the frequency-shifted path and the frequency-unshifted path. In this section, we calculate singles and coincidences for HOM measurements in various configurations and estimate the proper background subtraction that should be applied to experimental data taken using the setup shown in Fig. 3-3 [141]. The definitions of parameters used in this procedure are given in Table B.1

T_g	coincidence window (was set to 2 ns in the experiment)
P_0	mean number of SPDC pair in signal and idler paths within T_g
P_{1s}	mean number of SPDC signal in signal path without the conjugate idler in idler path within T_g
P_{1i}	mean number of SPDC idler in idler path without the conjugate signal in signal path within T_g
P_{2s}	mean number of pairs in signal path within T_g
P_{2i}	mean number of pairs in idler path within T_g
η_s	system efficiency for signal path
η_i	system efficiency for idler path
N_s	signal singles per second when idler path is blocked
N_i	idler singles per second when signal path is blocked
$C_s(t=0)$	signal coincidences per second within same T_g when idler path is blocked
$C_i(t=0)$	idler coincidences per second within same T_g when signal path is blocked
$C_s(t\neq 0)$	signal coincidences per second within two different T_g when idler path is blocked
$C_i(t\neq 0)$	idler coincidences per second within two different T_g when signal path is blocked
$C_{si}(t=0)$	HOM coincidences per second within the same T_g window
$C_{si}(t\neq 0)$	HOM coincidences per second between two different T_g windows

Table B.1: Parameter definitions in estimating HOM background.

We note that P_{2s} and P_{2i} account for pairs that could be due to inadequate extinction ratio for the fiber PBS or accidental phase matching that generates co-polarized signal and idler pairs. The distinction for P_0 and P_{1s} (or P_{1i}) is that the case with P_0 can lead to signal-idler coincidence but the cases with P_1 cannot. P_{1s} and P_{1i} may represent, for example, fluorescence background singles.

We analyze the background statistics based on the following configuration. The orthogonal signal and idler photons are generated from a type-II phase-matched PPKTP waveguide and the photon pairs are coupled into an optical fiber. The signal and idler are separated using a fiber polarization beam splitter. The signal goes through a waveshaper that reduces the signal's bandwidth. The idler goes through the frequency shifter. The co-polarized signal and idler are then combined at a fiber 50/50 beam splitter that outputs to two SNSPD detectors D1 and D2 with presumably

the same quantum efficiencies. The signal path can be varied through a free-space adjustable gap.

For coincidence measurements, we assume that if one photon triggers D1 and the other D2 within the same T_g window, a coincidence count is registered on the Hydraharp setup (with a small physical delay from 50/50 BS to D2). For two different T_g windows, D1 must be triggered first before D2 is triggered in order to obtain a coincidence. Effectively, when D1 is triggered, it waits for D2 to trigger and that falls into the appropriate time bin histogram. We should note that the longer it waits, the more likely that another photon triggers D1 again, thus resetting the reference time. Hence, we should see that the background coincidence counts fall slowly as the time delay exceeds the dead time. We note that we assume no dead time in order to simplify the calculations.

We make a few simplifying assumptions that match the experimental setup. The various mean numbers per T_g gate are assumed to be much smaller than 1, and they all obey Poisson statistics. We assume that P_0, P_{1s}, P_{1i} are comparable, and P_{2s}, P_{2i} $\ll P_0$, P_{1s}, P_{1i}. Hence, we retain terms up to the square of P_0, P_{1s}, P_{1i} and linearly for P_{2s}, P_{2i}. In particular, terms such as $P_{2x}P_0$, $P_{2x}P_{1y}$ are ignored, where x, y are s or i.

If two photons arrive at the same detector with efficiency η, the probability that it does not get triggered is given by $(1-\eta)^2$ so that the triggering probability is given by $1-(1-\eta)^2 = \eta(2-\eta)$. If the same two photons (from a single path) arrive at the 50/50 BS, then half of the time, they go to the same detector, so that probability is $1/2 * \eta(2-\eta) = \eta(1-\eta/2)$, while the other half of the time, they go to separate detectors so that probability of singles is $1/2*2\eta = \eta$, for a total probability of singles is given by $2\eta(1-\eta/4)$.

Single path, two detectors, and Poisson statistics

In Poisson statistics with mean P, the probability of no photons is given by Pr(0) $= e^{-P} \approx 1 - P + P^2/2$, up to order of P^2. For exactly 1 photon, the probability is Pr(1) $= Pe^{-P} \approx P - P^2$. For exactly two photons, the probability is given by Pr(2)

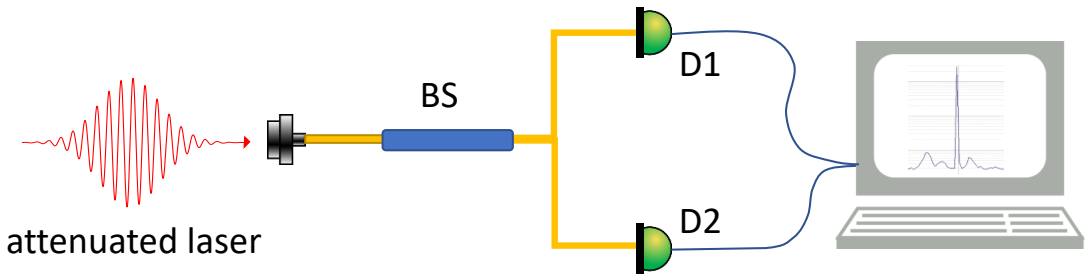

Figure B-1: Test setup for testing the coincidence detection system. BS: 50/50 beam splitter; D1, D2: detector 1 and 2.

$= (1/2)P^2e^{-P} \approx P^2/2$. We will use these probabilities when we calculate singles and coincidences. First, we will verify our detection system with an attenuated laser source that it obeys Poisson statistics. We used the setup shown in Fig. B-1 to perform the statistics test. An attenuated photon stream from a 1550 nm laser was coupled into an optical fiber and arrived at a 50/50 beam splitter that went to two identical detectors D1 and D2. The photon detections were recorded using the Hydraharp. The singles rate N and coincidence rates $C(t=0)$ and $C(t\neq 0)$ can be modeled as:

$$N = [\Pr(1)\eta + \Pr(2)2\eta(1-\frac{\eta}{4})]/T_g = (1-\frac{1}{4}P\eta)P\eta/T_g, \tag{B.15}$$

$$C(t=0) = \Pr(2)\frac{1}{2}\eta^2/T_g = \frac{1}{4}P^2\eta^2/T_g, \tag{B.16}$$

$$C(t\neq 0) = \Pr(1)^2\frac{1}{4}\eta^2/T_g = \frac{1}{4}P^2\eta^2/T_g = C(t=0). \tag{B.17}$$

We note that for $C(t\neq 0)$ with t larger T_g, detector D1 must be triggered first, with probability $\eta/2$ for the first photon, and detector D2 is triggered by the second photon with probability $\eta/2$.

In the following table, we show the measured coincidence and singles count rates and the calculated coincidence rates $\text{coincidence}_{\text{cal}}$ based on Poisson statistics at various laser attenuations.

laser attenuation (dB)	D1(/s)	D2(/s)	coincidence(/s)	coincidence$_{\text{cal}}$(/s)
86	29627	28576	1.2	1.7
84	45580	47120	4.1	4.3
82	69230	74480	11.4	10.3
80	112230	115900	26.5	26.0
78	178880	183540	66.6	65.7
76	279500	285000	167.5	159.3
74	438600	444600	412.3	390.0
72	679400	695400	1021.8	945.0
70	1044900	1079200	2417.6	2255.9
68	1599600	1622600	5572	5191.3

Table B.2: Measured singles and coincidence rates at different laser attenuation.

Signal only, idler-path blocked

In the following sections, we estimate the background counts for the setup shown in Fig. 3-3. For singles, if we assume only the presence of pairs with probability P_{2s} but without P_0 or P_{1s}, we should, in principle, write it as $P_{2s}(1-P_0)(1-P_{1s})$, but because of the way we retain various terms mentioned above, it can be simplified to just P_{2s}. The singles rate N_s and coincidence rates $C_s(t=0)$ and $C_s(t\neq 0)$ can be written as:

$$N_s = \Big[(P_0+P_{1s})[1-\frac{\eta_s}{4}(P_0+P_{1s})] + 2P_{2s}(1-\frac{\eta_s}{4})\Big]\eta_s/T_g, \tag{B.18}$$

$$C_s(t=0) = \Big[\frac{1}{2}P_{2s} + \frac{1}{4}(P_0+P_{1s})^2\Big]\eta_s^2/T_g, \tag{B.19}$$

$$C_s(t\neq 0) = \frac{1}{4}(P_0+P_{1s})^2\eta_s^2/T_g. \tag{B.20}$$

Here, the singles rate N_s is the total singles rate, which is the singles rate sum of signal's and idler's detectors. In N_s, the term $(P_0+P_{1s})[1-\frac{\eta_s}{4}(P_0+P_{1s})]\eta_s/T_g$ is the contribution from the signal photons calculated using Eq. (B.15). The term $2P_{2s}(1-\frac{\eta_s}{4})\eta_s/T_g$ is the total probability of singles from the P_{2s} case in which the lowest nonzero term has two photons in the signal path.

Idler only, signal-path blocked

For singles, if we assume only the presence of pairs with probability P_{2i} but without P_0 or P_{1i}, we should, in principle, write it as $P_{2i}(1-P_0)(1-P_{1i})$, but because of the way we retain various terms mentioned above, it can be simplified to just P_{2i}. The singles rate N_i and coincidence rates $C_i(t=0)$ and $C_i(t\neq 0)$ can be written as:

$$N_i = \Big[(P_0+P_{1i})[1-\frac{\eta_i}{4}(P_0+P_{1i})]+2P_{2i}(1-\frac{\eta_i}{4})\Big]\eta_i/T_g, \tag{B.21}$$

$$C_i(t=0) = \Big[\frac{1}{2}P_{2i}+\frac{1}{4}(P_0+P_{1i})^2\Big]\eta_i^2/T_g, \tag{B.22}$$

$$C_i(t\neq 0) = \frac{1}{4}(P_0+P_{1i})^2\eta_i^2/T_g. \tag{B.23}$$

Two SPDC pairs within T_g

In this subsection, we consider the case of there being two pairs of SPDC photons within the same T_g window, which occurs with probability $P_0^2/2$. Because we assume multimode SPDC output and that the photon pulse width is much smaller than the coincidence window T_g, the two pairs of photons are not in the same mode. That is, we have one pair of one mode and another pair of another mode.

At the HOM dip center, when each pair arrives at the BS at the same time, there is no coincidence. However, because we have two pairs, half of the time one pair goes to one detector and the other pair goes to the other detector and a coincidence is detected. The probability of a coincidence count at the dip center is therefore $(1/2)(\eta_s+\eta_i)^2$. Here we assume (only for this two-pair case) the system efficiencies η_s and η_i are low such that the probability of registering a click by a detector for a pair of signal and idler photons is simply $\eta_s+\eta_i$.

Away from the HOM dip center, we consider that there are 16 possibilities of how the four photons are distributed between the two detectors. Two cases have all photons going to one detector resulting in no coincidence. Eight cases have 3 photons going to one detector, and six cases have 2 photons going to each detector. For the eight cases of 3 photons going to one detector, the total probability of a coincidence is $[4\eta_s(\eta_s+2\eta_i)+4\eta_i(\eta_i+2\eta_s)]/16 = (\eta_s^2+\eta_i^2+4\eta_s\eta_i)/4$. For the six cases of two

photons per detector, we have the total probability of $[2(2\eta_s)(2\eta_i)+4(\eta_s+\eta_i)^2]/16 = (\eta_s^2+\eta_i^2+4\eta_s\eta_i)/4$. Hence the total probability of a coincidence count away from the dip center is $(\eta_s^2+\eta_i^2+4\eta_s\eta_i)/2$. Therefore, we can write the total probability as:

$$\frac{1}{2}P_0^2\Big[\frac{1}{2}(\eta_s+\eta_i)^2+\alpha\eta_s\eta_i\Big] = \frac{1}{2}P_0^2\eta_s\eta_i\Big[1+\alpha+\frac{1}{2}\Big(\frac{\eta_s}{\eta_i}+\frac{\eta_i}{\eta_s}\Big)\Big], \tag{B.24}$$

where $\alpha = 0$ at the dip center and $\alpha = 1$ away from the dip center. α can also be nonzero at the center of the dip if the signal and idler photons are not perfectly matched spectrally. We note that the probability of one pair at time 0 and another pair at time t is P_0^2 for $t \neq 0$.

There is an alternative way to arrive at the same formula that may be easier to understand and calculate. Again, we assume that the system efficiencies are much less than unity such that we can ignore the cases in which more than two photons arrive at the 50/50 BS. For example, if we consider $\eta \sim 10\%$, the chance of having 4 photons at the BS is 10^{-4}, 3 photons would be 4×10^{-3}, and 2 photons would be 6×10^{-2}, so that ignoring the 3-photon and 4-photon cases would make very little difference.

There are 6 different combinations for the two photons at the BS. Two cases involve conjugate signal and idler of the same pair, so they interfere to yield no coincidence at the dip center ($\alpha = 0$) or the coincidence probability is $\eta_s\eta_i/2$ far away from the dip center ($\alpha = 1$). Two cases involve signal-signal and idler-idler, so they have coincidence probabilities of $\eta_s^2/2$ and $\eta_i^2/2$, respectively. The other two cases involve signal and idler from different modes, so they do not interfere and the coincidence probability is $\eta_s\eta_i/2$. The total coincidence probability is then given by:

$$\frac{1}{2}P_0^2\Big[2\times\frac{1}{2}\alpha\eta_s\eta_i+\frac{1}{2}(\eta_s^2+\eta_i^2)+2\times\frac{1}{2}\eta_s\eta_i\Big] = \frac{1}{2}P_0^2\eta_s\eta_i\Big[1+\alpha+\frac{1}{2}\Big(\frac{\eta_s}{\eta_i}+\frac{\eta_i}{\eta_s}\Big)\Big], \tag{B.25}$$

which is exactly the same as Eq. (B.24).

HOM measurements and background subtraction

First we calculate the coincidence rate $C_{si}(t=0)$, then the background coincidence rate $C_{si}(t\neq 0)$, and make allowance for the proper background subtraction to get the background-subtracted coincidence rate. Note that it is not valid to remove the term proportional to P_0^2 because that contribution is due to multipair events when pumping the SPDC too hard.

$$C_{si}(t=0) = C_s(t=0) + C_i(t=0) + \frac{1}{2}\Big[\alpha P_0 + P_0P_{1s} + P_0P_{1i} + P_{1s}P_{1i} + P_0^2\Big[1+\alpha+\frac{1}{2}\Big(\frac{\eta_s}{\eta_i}+\frac{\eta_i}{\eta_s}\Big)\Big]\Big]\eta_s\eta_i/T_g. \tag{B.26}$$

$$C_{si}(t\neq 0) = C_s(t\neq 0) + C_i(t\neq 0) + \frac{1}{2}(P_0+P_{1s})(P_0+P_{1i})\eta_s\eta_i/T_g. \tag{B.27}$$

The background coincidences that we would like to subtract from $C_{si}(t=0)$ are the first two terms of Eq. (B.26), $C_s(t=0)$ and $C_i(t=0)$, and the triple sum of the middle term inside the square bracket, or $(P_0P_{1s}+P_0P_{1i}+P_{1s}P_{1i})\eta_s\eta_i/(2T_g)$. We note that $C_s(t=0)$ and $C_i(t=0)$ contain terms with P_0 in them that we should not subtract. However, because the two terms are dominated by the presence of pairs, P_{2s} and P_{2i}, P_0 contribution is minimal. These two terms are easy to subtract because they are measured in the experiment, so it is straightforward.

The third term is not easy to subtract. The closest one can get is:

$$C'_{si}(t\neq 0) = C_{si}(t\neq 0) - C_s(t\neq 0) - C_i(t\neq 0) = \frac{1}{2}(P_0+P_{1s})(P_0+P_{1i})\eta_s\eta_i/T_g. \tag{B.28}$$

In this case, $C'_{si}(t\neq 0)$ subtracts the extra term $P_0^2\eta_s\eta_i/(2T_g)$ that should be added back to the corrected coincidences. As we see later, one way to deal with this is to somehow approximate the size of the P_0^2 term, as follows. The background subtracted coincidence rate is given by:

$$C'_{si}(t=0) = C_{si}(t=0) - C_s(t=0) - C_i(t=0) - rC'_{si}(t\neq 0), \tag{B.29}$$

where the ratio r ranges from 0 to 1. That is, we try to subtract only a fraction of $C'_{si}(t \neq 0)$. For example, if P_0 is much larger than P_{1s} and P_{1i}, then P_0^2 dominates and we should subtract very little of it by setting $r \approx 0$. On the other hand, if P_0 is small relative to P_{1s} and P_{1i}, then $r \approx 1$. There is not an easy way to deduce these ratios and we have to make guesses.

The signal path includes the waveshaper that sets a signal bandwidth of 50 GHz, whereas the idler path has the full bandwidth of 320 GHz, so we expect the ratio of P_{1i}/P_{1s} to be $\sim 320/50 = 6.4$. Based on Zhong's Optics Express paper on the waveguide source [102], we estimated the heralding efficiency to be 80% (probably the highest obtainable in that setup). That means $P_0/(P_0 + P_{1s}) = 0.8$, or $P_{1s} = 0.25P_0$. With these assumptions, we should use $r = 0.69$. If the heralding efficiency is a little worse, say 70%, then we should use r = 0.81. As it turns out, the term $rC'_{si}(t \neq 0)$ is relatively small and much less than $C_{si}(t = 0)$ and has limited effect in the background calculation.

Appendix C

Performance characterization of superconducting nanowire single-photon detectors

In this appendix, we document the performance of and the characterization procedure for our superconducting nanowire single-photon detectors. We summarize the measured efficiency, dark count rate, and the maximum count rate for each detector channel in Table C.1. These measurements were done on Aug. 26, 2019.

detector number	label	efficiency	dark count/s	timing jitter (ps)	maximum count rate/s
1	C3	0.728	483	230	960,000
2	C4	0.802	369	230	8,500,000
3	D1	0.625	410	271	5,160,000
4	D2	0.745	427	227	8,500,000
7	A1	0.599	790	149	9,600,000
8	A2	0.617	462	156	10,700,000
9	A3	0.572	348	168	11,410,000
10	A4	0.834	527	172	8,400,000
11	B1	0.767	312	160	3,220,000
12	B2	0.775	344	172	4,570,000
13	B3	0.832	536	165	5,100,000
14	B4	0.791	492	172	4,210,000

Table C.1: Performance summary of superconducting nanowire single-photon detectors.

We note that there are 16 detectors in the fridge. NIST manufactured detectors 1-6 in 2013. Photonspot manufactured detectors 7-9 in 2018. NIST manufactured detectors 10-14 in 2018. Detectors 5 and 6 are not functional. A detector label indicates the corresponding amplification electronics for that detector.

The efficiency of the detectors is measured using an attenuated laser source. The laser output power and the applied attenuation are calibrated in reference to an Agilent power meter HP 81634A. The detector count rate is monitored using a Hydraharp time tagger. Detector dark count rate and detector efficiency are measured at different bias currents. The reported value is the optimal current set point. We note that the Hydraharp requires negative input pulses that correspond to negative detector bias currents.

The detector timing jitter is measured with a nonclassical photon pairs source. The photon pairs have a correlation time of less than a few picoseconds and are negligible compared to the detector jitters, which are on the order of hundreds of picoseconds. Similarly, the Hydraharp time tagger has a timing jitter of 12 ps. This contribution is also neglected in our calculation. The signal and idler photons are separated and sent to two different detectors. The recorded coincidence peak indicates the timing jitter of two detectors. We first measured the timing jitter of detectors 1 and 2. Assuming detector 1 and 2 have the same jitters, the timing jitter can be written as: $\delta t_{D1} = \delta t_{D2} = \delta t_{\text{coincidence12}}/\sqrt{2}$. The timing jitters of detectors 3-14 are calculated using this information. For example, we used detectors 1 and 3 to measure the coincidence jitter $\delta t_{\text{coincidence13}}$. Detector 3's timing jitter is then approximated to be $\delta t_3 = \sqrt{t^2_{\text{coincidence13}} - \delta t_1^2}$.

Bibliography

[1] J. Preskill, "Quantum computing in the NISQ era and beyond," *Quantum*, vol. 2, p. 79, 2018.

[2] F. Arute *et al.*, "Quantum supremacy using a programmable superconducting processor," *Nature*, vol. 574, no. 7779, pp. 505–510, 2019.

[3] H.-S. Zhong *et al.*, "Quantum computational advantage using photons," *Science*, vol. 370, no. 6523, pp. 1460–1463, 2020.

[4] N. Gisin and R. Thew, "Quantum communication," *Nature Photonics*, vol. 1, no. 3, pp. 165–171, 2007.

[5] C. L. Degen, F. Reinhard, and P. Cappellaro, "Quantum sensing," *Reviews of Modern Physics*, vol. 89, no. 3, p. 035002, 2017.

[6] P. W. Shor, "Algorithms for quantum computation: discrete logarithms and factoring," in *Proceedings 35th annual symposium on foundations of computer science*, pp. 124–134, IEEE, 1994.

[7] D. Dieks, "Communication by EPR devices," *Physics Letters A*, vol. 92, no. 6, pp. 271–272, 1982.

[8] W. K. Wootters and W. H. Zurek, "A single quantum cannot be cloned," *Nature*, vol. 299, no. 5886, pp. 802–803, 1982.

[9] C. E. Shannon, "Communication theory of secrecy systems," *The Bell System Technical Journal*, vol. 28, no. 4, pp. 656–715, 1949.

[10] C. H. Bennett and G. Brassard, "Quantum cryptography: Public key distribution and coin tossing," *arXiv preprint arXiv:2003.06557*, 2020.

[11] C. H. Bennett, G. Brassard, and N. D. Mermin, "Quantum cryptography without Bell's theorem," *Physical Review Letters*, vol. 68, no. 5, p. 557, 1992.

[12] G. Brassard, N. Lütkenhaus, T. Mor, and B. C. Sanders, "Limitations on practical quantum cryptography," *Physical Review Letters*, vol. 85, no. 6, p. 1330, 2000.

[13] N. Lütkenhaus, "Security against individual attacks for realistic quantum key distribution," *Physical Review A*, vol. 61, no. 5, p. 052304, 2000.

[14] H.-K. Lo, X. Ma, and K. Chen, "Decoy state quantum key distribution," *Physical Review Letters*, vol. 94, no. 23, p. 230504, 2005.

[15] X.-B. Wang, "Beating the photon-number-splitting attack in practical quantum cryptography," *Physical Review Letters*, vol. 94, no. 23, p. 230503, 2005.

[16] D. Stucki, N. Brunner, N. Gisin, V. Scarani, and H. Zbinden, "Fast and simple one-way quantum key distribution," *Applied Physics Letters*, vol. 87, no. 19, p. 194108, 2005.

[17] K. Inoue, E. Waks, and Y. Yamamoto, "Differential phase shift quantum key distribution," *Physical Review Letters*, vol. 89, no. 3, p. 037902, 2002.

[18] F. Grosshans and P. Grangier, "Continuous variable quantum cryptography using coherent states," *Physical Review Letters*, vol. 88, no. 5, p. 057902, 2002.

[19] A. K. Ekert, "Quantum cryptography based on Bell's theorem," *Physical Review Letters*, vol. 67, no. 6, p. 661, 1991.

[20] J. F. Clauser, M. A. Horne, A. Shimony, and R. A. Holt, "Proposed experiment to test local hidden-variable theories," *Physical Review Letters*, vol. 23, no. 15, p. 880, 1969.

[21] J. S. Bell, *Speakable and unspeakable in quantum mechanics: Collected papers on quantum philosophy*. Cambridge University Press, 2004.

[22] F. N. C. Wong, J. H. Shapiro, and T. Kim, "Efficient generation of polarization-entangled photons in a nonlinear crystal," *Laser Physics*, vol. 16, no. 11, pp. 1517–1524, 2006.

[23] E. Y. Zhu, Z. Tang, L. Qian, L. G. Helt, M. Liscidini, J. Sipe, C. Corbari, A. Canagasabey, M. Ibsen, and P. G. Kazansky, "Direct generation of polarization-entangled photon pairs in a poled fiber," *Physical Review Letters*, vol. 108, no. 21, p. 213902, 2012.

[24] T. Zhong, X. Hu, F. N. C. Wong, K. K. Berggren, T. D. Roberts, and P. Battle, "High-quality fiber-optic polarization entanglement distribution at 1.3 μm telecom wavelength," *Optics Letters*, vol. 35, no. 9, pp. 1392–1394, 2010.

[25] C. E. Kuklewicz, M. Fiorentino, G. Messin, F. N. C. Wong, and J. H. Shapiro, "High-flux source of polarization-entangled photons from a periodically poled $KTiOPO_4$ parametric down-converter," *Physical Review A*, vol. 69, no. 1, p. 013807, 2004.

[26] X. Li, P. L. Voss, J. E. Sharping, and P. Kumar, "Optical-fiber source of polarization-entangled photons in the 1550 nm telecom band," *Physical Review Letters*, vol. 94, no. 5, p. 053601, 2005.

[27] M. Mirhosseini, O. S. Magaña-Loaiza, M. N. O'Sullivan, B. Rodenburg, M. Malik, M. P. Lavery, M. J. Padgett, D. J. Gauthier, and R. W. Boyd, "High-dimensional quantum cryptography with twisted light," *New Journal of Physics*, vol. 17, no. 3, p. 033033, 2015.

[28] M. Mafu, A. Dudley, S. Goyal, D. Giovannini, M. McLaren, M. J. Padgett, T. Konrad, F. Petruccione, N. Lütkenhaus, and A. Forbes, "Higher-dimensional orbital-angular-momentum-based quantum key distribution with mutually unbiased bases," *Physical Review A*, vol. 88, no. 3, p. 032305, 2013.

[29] M. Mirhosseini, O. S. Magaña-Loaiza, C. Chen, B. Rodenburg, M. Malik, and R. W. Boyd, "Rapid generation of light beams carrying orbital angular momentum," *Optics Express*, vol. 21, no. 25, pp. 30196–30203, 2013.

[30] I. Ali-Khan, C. J. Broadbent, and J. C. Howell, "Large-alphabet quantum key distribution using energy-time entangled bipartite states," *Physical Review Letters*, vol. 98, no. 6, p. 060503, 2007.

[31] C. Lee *et al.*, "Entanglement-based quantum communication secured by nonlocal dispersion cancellation," *Physical Review A*, vol. 90, no. 6, p. 062331, 2014.

[32] J. Mower, Z. Zhang, P. Desjardins, C. Lee, J. H. Shapiro, and D. Englund, "High-dimensional quantum key distribution using dispersive optics," *Physical Review A*, vol. 87, no. 6, p. 062322, 2013.

[33] T. Zhong *et al.*, "Photon-efficient quantum key distribution using time–energy entanglement with high-dimensional encoding," *New Journal of Physics*, vol. 17, no. 2, p. 022002, 2015.

[34] J. D. Franson, "Bell inequality for position and time," *Physical Review Letters*, vol. 62, no. 19, p. 2205, 1989.

[35] Z. Zhang, J. Mower, D. Englund, F. N. C. Wong, and J. H. Shapiro, "Unconditional security of time-energy entanglement quantum key distribution using dual-basis interferometry," *Physical Review Letters*, vol. 112, no. 12, p. 120506, 2014.

[36] E. Diamanti, H.-K. Lo, B. Qi, and Z. Yuan, "Practical challenges in quantum key distribution," *npj Quantum Information*, vol. 2, no. 1, p. 16025, 2016.

[37] C. Elliott, A. Colvin, D. Pearson, O. Pikalo, J. Schlafer, and H. Yeh, "Current status of the DARPA quantum network," in *Quantum Information and computation III*, vol. 5815, pp. 138–149, International Society for Optics and Photonics, 2005.

[38] M. Mehic *et al.*, "Quantum key distribution: a networking perspective," *ACM Computing Surveys (CSUR)*, vol. 53, no. 5, pp. 1–41, 2020.

[39] M. Sasaki *et al.*, "Field test of quantum key distribution in the Tokyo QKD network," *Optics Express*, vol. 19, no. 11, pp. 10387–10409, 2011.

[40] S. Wang *et al.*, "Field and long-term demonstration of a wide area quantum key distribution network," *Optics Express*, vol. 22, no. 18, pp. 21739–21756, 2014.

[41] S.-K. Liao *et al.*, "Satellite-to-ground quantum key distribution," *Nature*, vol. 549, no. 7670, pp. 43–47, 2017.

[42] J.-P. Chen *et al.*, "Twin-field quantum key distribution over a 511 km optical fibre linking two distant metropolitan areas," *Nature Photonics*, vol. 15, pp. 570–575, 2021.

[43] N. Sangouard, C. Simon, H. De Riedmatten, and N. Gisin, "Quantum repeaters based on atomic ensembles and linear optics," *Reviews of Modern Physics*, vol. 83, no. 1, p. 33, 2011.

[44] D. Zhu *et al.*, "Integrated photonics on thin-film lithium niobate," *Advances in Optics and Photonics*, vol. 13, no. 2, pp. 242–352, 2021.

[45] F. Kaneda, B. G. Christensen, J. J. Wong, H. S. Park, K. T. McCusker, and P. G. Kwiat, "Time-multiplexed heralded single-photon source," *Optica*, vol. 2, no. 12, pp. 1010–1013, 2015.

[46] C. Chen, C. Bo, M. Y. Niu, F. Xu, Z. Zhang, J. H. Shapiro, and F. N. C. Wong, "Efficient generation and characterization of spectrally factorable biphotons," *Optics Express*, vol. 25, no. 7, pp. 7300–7312, 2017.

[47] C. Chen, "Generation and characterization of spectrally factorable biphotons," *S.M.'s Thesis, Massachusetts Institute of Technology*, 2017.

[48] C. Chen, J. E. Heyes, K.-H. Hong, M. Y. Niu, A. E. Lita, T. Gerrits, S. W. Nam, J. H. Shapiro, and F. N. C. Wong, "Indistinguishable single-mode photons from spectrally engineered biphotons," *Optics Express*, vol. 27, no. 8, pp. 11626–11634, 2019.

[49] A. Politi, J. C. Matthews, and J. L. O'Brien, "Shor's quantum factoring algorithm on a photonic chip," *Science*, vol. 325, no. 5945, pp. 1221–1222, 2009.

[50] N. C. Harris, G. R. Steinbrecher, M. Prabhu, Y. Lahini, J. Mower, D. Bunandar, C. Chen, F. N. C. Wong, T. Baehr-Jones, M. Hochberg, S. Lloyd, and D. Englund, "Quantum transport simulations in a programmable nanophotonic processor," *Nature Photonics*, vol. 11, no. 7, pp. 447–452, 2017.

[51] K. Azuma, K. Tamaki, and H.-K. Lo, "All-photonic quantum repeaters," *Nature Communications*, vol. 6, p. 6787, 2015.

[52] C. K. Law, I. A. Walmsley, and J. H. Eberly, "Continuous frequency entanglement: effective finite Hilbert space and entropy control," *Physical Review Letters*, vol. 84, no. 23, p. 5304, 2000.

[53] C. K. Law and J. H. Eberly, "Analysis and interpretation of high transverse entanglement in optical parametric down conversion," *Physical Review Letters*, vol. 92, no. 12, p. 127903, 2004.

[54] P. P. Rohde, W. Mauerer, and C. Silberhorn, "Spectral structure and decompositions of optical states, and their applications," *New Journal of Physics*, vol. 9, no. 4, p. 91, 2007.

[55] W. P. Grice, A. B. U'Ren, and I. A. Walmsley, "Eliminating frequency and space-time correlations in multiphoton states," *Physical Review A*, vol. 64, no. 6, p. 063815, 2001.

[56] P. J. Mosley, J. S. Lundeen, B. J. Smith, P. Wasylczyk, A. B. U'Ren, C. Silberhorn, and I. A. Walmsley, "Heralded generation of ultrafast single photons in pure quantum states," *Physical Review Letters*, vol. 100, no. 13, p. 133601, 2008.

[57] C.-K. Hong, Z.-Y. Ou, and L. Mandel, "Measurement of subpicosecond time intervals between two photons by interference," *Physical Review Letters*, vol. 59, no. 18, p. 2044, 1987.

[58] V. Giovannetti, L. Maccone, J. H. Shapiro, and F. N. C. Wong, "Generating entangled two-photon states with coincident frequencies," *Physical Review Letters*, vol. 88, no. 18, p. 183602, 2002.

[59] O. Kuzucu, F. N. C. Wong, S. Kurimura, and S. Tovstonog, "Joint temporal density measurements for two-photon state characterization," *Physical Review Letters*, vol. 101, no. 15, p. 153602, 2008.

[60] G. Harder, V. Ansari, B. Brecht, T. Dirmeier, C. Marquardt, and C. Silberhorn, "An optimized photon pair source for quantum circuits," *Optics Express*, vol. 21, no. 12, pp. 13975–13985, 2013.

[61] F. Kaneda, K. Garay-Palmett, A. B. U'Ren, and P. G. Kwiat, "Heralded single-photon source utilizing highly nondegenerate, spectrally factorable spontaneous parametric downconversion," *Optics Express*, vol. 24, no. 10, pp. 10733–10747, 2016.

[62] M. M. Weston, H. M. Chrzanowski, S. Wollmann, A. Boston, J. Ho, L. K. Shalm, V. B. Verma, M. S. Allman, S. W. Nam, R. B. Patel, S. Slussarenko, and G. J. Pryde, "Efficient and pure femtosecond-pulse-length source of polarization-entangled photons," *Optics Express*, vol. 24, no. 10, pp. 10869–10879, 2016.

[63] A. M. Brańczyk, A. Fedrizzi, T. M. Stace, T. C. Ralph, and A. G. White, "Engineered optical nonlinearity for quantum light sources," *Optics Express*, vol. 19, no. 1, pp. 55–65, 2011.

[64] J. L. Tambasco, A. Boes, L. G. Helt, M. J. Steel, and A. Mitchell, "Domain engineering algorithm for practical and effective photon sources," *Optics Express*, vol. 24, no. 17, pp. 19616–19626, 2016.

[65] F. Graffitti, D. Kundys, D. T. Reid, A. M. Brańczyk, and A. Fedrizzi, "Pure down-conversion photons through sub-coherence-length domain engineering," *Quantum Science and Technology*, vol. 2, no. 3, p. 035001, 2017.

[66] F. Graffitti, P. Barrow, M. Proietti, D. Kundys, and A. Fedrizzi, "Independent high-purity photons created in domain-engineered crystals," *Optica*, vol. 5, no. 5, pp. 514–517, 2018.

[67] P. B. Dixon, J. H. Shapiro, and F. N. C. Wong, "Spectral engineering by Gaussian phase-matching for quantum photonics," *Optics Express*, vol. 21, no. 5, pp. 5879–5890, 2013.

[68] F. Graffitti, J. Kelly-Massicotte, A. Fedrizzi, and A. M. Brańczyk, "Design considerations for high-purity heralded single-photon sources," *Physical Review A*, vol. 98, no. 5, p. 053811, 2018.

[69] J.-P. W. MacLean, J. M. Donohue, and K. J. Resch, "Direct characterization of ultrafast energy-time entangled photon pairs," *Physical Review Letters*, vol. 120, no. 5, p. 053601, 2018.

[70] A. O. C. Davis, V. Thiel, M. Karpiński, and B. J. Smith, "Measuring the single-photon temporal-spectral wave function," *Physical Review Letters*, vol. 121, no. 8, p. 083602, 2018.

[71] L. Praxmeyer and K. Wodkiewicz, "Time and frequency description of optical pulses," *Laser Physics*, vol. 15, no. 10, pp. 1477–1485, 2005.

[72] V. Ansari, J. M. Donohue, M. Allgaier, L. Sansoni, B. Brecht, J. Roslund, N. Treps, G. Harder, and C. Silberhorn, "Tomography and purification of the temporal-mode structure of quantum light," *Physical Review Letters*, vol. 120, no. 21, p. 213601, 2018.

[73] N. Quesada and A. M. Brańczyk, "Gaussian functions are optimal for waveguided nonlinear-quantum-optical processes," *Physical Review A*, vol. 98, no. 4, p. 043813, 2018.

[74] A. M. Weiner, J. P. Heritage, and E. M. Kirschner, "High-resolution femtosecond pulse shaping," *Journal of the Optical Society of America B*, vol. 5, no. 8, pp. 1563–1572, 1988.

[75] A. M. Weiner, "Femtosecond pulse shaping using spatial light modulators," *Review of Scientific Instrument*, vol. 71, no. 5, pp. 1929–1960, 2000.

[76] T. Gerrits, S. Glancy, T. S. Clement, B. Calkins, A. E. Lita, A. J. Miller, A. L. Migdall, S. W. Nam, R. P. Mirin, and E. Knill, "Generation of optical coherent-state superpositions by number-resolved photon subtraction from the squeezed vacuum," *Physical Review A*, vol. 82, no. 3, p. 031802 (R), 2010.

[77] P. B. Dixon, D. Rosenberg, V. Stelmakh, M. E. Grein, R. S. Bennink, E. A. Dauler, A. J. Kerman, R. J. Molnar, and F. N. C. Wong, "Heralding efficiency and correlated-mode coupling of near-ir fiber-coupled photon pairs," *Physical Review A*, vol. 90, no. 4, p. 043804, 2014.

[78] R. Graham and H. Haken, "The quantum-fluctuations of the optical parametric oscillator. I," *Z. Physik*, vol. 210, no. 3, pp. 276–302, 1968.

[79] E. J. Mason and N. C. Wong, "Observation of two distinct phase states in a self-phase-locked type II phase-matched optical parametric oscillator," *Optics Letters*, vol. 23, no. 22, pp. 1733–1735, 1998.

[80] C. Chen, J. E. Heyes, J. H. Shapiro, and F. N. C. Wong, "Single-photon frequency shifting with a quadrature phase-shift keying modulator," *Scientific Reports*, vol. 11, no. 1, pp. 1–7, 2021.

[81] H. J. Kimble, "The quantum internet," *Nature*, vol. 453, no. 7198, pp. 1023–1030, 2008.

[82] S. Wehner, D. Elkouss, and R. Hanson, "Quantum internet: A vision for the road ahead," *Science*, vol. 362, no. 6412, eaam9288, 2018.

[83] K. Y. Bliokh, F. J. Rodríguez-Fortuño, F. Nori, and A. V. Zayats, "Spin-orbit interactions of light," *Nature Photonics*, vol. 9, no. 12, pp. 796–808, 2015.

[84] J. Huang and P. Kumar, "Observation of quantum frequency conversion," *Physical Review Letters*, vol. 68, no. 14, p. 2153, 1992.

[85] M. A. Albota and F. N. C. Wong, "Efficient single-photon counting at 1.55 μm by means of frequency upconversion," *Optics Letters*, vol. 29, no. 13, pp. 1449–1451, 2004.

[86] S. Zaske *et al.*, "Visible-to-telecom quantum frequency conversion of light from a single quantum emitter," *Physical Review Letters*, vol. 109, no. 14, p. 147404, 2012.

[87] Z. Vernon, M. Liscidini, and J. E. Sipe, "Quantum frequency conversion and strong coupling of photonic modes using four-wave mixing in integrated microresonators," *Physical Review A*, vol. 94, no. 2, p. 023810, 2016.

[88] L. J. Wright, M. Karpiński, C. Söller, and B. J. Smith, "Spectral shearing of quantum light pulses by electro-optic phase modulation," *Physical Review Letters*, vol. 118, no. 2, p. 023601, 2017.

[89] L. Fan, C.-L. Zou, M. Poot, R. Cheng, X. Guo, X. Han, and H. X. Tang, "Integrated optomechanical single-photon frequency shifter," *Nature Photonics*, vol. 10, no. 12, pp. 766–770, 2016.

[90] Private communication with Marko Lončar at Harvard University, 2021.

[91] V. Leong, S. Kosen, B. Srivathsan, G. K. Gulati, A. Cerè, and C. Kurtsiefer, "Hong-Ou-Mandel interference between triggered and heralded single photons from separate atomic systems," *Physical Review A*, vol. 91, no. 6, p. 063829, 2015.

[92] L. Shao, N. Sinclair, J. Leatham, Y. Hu, M. Yu, T. Turpin, D. Crowe, and M. Lončar, "Integrated microwave acousto-optic frequency shifter on thin-film lithium niobate," *Optics Express*, vol. 28, no. 16, pp. 23728–23738, 2020.

[93] M. Izutsu, S. Shikama, and T. Sueta, "Integrated optical SSB modulator/frequency shifter," *IEEE Journal of Quantum Electronics*, vol. 17, no. 11, pp. 2225–2227, 1981.

[94] S. Shimotsu, S. Oikawa, T. Saitou, N. Mitsugi, K. Kubodera, T. Kawanishi, and M. Izutsu, "$LiNBO_3$ optical single-sideband modulator," in *Optical Fiber Communication Conference*, p. PD16, Optical Society of America, 2000.

[95] H. Takesue, T. Horiguchi, and T. Kobayashi, "Numerical simulation of a lightwave synthesized frequency sweeper incorporating an optical SSB modulator composed of four optical phase modulators," *Journal of Lightwave Technology*, vol. 20, no. 11, p. 1908, 2002.

[96] Y. Yamaguchi, A. Kanno, T. Kawanishi, M. Izutsu, and H. Nakajima, "Pure single-sideband modulation using high extinction-ratio parallel Mach-Zehnder modulator with third-order harmonics superposition technique," in *CLEO: Applications and Technology*, pp. JTh2A–40, Optical Society of America, 2015.

[97] H.-P. Lo and H. Takesue, "Precise tuning of single-photon frequency using an optical single sideband modulator," *Optica*, vol. 4, no. 8, pp. 919–923, 2017.

[98] M. C. Sarihan, K.-C. Chang, X. Cheng, Y. S. Lee, T. Zhong, H. Zhou, Z. Zhang, F. N. C. Wong, J. H. Shapiro, and C. W. Wong, "High dimensional quantum key distribution with biphoton frequency combs through energy-time entanglement," in *CLEO: QELS–Fundamental Science*, pp. FTh1A–3, Optical Society of America, 2019.

[99] M. C. Sarihan *et al.*, "Frequency-multiplexed rate-adaptive quantum key distribution with high-dimensional encoding," in *CLEO: QELS–Fundamental Science*, pp. FF3C–3, Optical Society of America, 2020.

[100] E. Saglamyurek, J. Jin, V. B. Verma, M. D. Shaw, F. Marsili, S. W. Nam, D. Oblak, and W. Tittel, "Quantum storage of entangled telecom-wavelength

photons in an erbium-doped optical fibre," *Nature Photonics*, vol. 9, no. 2, pp. 83–87, 2015.

[101] B. Brecht, A. Eckstein, A. Christ, H. Suche, and C. Silberhorn, "From quantum pulse gate to quantum pulse shaper—engineered frequency conversion in nonlinear optical waveguides," *New Journal of Physics*, vol. 13, no. 6, p. 065029, 2011.

[102] T. Zhong, F. N. C. Wong, A. Restelli, and J. C. Bienfang, "Efficient single-spatial-mode periodically-poled $KTiOPO_4$ waveguide source for high-dimensional entanglement-based quantum key distribution," *Optics Express*, vol. 20, no. 24, pp. 26868–26877, 2012.

[103] M. B. Nasr, B. E. A. Saleh, A. V. Sergienko, and M. C. Teich, "Demonstration of dispersion-canceled quantum-optical coherence tomography," *Physical Review Letters*, vol. 91, no. 8, p. 083601, 2003.

[104] J. Nees, S. Williamson, and G. Mourou, "100 GHz traveling-wave electro-optic phase modulator," *Applied Physics Letters*, vol. 54, no. 20, pp. 1962–1964, 1989.

[105] C. Chen, J. H. Shapiro, and F. N. C. Wong, "Experimental demonstration of conjugate-Franson interferometry," *arXiv preprint arXiv:2104.15084*, 2021.

[106] M. A. Nielsen, "Optical quantum computation using cluster states," *Physical Review Letters*, vol. 93, no. 4, p. 040503, 2004.

[107] Z. Zhang, S. Mouradian, F. N. C. Wong, and J. H. Shapiro, "Entanglement-enhanced sensing in a lossy and noisy environment," *Physical Review Letters*, vol. 114, no. 11, p. 110506, 2015.

[108] S. Lloyd, "Enhanced sensitivity of photodetection via quantum illumination," *Science*, vol. 321, no. 5895, pp. 1463–1465, 2008.

[109] Y. Zhang, D. England, A. Nomerotski, P. Svihra, S. Ferrante, P. Hockett, and B. Sussman, "Multidimensional quantum-enhanced target detection via spectrotemporal-correlation measurements," *Physical Review A*, vol. 101, no. 5, p. 053808, 2020.

[110] A. Pe'er, B. Dayan, A. A. Friesem, and Y. Silberberg, "Temporal shaping of entangled photons," *Physical Review Letters*, vol. 94, no. 7, p. 073601, 2005.

[111] S. Mittal, V. V. Orre, A. Restelli, R. Salem, E. A. Goldschmidt, and M. Hafezi, "Temporal and spectral manipulations of correlated photons using a time lens," *Physical Review A*, vol. 96, no. 4, p. 043807, 2017.

[112] M. G. Raymer, A. H. Marcus, J. R. Widom, and D. L. Vitullo, "Entangled photon-pair two-dimensional fluorescence spectroscopy (EPP-2DFS)," *Journal of Physical Chemistry B*, vol. 117, no. 49, pp. 15559–15575, 2013.

[113] C. Reimer *et al.*, "High-dimensional one-way quantum processing implemented on d-level cluster states," *Nature Physics*, vol. 15, no. 2, pp. 148–153, 2019.

[114] N. Tischler, A. Büse, L. G. Helt, M. L. Juan, N. Piro, J. Ghosh, M. J. Steel, and G. Molina-Terriza, "Measurement and shaping of biphoton spectral wave functions," *Physical Review Letters*, vol. 115, no. 19, p. 193602, 2015.

[115] P. Chen, C. Shu, X. Guo, M. M. T. Loy, and S. Du, "Measuring the biphoton temporal wave function with polarization-dependent and time-resolved two-photon interference," *Physical Review Letters*, vol. 114, no. 1, p. 010401, 2015.

[116] A. O. C. Davis, V. Thiel, and B. J. Smith, "Measuring the quantum state of a photon pair entangled in frequency and time," *Optica*, vol. 7, no. 10, pp. 1317–1322, 2020.

[117] F. A. Beduini, J. A. Zielińska, V. G. Lucivero, Y. A. de Icaza Astiz, and M. W. Mitchell, "Interferometric measurement of the biphoton wave function," *Physical Review Letters*, vol. 113, no. 18, p. 183602, 2014.

[118] N. B. Lingaraju, H.-H. Lu, S. Seshadri, P. Imany, D. E. Leaird, J. M. Lukens, and A. M. Weiner, "Quantum frequency combs and Hong-Ou-Mandel interferometry: The role of spectral phase coherence," *Optics Express*, vol. 27, no. 26, pp. 38683–38697, 2019.

[119] K.-C. Chang *et al.*, "648 Hilbert-space dimensionality in a biphoton frequency comb: entanglement of formation and schmidt mode decomposition," *npj Quantum Information*, vol. 7, no. 1, p. 48, 2021.

[120] K. Zielnicki, K. Garay-Palmett, D. Cruz-Delgado, H. Cruz-Ramirez, M. F. O'Boyle, B. Fang, V. O. Lorenz, A. B. U'Ren, and P. G. Kwiat, "Joint spectral characterization of photon-pair sources," *Journal of Modern Optics*, vol. 65, no. 10, pp. 1141–1160, 2018.

[121] J. D. Franson, "Nonlocal cancellation of dispersion," *Physical Review A*, vol. 45, no. 5, p. 3126, 1992.

[122] R. W. Gerchberg, "A practical algorithm for the determination of phase from image and diffraction plane pictures," *Optik*, vol. 35, pp. 237–246, 1972.

[123] F. Vedovato, C. Agnesi, M. Tomasin, M. Avesani, J.-Å. Larsson, G. Vallone, and P. Villoresi, "Postselection-loophole-free Bell violation with genuine time-bin entanglement," *Physical Review Letters*, vol. 121, no. 19, p. 190401, 2018.

[124] N. J. Cerf, M. Bourennane, A. Karlsson, and N. Gisin, "Security of quantum key distribution using d-level systems," *Physical Review Letters*, vol. 88, no. 12, p. 127902, 2002.

[125] A. Mair, A. Vaziri, G. Weihs, and A. Zeilinger, "Entanglement of the orbital angular momentum states of photons," *Nature*, vol. 412, no. 6844, pp. 313–316, 2001.

[126] L. Zhang, C. Silberhorn, and I. A. Walmsley, "Secure quantum key distribution using continuous variables of single photons," *Physical Review Letters*, vol. 100, no. 11, p. 110504, 2008.

[127] O. Ozolins *et al.*, "DWDM transmission based on the thin-film filter technology," *Latvian Journal of Physics and Technical Sciences*, vol. 48, no. 3, p. 55, 2011.

[128] W. Bogaerts, P. De Heyn, T. Van Vaerenbergh, K. De Vos, S. Kumar Selvaraja, T. Claes, P. Dumon, P. Bienstman, D. Van Thourhout, and R. Baets, "Silicon microring resonators," *Laser & Photonics Reviews*, vol. 6, no. 1, pp. 47–73, 2012.

[129] Z. Du, C. Hu, G. Cao, H. Lin, B. Jia, S. Yang, M. Chen, and H. Chen, "Integrated wavelength beam emitter on silicon for two-dimensional optical scanning," *IEEE Photonics Journal*, vol. 11, no. 6, pp. 1–10, 2019.

[130] R. Marchetti, C. Lacava, L. Carroll, K. Gradkowski, and P. Minzioni, "Coupling strategies for silicon photonics integrated chips," *Photonics Research*, vol. 7, no. 2, pp. 201–239, 2019.

[131] R. García-Patrón and N. J. Cerf, "Unconditional optimality of Gaussian attacks against continuous-variable quantum key distribution," *Physical Review Letters*, vol. 97, no. 19, p. 190503, 2006.

[132] Z. Zhang, C. Chen, Q. Zhuang, F. N. C. Wong, and J. H. Shapiro, "Experimental quantum key distribution at 1.3 gigabit-per-second secret-key rate over a 10 dB loss channel," *Quantum Science and Technology*, vol. 3, no. 2, p. 025007, 2018.

[133] H. Zhou, L. Wang, and G. Wornell, "Layered schemes for large-alphabet secret key distribution," in *2013 Information Theory and Applications Workshop (ITA)*, pp. 1–10, IEEE, 2013.

[134] C. Lee, J. Mower, Z. Zhang, J. H. Shapiro, and D. Englund, "Finite-key analysis of high-dimensional time–energy entanglement-based quantum key distribution," *Quantum Information Processing*, vol. 14, no. 3, pp. 1005–1015, 2015.

[135] T. Brougham, S. M. Barnett, K. T. McCusker, P. G. Kwiat, and D. J. Gauthier, "Security of high-dimensional quantum key distribution protocols using Franson interferometers," *Journal of Physics B: Atomic, Molecular and Optical Physics*, vol. 46, no. 10, p. 104010, 2013.

[136] M. Jacques, A. Samani, E. El-Fiky, D. Patel, Z. Xing, and D. V. Plant, "Optimization of thermo-optic phase-shifter design and mitigation of thermal crosstalk on the SOI platform," *Optics Express*, vol. 27, no. 8, pp. 10456–10471, 2019.

[137] A. Liu, L. Liao, D. Rubin, H. Nguyen, B. Ciftcioglu, Y. Chetrit, N. Izhaky, and M. Paniccia, "High-speed optical modulation based on carrier depletion in a silicon waveguide," *Optics Express*, vol. 15, no. 2, pp. 660–668, 2007.

[138] Q.-Y. Zhao, D. Zhu, N. Calandri, A. E. Dane, A. N. McCaughan, F. Bellei, H.-Z. Wang, D. F. Santavicca, and K. K. Berggren, "Single-photon imager based on a superconducting nanowire delay line," *Nature Photonics*, vol. 11, no. 4, pp. 247–251, 2017.

[139] J. H. Shapiro, "Lecture 22 notes for MIT subject 6.453, Quantum optical communications, available online through MIT opencourseware (http://ocw.mit.edu),"

[140] J. H. Shapiro, "Quantum theory of coincidence counting: Gaussian states and quantum interference," in *Frontiers in Optics*, p. FMO3, Optical Society of America, 2004.

[141] F. N. C. Wong, "Note on Hong-Ou-Mandel measurements and background subtraction," 2020.